Hemodynamics and Virtual Stenting of Cerebral Aneurysms

Dissertation
zur Erlangung des akademischen Grades

Doktoringenieur
(Dr.-Ing.)

von **M.Sc. Santhosh Seshadhri**
geb. am 14. September 1980 in Chennai, Indien

genehmigt durch die Fakultät für Verfahrens- und Systemtechnik
der Otto-von-Guericke-Universität Magdeburg

Gutachter:

Prof. Dr.-Ing. Dominique Thévenin
Prof. Dr. Martin Skalej
Prof. Dr.-Ing. Klaus Affeld

Promotionskolloquium am: 14.11.2011

ACKNOWLEDGEMENTS

I want to thank my advisor and Department chair, Prof. Dominique Thévenin, not only for giving me the opportunity to work in the bioengineering field, but also because he has challenged my way of thinking towards the excellence. All of his wise pieces of advice and patience have accelerated this work thoughout my PhD study. Thank you for providing me with financial, technical and moral support. I feel gifted to be blessed with your guidance and I appreciate you taking a chance on a new research area. I am also thankful for his wise criticisms and suggestions in preparing and improving of this dissertation.

I thank Prof. Martin Skalej, my second advisor for all the great discussions that we had in our meetings and his guidance from the medical perspective. Your perseverance has been instrumental in shaping my doctoral work. It has been a pleasure working with you.

I thank Prof. Klaus Affeld for his critical revivew of my work.

Dr. Gábor Janiga - Sincere appreciation for your assistance on various aspects of the project. I have learnt from you, the art of communication and management skills along with your immense experience, when working on collaborative projects. You have been an influential mentor especially concerning all simulations during my work. In addition, your doors were always open to me to discuss various issues and I thank you for accommodating me in your busy schedule.

Mr. Róbert Bordás - Thanks for your immense help in the experimental part of my work, in addition to your insights on various issues, including LABVIEW programming.

I thank the whole Institute for Fluid Dynamics and Thermodynamics for providing this great opportunity and facility to work in Magdeburg. I am

delighted to acknowledge the support I have received from all my colleagues in this department. This work could not have been completed in such a peaceful way without their support. I take this opportunity to express my thanks to all members of MOBESTAN group for their moral and scientific support. Special thanks to Rocco, Mathias and Dr. Beuing for successful participation in VISC09 and VISC10.

Special thanks to Dr. Barbara Witter: she was really supportive in various phases during my stay in Magdeburg! For the financial support of this study, I thank the International Max Planck Research School (IMPRS) committee Magdeburg and Land of Sachsen-Anhalt for the project funding.

I also like to thank all my friends for their encouragements during this research. Specially, many thanks to Thirumalesha, with whom I shared my office room; I learnt many things from him.

My father gave me a special gift, his belief, and the older I become, I have realized the smarter my father seems to get. He taught me, most importantly about optimism, respect and humility. My mother on the other hand, taught me to be patient and work hard to achieve my goals. They have been a source of inspiration throughout my education. This is something every son wishes for, when his parents never doubt his efforts and always believe in him. Dad and Mom, thank you very much. A special thanks to my brother for being a pillar of strength. He has been a source of inspiration and inducing practicality in my life. Thanks to my family who have molded me to become a successful individual, in addition to being an integral part for my quest of knowledge. A special mention about my late grandparents, whose strengths of will power and 'never give up attitude' has helped me all the way through.

ABSTRACT

A cerebral aneurysm is an abnormal irreversible outward bulging of an artery found in the brain. When a cerebral aneurysm ruptures a specific type of bleeding known as Subarachonoid Hemorrhage (SAH) occurs. SAH is a form of stroke and represents 1-7% of all types of strokes. It is a medical emergency and can lead to death or severe disability when unrecognized and not treated at an early stage. Aneurysm surgery remains dangerous because surgeons have limited knowledge of blood flow patterns and due to complex 3D geometry of aneurysms. Therefore, this research project was initiated to make it possible for medical specialists to obtain such detailed information and prepare the intervention, since it would be better to treat the aneurysm before it ruptures. In order to decide whether or not and how to operate, the hemodynamics and associated modifications should be estimated more accurately than previously possible.
Recent developments in minimally invasive approach to cerebrovascular diseases include the placement of stents in arteries for treatment of aneurysms. The placement of a stent across the neck of an aneurysm has the potential to alter the hemodynamics in such a way as to induce self-thrombosis within the aneurysm sac, stopping its further growth and preventing its rupture. Furthermore, the porous nature of a stent will keep the adjacent perforating vessels patent even after the stent is deployed. The alterations in local hemodynamics due to the introduction of a stent are however, not yet well understood.

This work address the above mentioned problem in two parts.

First, a detailed validation study of blood flow simulations is presented. The comparisons between simulations based on Computational Fluid Dynamics (CFD) and in-situ, Laser Doppler Velocimetry (LDV) measurements in the silicon model of a cerebral artery demonstrates the acuracy of the numerical approach. CFD results are obtained by relying on the well-known industrial software FLUENT 6.3. In order to obtain reproducible results, measurements take place in an inverse model, in which the position of the blood vessels is fixed. The used 1:1 model is made from transparent silicone. A complex liquid mixture has been specifically developed for the present investigation: it shows physical properties very similar to real blood, but

leads to a refraction index matched to that of the silicon model. Flow measurements by means of LDV were conducted at several positions within the vessel. This finally allows accurate velocity measurements within the model and a comparisons with CFD under pulsatile conditions.
Even though stents have been identified as a potential treatment of aneurysm, there is still no quantitative data available yet on optimal stent design parameters and on the resulting effect on hemodynamics. Thus, the second part of the work is focused on obtaining a complete characterization and understanding of the flow pattern modifications induced by stenting. For this investigation, idealized side wall aneurysm with straight parent vessel or curved parent vessel are first considered. Finally real patient geometries are investigated. For all the cases non-stented and stented configurations are compared using Computational Fluid Dynamics.

To quantify the stenting efficieny the turn-over time within the neck of the aneurysm is employed. This factor provides detailed information of the quantity of blood flow entering the aneurysm. This information is essential to determine if a specific aneurysm can be suitably treated with a particular stent. We finally show how these results can be used to develop better stent designs.

ZUSAMMENFASSUNG

Ein zerebrales Aneurysma ist eine krankhafte irreversible Ausbeulung einer Arterie im Gehirn. Kommt es zu einer Ruptur eines zerebralen Aneurysmas, schließt sich eine subarachnoidale Hämorrhagie (SAH) an. Eine SAH ist eine Art Hirnschlag und nimmt etwa 1-7% aller Hirnschläge ein. Dabei handelt es sich um einen medizinischen Notfall, der zu einem schnellen Tod oder schweren Behinderungen führen kann, falls das Aneurysma nicht erkannt oder in einem frühen Status behandelt wird. Operative Eingriffe weisen hohe Gefahren auf, da Chirurgen aufgrund der komplexen dreidimensionalen Geometrie der Aneurysmen über eingeschränkte Kenntnis des Blutflussverhaltens verfügen. Deshalb wurde dieses Forschungsprojekt initiiert, um es medizinischen Spezialisten möglich zu machen, detaillierte Information zu erhalten und folglich einen Eingriff zur Verhinderung einer Aneurysmaruptur besser vorzubereiten. Damit im Voraus entschieden werden kann, ob eine Operation notwendig ist, sollten Modifikationen und das damit verbundene hämodynamische Verhalten genauer als bisher abgeschätzt werden. Aktuelle Entwicklungen von minimal-invasiven Eingriffen bei Gehirngefäßerkrankungen beinhalten die Platzierung von Stents in Arterien als Behandlungsmaßnahme für Aneurysmen. Durch die Platzierung eines Stents unterhalb des gesamten Aneurysmahalses kann das Strömungsverhalten dahingehend beeinflusst werden, dass sich eine Eigenthrombose im Aneurysmasack einstellt, die ein weiteres Wachstum verhindert und somit einer Ruptur vorbeugt. Aufgrund der Porosität des Stents werden die angrenzenden Gefäße jedoch auch weiterhin durchströmt. Die lokalen Änderungen der Hämodynamik nach einer Stent-Platzierung sind zum aktuellen Stand der Technik weitestgehend unbekannt. Diese Arbeit richtet sich an die oben genannten Probleme und gliedert sich in zwei Teile. Zunächst wird eine detaillierte Validierungsstudie von Blutflusssimulationen präsentiert. Der Vergleich zwischen Simulationen, die auf der numerischen Strömungsmechanik (CFD) basieren, und lokalen Laser-Doppler-Geschwindigkeitsmessungen (LDV) an einem Silikonmodell einer zerebralen Arterie demonstriert die Genauigkeit der numerischen Annäherung. Die CFD-Ergebnisse werden dabei durch das häufig industriell genutzte Softwarepaket ANSYS FLUENT 6.3 generiert. Um reproduzierbare Ergebnisse zu erhalten, werden Messungen an einem Inversmodell mit einem befestigten

Blutgefäß durchgeführt. Das Modell im Maßstab 1:1 besteht aus durchsichtigem Silikon. Speziell für die vorliegende Untersuchung wurde eine komplexe Flüssigkeitsmixtur hergestellt, welche blutähnliche physikalische Eigenschaften zeigt, allerdings einen Lichtbrechungsindex besitzt, der zum Silikonmodell passt. Strömungsmessungen mittels LDV wurden an unterschiedlichen Positionen des Gefäßes durchgeführt. Dadurch konnten genaue Geschwindigkeits-messungen innerhalb des Modells und ein Vergleich mit den CFD-Simulationen unter pulsatilen Bedingungen realisiert werden. Obwohl Stents bereits als potenzielle Behandlungsmöglichkeit für Aneurysmen angesehen werden, stehen bisher keine quantitativen Daten über optimale Stent-Parameter und deren Beeinflussung der Hämodynamik zur Verfügung. Deshalb fokussiert sich der zweite Teil der Arbeit auf die vollständige Charakterisierung des veränderten Strömungsverhaltens, das durch den Stent-Einsatz verursacht wird. Im Rahmen dieser Untersuchung werden zunächst idealisierte Aneurysmen betrachtet, die sich an der Seite von geraden und -gekrümmten Hauptgefäßen befinden. Abschließend werden patientenspezifische Geometrien untersucht und die Simulationen aller Konfiguration mit und ohne Stent verglichen. Um die Effizienz der Stents quantitativ zu bestimmen, wird die Turnover-Time am Aneurysmahals betrachtet. Dieses Kriterium liefert detaillierte Informationen über den Volumenstrom, der in das Aneurysma eintritt. Diese Information trägt wesentlich zu der Entscheidung bei, ob ein spezifisches Aneurysma mit einem bestimmten Stent behandelt werden sollte. Abschließend zeigen wir, wie die erzeugten Ergebnisse verwendet werden können, um bessere Stent-Designs entwickeln zu können.

NOMENCLATURE

Latin symbols

D	Dome diameter [mm]
E	Youngs moulus of elasticity [MPa]
H	Dome height [mm]
N	Neck width [mm]
n	Refractive Index [-]
p	Pressure [Pa]
P_{ip}	Static pressure at each integration point [Pa]
P_{spec}	Static pressure [Pa]
Re	Reynolds number [-]
S	Semi axis height [mm]
t	time [s]
T	Residence time [s]
$\vec{u}$	Velocity vector of the fluid [m/s]
υ	Local flow velocity magnitude [m/s]
V_{puls}	Flow rate [m/s]
V_x	Particle velocity [m/s]
$\vec{\nabla}$	Gradient symbol

Greek symbols

δ_f	Distance between fringes [mm]
δ_x	Height of the measurement volume [mm]
δ	Characteristic dimension [-]
γ	Shear rate [1/sec]
λ	Laser wavelength [nm]
μ_0	Zero strain viscosity [cP]
μ_∞	Infinite strain viscosity [cP]
μ	Kinematic Viscosity [cP]
ρ	Density of fluid [kg/m^3]
σ	Shear stress [Pa]

Abbreviations

ACA	Anterior Cerebral Artery
ALE	Arbitrary Lagrangian-Eulerian
BFGS	Broyden-Fletcher-Goldfarb-Shanno
BP	Bent parent vessel
CAD	Computer Aided Designs
CE-MRA	Contrast- Enhanced Magnetic Resonance Angiography
CFD	Computational Fluid Dynamics
CTA	Computer Tomography Angiography
CT	Computerized Tomography
DSA	Digital Subtraction Angiography
FSI	Fluid Structure Interaction
HPIV	Holographic PIV
ICA	Internal Carotid Artery
ISA	Intracranial Saccular Aneurysm
KSCN	Potassium Thiocyanate
LDV	Laser Doppler Velocimetry
LIF	Laser Induced Fluorescence
MCA	Middle Cerebral Artery
MRA	Magnetic Resonance Angiography
MRI	Magnetic Resonance Imaging
NaCl	Sodium Chloride
NaSCN	Sodium Thiocyanate
NHP	Neuroform High Porosity
NLP	Neuroform Low Porosity
PAA	Polyacrylamide
PC-MRI	Phase Contrast Magnetic Resonance Imaging
PCoA	Posterior Communicating Arteries
PIV	Particle Image Velocimetry
PTV	Particle Tracking Velocimetry
SAH	Subarachonoid Hemorrhage
SPIV	Stereoscopic PIV
SP	Straight parent Vessel
STL	Stereoithographic
TOF-MRA	Time-of-Flight Magnetic Resonance Angiography
VISC	Virtual Intracranial Stenting Challenge
WOS	Without stent
WSS	Wall Shear Stress [Pa]
ZI	Zinc Iodide

CONTENTS

1. INTRODUCTION

1.1 Blood circulation

In order to understand later results, it is important to know some fundamentals of cardiovascular and cerebrovascular physiology. The blood is irrigated throughout the human body through arteries and it returns through veins. The veins and arteries are interconnected by capillaries. The organ in charge of the pumping process is the heart. This muscle is divided in four cavities: left and right ventricles and atriums. Deoxygenated blood is pumped from the right ventricle to the lungs through the pulmonary artery and oxygenated blood returns to the left atrium. This short circulation is known as pulmonary circulation. An equal volume of oxygenated blood is pumped from the left ventricle to the rest of the body and deoxygenated blood returns to the heart through two main veins (vena cava superior and inferior) to the right atrium. This longer cycle is known as systematic circulation [1]. The process occurs during repetitive cardiac cycles in two phases: the ventricles receive blood while the muscle is relaxed (diastole) and when the blood is expelled from the atriums, and consequently the muscle is contracted (systole). The volume ejected per contraction in a healthy adult is 70-80 mL per min and the heart rate is 60-75 beats/min (5 liters per min) [2]. However, the cardiac output is variable because it adapts to changing internal or external circumstances such as exercise, nerves, etc. Any change of the blood circulation is immediately detected by the brain tissue because this consumes about 20% of the total quantity of oxygen utilized by the whole body [3]. The brain tissue exhibits a high sensibility to any blood disturbance. Therefore, the brain tissue is highly vulnerable to pathogenic factors mostly related to circulatory disorders. For example, if the blood flow is completely stopped, it would cause the death of the brain tissues after 4-5 minutes [4]. Hence, the brain is a highly vulnerable organ for any change in the blood circulation and it has the priority in blood supply over the other organs [3].

The walls of all arteries (except capillaries) are made up of three layers: the tunica intima (the innermost coat or endothelium), tunica media (the middle coat that consists on vascular smooth muscle, collagen, and elastin), and tunica adventitia (the outer coat or connective tissue). The first layer

or intima is a sheet of flattened endothelial cells. The main function of this layer is to avoid the escape of plasma. The media or second layer supplies mechanical strength and contractile power through the elastin and collagen fibres. Elastin is an extracellular protein which enables the artery to expand by up to 10% during each heart beat, while collagen is also an extracellular protein which forms a strong fibrils network in the media. Finally, the last layer, adventitia, maintains the vessel loosely to the surrounding tissue. All three layers are interconnected by an elastic lamina: internal (between the intima and media) and external (between the media and adventitia).

1.2 Intracranial Saccular Aneurysm (ISA)

An Intracranial Saccular Aneurysm (ISA) is an balloning or bulging out of vessel wall that develops at diseased site. Intracranial aneurysms are usually located at the base of the brain in the circle of Willis. The circle of Willis is an arterial ring that connects the two internal carotid systems (see Fig. 1.2.1). The blood flow enters the brain under arterial pressure through the left and right internal carotid arteries and the left and right vertebral arteries. The anterior ciruclation is formed by the Anterior Cerebral Artery (ACA) and the Middle Cerebral Artery (MCA). Aneurysms can occur at any of the cerebral vasculature branch points; however, 90% of them occur at the circle of Willis.

The ACA is the most common site of ruptured aneurysms, followed by the MCA and the posterior circulation [5]. Aneurysms in the internal carotid artery (ICA) are most often encountered at the origin of the Posterior Communicating Arteries (PCoA), followed by the carotid bifurcation, and the origin of the ophthalmic artery. Few aneurysms are located in the cavernous portion of the ICA. However, approximately 10% of giant aneurysms (larger than 25 mm in diameter) are located in the cavernous segment. Multiple aneurysms are found in 20% to 30% of patients with SAH that results from aneurysm rupture [6]. It has been also reported [7] that approximately 30% of all intracranial aneurysms occur on the anterior communicating artery, 20–30% between the interior carotid and posterior communicating arteries, 20% from the middle cerebral artery bifurcation, and 15% from the basilar tip.

It is estimated that 5% of the population has some type of aneurysm in the brain. The incidence of ruptured aneurysm is approximately 10 out of 100,000 people per year. [8]. Furthermore, intracranial aneurysms are responsible for the majority of all non traumatic subarachnoid hemorrhages [9, 10]. From autopsies, the reported occurrence of aneurysms varies from 0.2 to 7.9%. Roughly half of all aneurysms found during autopsy have ruptured

[10].
At the same time, treatments for saccular aneurysms have also a morbidity rate as high as 17.5% after 30 days [11]. There exists, therefore, a need to find ways to determine the risk of rupture of an aneurysm quickly and correctly in order to treat all dangerous lesions while not putting too many patients at risk. Aditionally, the most efficient treatment must be identified.
In current practice, the size of the aneurysm sac is the main criterion in deciding whether treatment should be performed or not. Usual treatment options are (1) surgical clipping, (2) endovascular coil embolization, and more recently (3) stenting with a flow diverter. Clipping consists of placing a clip around the aneurysm neck, preventing blood from flowing into the aneurysm. Depending on the position of the aneurysm, it cannot always be employed or is associated with high perioperative morbidity and mortality. Due to the general trend towards minimal invasive treatments, it tends to be replaced by alternative techniques. Coil embolization consists of filling the aneurysm with a platinum coil in order to decrease blood circulation within the aneurysmal pouch and promote thrombus formation in the aneurysm. Though efficient, considerable risks remain like coil protrusion or escape into the parent vessel during or after intervention, plus a non-negligible risk of aneurysm rupture when filling out the aneurysm sac with coils. In addition, coil-treated aneurysms may remain incompletely occluded with a persisting risk of rupture. Prior to coiling a stent may be placed in the parent artery, especially in case of wide-necked aneurysms, in order to reduce the risks mentioned previously. For instance, the head-to-neck ratio (see later Fig. 1.2.4) has been explored as possible predictor for the rupture of a lesion [12].

Intracranial aneurysms are classified into several categorie [9]. The most commonly occurring type is the saccular aneurysm which comprises 66-90% of all aneurysms (see Fig. 1.2.3). These dilatations are found near an arterial bifurcation in roughly 75% of all cases. Otherwise, they are found as lateral wall aneurysms on straight or curved vessels. Saccular aneurysms are often called berry aneurysms because they resemble berries growing on a branch. Unruptured aneurysms are typically found to have diameters from 2 to 10 mm. These smaller aneurysms often have thick necks and thin transparent walls. Aneurysms that have ruptured are usually larger, ranging from 6 to 50 mm in diameter. These aneurysms are sometimes calcified and partially filled with blood clots [9].

There are other less common varieties of arterial dilatations classified as aneurysms. The fusiform or atherosclerotic aneurysm appears as a region of artery with a local increase in diameter (see Fig. 1.2.3). Mycotic aneurysms are formed by bacteria or fungi that lodge in the artery wall. Dissecting aneurysms occur when the arterial wall is separated forming a pocket that

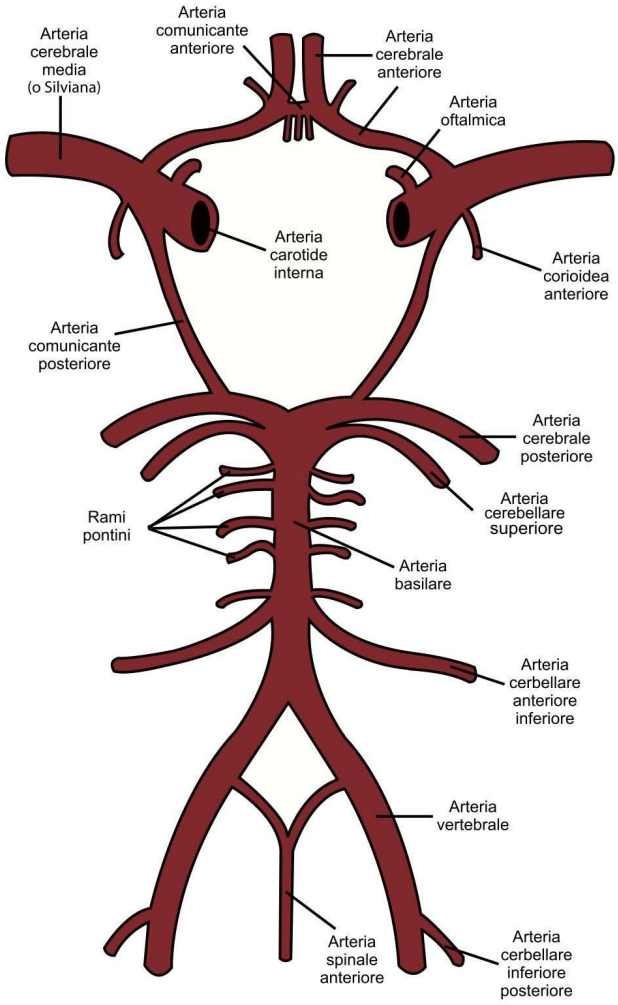

Fig. 1.2.1. Schematic of circle of willis showing arteries [13]

Fig. 1.2.2. Lateral wall aneurysm rupture [13]

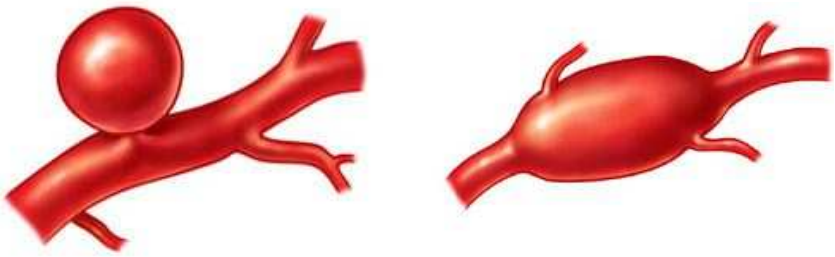

(a) Saccular aneurysm (b) Fusiform aneurysm

Fig. 1.2.3. Types of aneurysm [13]

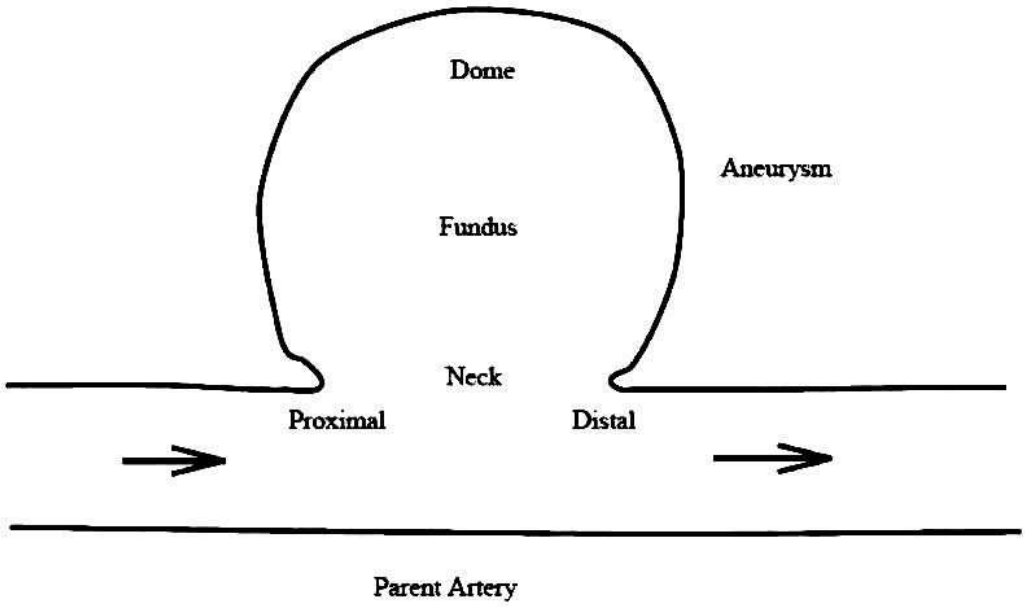

Fig. 1.2.4. Schematic of lateral wall aneurysm with anatomic terms.

inflates with blood.
In saccular aneurysms, the neck (also called the ostium) refers to the connecting region between the aneurysm and parent artery. The neck is further divided into proximal (upstream) and distal (downstream) regions. The center area of the aneurysm is referred to as the fundus, while the dome refers to the top of the aneurysm, i.e., the area farthest from the neck. Figure 1.2.4 illustrates the regions and terms in a lateral wall aneurysm. The inflow region is the area in the neck where flow passes from the parent artery into the aneurysm, and the outflow region is where blood exits the aneurysm and rejoins the arterial flow. Flow patterns in arteries and aneurysms are referred to as either laminar, transitional, or turbulent. In laminar flow, flow path lines are smooth and regular. With turbulent flow, path lines are chaotic, irregular, and tortuous. Turbulent fluids exhibit extreme flow mixing and many small eddies. Transitional flow occurs between laminar and turbulent conditions. Minor instabilities and vortex formation are typical evidence of transitional flow [14, 15]. In our case the flow is laminar (mean Reynolds number of 220 with an artery inlet diameter of 3 mm and an aneurysm dome size of 10 mm), so that only coherent vortex structures are expected.

1.3 Imaging Cerebral Aneurysms

1.3.1 Angiography

Among the many medical imaging techniques which are used to visualize the blood vessel and detect aneurysm, Angiography is a populary known non-invasive technique. Some important aspects of imaging techniques discussed here concern the resolution and contrast which are crucial to perform reliable blood flow modelling. A precise geometrical representation of the vessel walls is the first step towards a faithful simulation of the blood flow therein. Unfortunately, the spatial resolution of the most accurate imaging techniques (0.5 mm) is not much higher than the typical diameter of the main cerebral arteries (1-5 mm). However, it seems that blood flow simulation results pertaining to poor geometrical models do not always differ much from those achieved by accurately defining the vasculature wall [16]. Although it is still impossible to determine which aneurysms will rupture, recent advances in medical imaging techniques such as Computerized Tomography (CT) and Magnetic Resonance Imaging (MRI) have allowed for increased findings of unruptured intracranial aneurysms.

Angiography based on X-rays

The Digital Subtraction Angiography (DSA) is an X-ray procedure in which a high-contrast visualization of blood vessels is made. Modern imaging techniques like MRI and CT hold a significant position in radiology, however DSA is still the gold standard in the diagnosis of aneurysms. In an X-ray based angiography technique two scanners emit X-rays towards the system under investigation along two (ideally orthogonal) projections. Angiography is a catheter based technique in which a thin plastic catheter is introduced into the femoral arterial system percutaneously by the Seldinger technique. Via the catheter the X-ray contrast agent is injected in the vascular region of interest. Under these approaches, so-called empty pictures (without contrast medium) and subsequently filling images (with contrast) are created. Then, the resulting image slices are digitally subtracted from a pre-injection scan to remove the presence of static material. This requires a double dose of radiation and is called Digital Subtraction Angiography (DSA). The contrast and spatio-temporal resolutions are better than those obtained via Magnetic Resonance Angiography (MRA) and Computer Tomography (CT) scans [17] (see below); unfortunately, catheterisation and adverse reaction to the contrast agent make X-ray angiography a significantly invasive technique.

A recent development is three-dimensional rotational angiography (3DRA)[18, 19], for which the volumetric information is obtained through the acquisition

of a series of two-dimensional rotational projections at different angles.

1.3.2 Magnetic Resonance Imaging

Magnetic resonance imaging (MRI) is an established imaging procedure in the routine diagnosis of cerebrovascular diseases. One finds different techniques for vascular imaging in MRI. In clinical routine it works mainly with the time-of-Flight Angiography (TOF-MRA) and contrast-enhanced MRA (CE-MRA). Clinically, the cerebral MRA is now used especially in the diagnosis of stenoses the supra-aortic vessels and in the non-invasive investigation of cerebral vascular malformations application. Usually, the volumetric resolution is 0.4-1 mm. The CE-MRA is a three-dimensional imaging in selective representation of the arterial vascular system. The contrast-enhanced MRA so similar to the DSA. It allows a fast and reliable representation of the aortic arch and extra-and intracranial vessels. Due to its excellent image quality, the large field of investigation and the ultra-short examination times, this method is particularly attractive. The necessary contrast injection, the resulting higher costs and the considerable demands on the hardware are few disadvantages of CE-MRA. In the time-of-flight technique, the investigation of intracranial vessels is carried out without the use of contrast agents. This technique is dependent on the flow and the movement of protons in blood through the imaging plane. To accomplish this as flow enters the area being imagined involves saturating the signal in the slice that is to be imaged with rapid RF pulses. Phase contrast MRI (PC-MRI) technique relies on appropriately varying the magnetic field to create phase shift in protons with a predetermined range of flow velocity. PC-MRA is usually used in image-based computational fluid dynamics (CFD) applications for providing flow-rate waveforms at some planar locations [20] used as boundary conditions, which allows cerebral simulations to be more subject-specific.

1.3.3 Ultrasound

Ultrasound is a cyclic sound pressure with a frequency greater than the upper limit of human hearing, which is approximately 20 kHz. Ultrasonic waves passing through the body are partially reflected on tissue interfaces. Reflections (echoes) are received, processed and displayed. Like PC-MRI, Doppler ultrasound can sometimes be used to provide real-time measurements of the blood flow velocities within the vessel. Due to limitations in three dimensional image correlation techniques it is not a preffered mode of imaging [21] in the context of computational hemodynamic.

1.4 Causes of Cerebral Aneurysms

There are two major theories on the origin of intracranial aneurysms. The congenital theory contends that aneurysms are caused by an inherited weakness in the vascular wall. The degeneration theory holds that aneurysms are caused by acquired factors. Hemodynamics and atherosclerosis effects are often cited as mechanisms of the degeneration theory. Research is ongoing to determine qualitatively the cause of aneurysms and to discover the mechanism of their growth. It is now belived that hemodynamic factors are linked to the etiology of aneurysms, rather than inherited factors [10]. The present study concentrates on the treatment of existing aneurysms and not on the origin of those ICA.

1.5 Currently employed treatments

It is generally difficult to diagnose an aneurysm before rupture occurs. Sometimes, symptoms such as headaches, dizziness, blindness, and neurologic disorders will manifest themselves and prompt testing [9]. Angiography is the primary means of locating and identifying intracranial aneurysms, and can provide the following information [9]: 1. Identification and location, 2. Size and number, 3. Neck configuration, 4. Evidence of spasm, 5. Relation to other arteries.

Presently, intracranial aneurysms can be treated with endovascular or surgical techniques. There are four main methods of treatment, namely: clipping, endovascular embolization including coiling and onyx, stent-assistant coiling and flow diversion.

The first surgical procedure to treat aneurysm was perfromed by Walter Dandy. He used the clip designed by Harvey Cushing [22]. Modern microsurgical and anesthetic techniques and improved anesthetic agent have enabled the direct clipping of some giant intracranial aneurysms (Fig. 1.5.1). The clipping procedure involves craniotomy where in metal clip is placed across the base of the aneurysm surgically gaining direct access in to the cranial cavity (Fig. 1.5.1). This keeps blood from entering the aneurysm. As a result, future bleeding is prevented and nearby brain tissue is protected from further damage. The bone plate is then wired securely into place and the wound is closed.

Surgical treatment remained the predominant treatment for nearly four decades until the development of the detachable coil by Gglielmi in the late 1980s. Endovascular coiling of cerebral aneurysm includes the delivery of small metallic coils into the aneurysm sac (Fig. 1.5.2) through a micro-

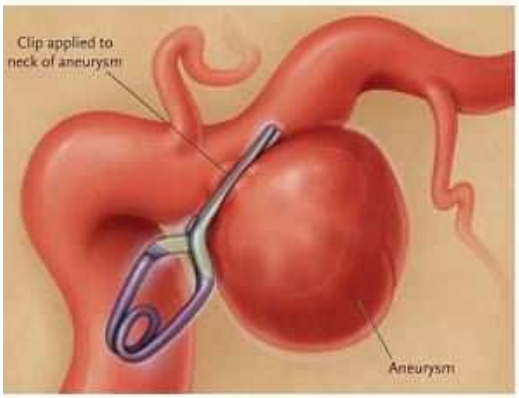

Fig. 1.5.1. Aneurysm clipping. Image taken from [23].

catheter. Coils are detached by electrolyzing a fusible metal. Since all the intervention is performed through the introduction of a catheter in the femoral artery, avoiding open head surgery, this approach is minimally invasive.

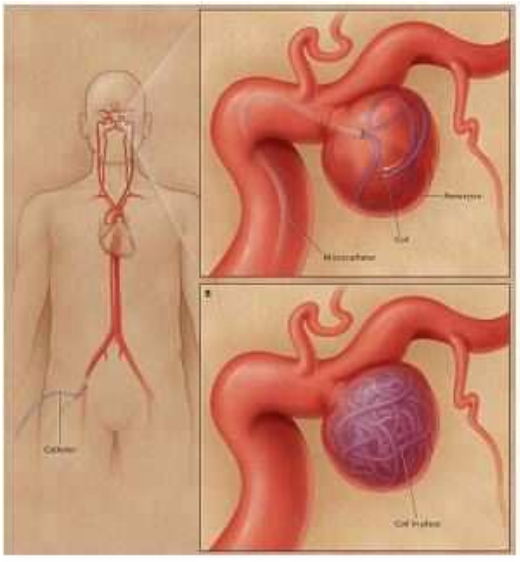

Fig. 1.5.2. Aneurysm Coiling. Image taken from [23].

Ideally, the alteration of flow should promote the formation of a stable thrombus initially, maturing to an organized one within a few weeks, with the eventual exclusion of the aneurysm from the circulation. Endovascular treatment of aneurysm has been proven successful in numerous trials. However, complications such as aneurysm perforation, recanalization, parent artery occlusion, and cerebral embolization still persist. Thrombus generated at the ir-

regular surface of the aneurysm entrance may lead to parent artery occlusion or embolic showers. Aneurysm perforation may occur during catheterization or during the placement of coils into the aneurysm. Preexisting thrombus within the aneurysm sac may be sheared off into the parent trunk. In addition, coil movement and compaction which occurs several months after their placement may foster aneurysm revascularization or regrowth [24]. Intrinsic technical limitations (e.g., coil flexibility, shape, and dimensions) prevent the tight packing of aneurysms, especially those with wide necks, without compromising the parent artery. Clearly, novel approaches are required for a safer, more definitive endovascular treatment of aneurysms.

Another treatment option is the use of liquid embolic material, which is still at the beginning for the treatment of intracranial aneurysms for example Ethibloc and Onyx. Ethibloc is a grain-alcohol related protein that harden on contact with blood. A liquid embolic material (Fig. 1.5.3), Onyx is a biocompatible ethylene-vinyl alcohol polymer, which is precipitated into soft polymeric embolus. This is a special form of the remodeling technique where in the aneurysm is filled with this polymer and the neck of the aneurysm is occluded with the help of balloon (Fig. 1.5.4), which prevents the polymer from migrating into the main circulation.

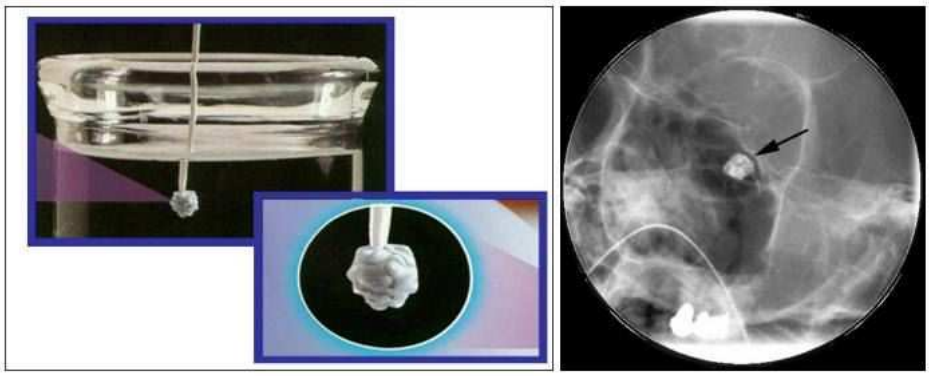

Fig. 1.5.3. Product Onyx. Image taken from [25]

Moret et al. [26] developed remodeling technique as a first approach where they combined the use of a balloon (see Figure 1.5.4) and coils. The balloon temporarily sealed the aneurysm neck until the aneurysm lumen is completely filled with coils. In this way of optimal coil position can be achieved. The simultaneous use of two micro-catheters is significantly more demanding than a coiling with a single catheter. Also, a bad use of the balloon can cause vessel rupture, vasospasm and dissections [27]. The temporary closure of the carrier vessel also increases the thromboembolic risk.

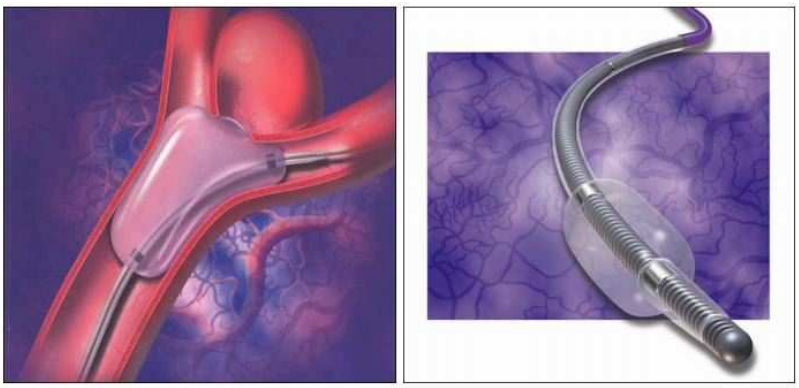

Fig. 1.5.4. Aneurysm Balloon technique. Image take from [28]

Another possibility is the closure of the support vessel. This technique has been known for some time and comes with detachable balloons (see Fig. 1.5.4) or coils, which isolate the aneurysm from the blood stream or at least take the pressure off the aneurysm. Essential in this method is to check the hemodynamic reserves and sufficient collateralization.

The most promising new development for the treatment of wide neck aneurysms, however, is the development of neuro stents aimed at bridging the base. Instead of coiling alone, clinicians can combine with coils to provide a solution for the treatment of unruptured wide-necked cerebral aneurysms [29]. Originating from the cardiology following neuro stents can be found for instance on the market for the treatment of intracranial cerebrovascular aneurysms:

- Neuroform (Boston Scientific SMART, California, USA, Fig 1.5.5(a))
- Wingspan (Boston Scientific SMART, California, USA, Fig 1.5.5(b))
- SILK (BALT Extrusion, Montmorency, France, Fig 1.5.5(c))
- Enterprise (Cordis, LLC, USA, Fig 1.5.5(d))

The development of these implants is still far from complete. So until the present time there are still significant difficulties or restrictions on the use of stents. Those that are balloon-expandable need a relatively high pressure to be spread which is at great risk of overloading the vessel wall. With self-expandable stents, however there is a risk that those do not fully expand. In both systems, a previously incorrectly estimated vessel diameter or vessel dilation can lead to large errors concerning selected stent size. In addition,

the high rigidity of these stents leads to a restricted use in certain targeted areas, since it leads to an inflexible guidance and certain vascular segments are simply not passable. The absence or limited repositioning is another shortcoming of the available neuro stents. The risk of thromboembolism or a serious bleeding risk is, at the present time, in any case much higher than for the sole use of coils. Therefore, both before and after the deployment of the stent, an appropriate anticoagulant therapy is required.

The decision on intervention entirely depends on the rupture risk and on the treatment method. As the mechanical properties of the arterial wall and its corresponding loading state can not be determined in vivo, accurate estimation of the risk of rupture is not possible yet. Presently the rupture rate is associated with size, though there is controversy over critical size. Reliable simulation tools are needed to support medical decisions and intervention planning.

1.6 Scope of investigation

The main goal of this project is to validate numerical simulations of blood flows in aneurysms by comparing in vitro measurements and numerical results. Then, the developed procedure will be used to study the influence

(a) Image taken from [30]

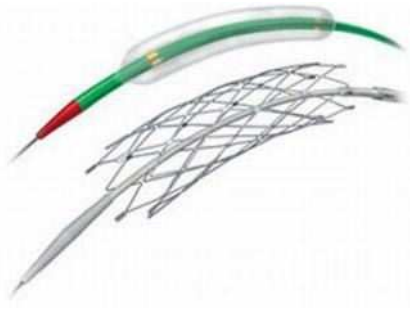

(b) Image taken from [30]

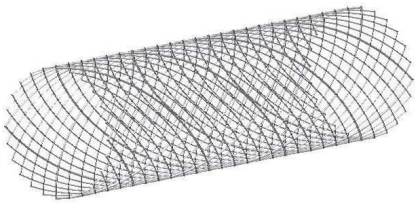

(c)

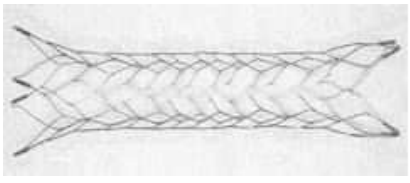

(d) Image taken from [31]

Fig. 1.5.5. Neuro stents for the treatement of cerebrovascular aneurysm

of stent placement in a vessel with an aneurysm. Hemodynamic parameters such as aneurysmal inflow, velocity field, wall shear stress in a virtual aneurysm model as well as in real patient geometries will be considered under steady as well as pulsatile conditions.

We will limit the scope of investigation by making assumptions such as considering blood as a Newtonian fluid, the aneurysm and vessels to be rigid. We will also limit the scope of validation study by selecting Laser Doppler Velocimetry as the sole experimental source of velocity information.

1.7 Thesis organization

The thesis is divided into seven chapters including this introduction and a conclusion. Specifically, Chapter 2 reviews the recent work carried out concerning aneurysm blood flow studies, in vitro validation, imaging based validation along with stenting techniques. Chapter 3 descibes the principles of Laser Doppler Velocimetry and explain in detail the experimental setup and phantom models. It also presents the measurement results and the corresponding validation. Chapter 4 and 5 describe the virtual stenting simulations carried on both virtual aneurysm model as well as in real patients geometries. Chapter 6 reviews the main remaining issues.

2. LITERATURE REVIEW

Extensive research has been done in the past to investigate blood flows in intracranial aneurysms. Experimental studies have been made based on glass models, cardiometric measurements, and computer simulations of lateral wall aneurysms. The availability of advanced computational tools, their cost effectiveness, time savings and the difficulty in conducting in vivo experiments have now popularized CFD techniques.

There are two main ways of studying hemodynamics in aneurysms. The first would be using idealized aneurysm geometries that give enough independence to compromise on the complex shape of actual aneurysms but for which good numerical meshes are possible. Such types of studies are usually parametric in nature. In the second approach, the arterial geometry is obtained in a digital format consisting of voxels. Such real geometries, however, usually result in skewed meshes of poor quality.

2.1 Aneurysm initiation and growth

Over the years its widely accepted that hemodynamic factors are responsible for aneurysm intiation and growth [17, 32, 33, 34, 35, 36, 37]. Hemodynamic stress has in particular a profound effect on the development of cerebral aneurysms [38, 39, 40].

Due to the complexity of the arterial geometry, ideal geometries were initially employed to represent real geometries. However, with the development of new sophisticated techniques such as computed tomography angiography (CTA) and magnetic resonance angiography (MRA), it is now possible to visualize the exact aneurysm geometry. These types of visualization are possible through the injection of a contrast agent in the arterial supply.

The shape of the aneurysm and of the parental vessel is reconstructed from 2D images and is the most important step towards complete analysis because of its strong influence on hemodynamics [17, 32, 38]. These CTA or MRA procedures include not only the imaging data, but also the monitoring of the patients vital signs. Accurate physiologic flow conditions for each individual patient are important to have a better representation [41]. The blood flow waveforms associated with each patient may affect the hemodynamic

stresses and pressures. However, it was demonstrated that by changing the magnitude of the blood waveform, there is usually no major changes in the flow pattern. The maximum and minima in WSS was found to occur at the same locations when the waveform varied [33].

Feng et al. [34] conducted a numerical simulation of the growth of a pseudo-sidewall-aneurysm, in which they concluded that the genesis of the aneurysms is mainly due to high WSS concentrated near the distal neck region. As the aneurysm starts enlarging, the neck region becomes part of the aneurysm sac. The aneurysm keeps growing until it is treated or rupture occurs. Results show that during the development of the aneurysms, high WSS is observed at the distal and proximal end of the aneurysms. This is due to the interaction between the WSS and the degeneration of the wall. During the enlargement phase, fluctuations of WSS are present mostly in the proximal neck region. The enlargement of impingement zones can occur if the arterial curvature is amplified (Hoi et al. [42]). During the cardiac cycle, the bifurcation of the arteries is the primary location of high hemodynamic stress because the blood impinges on the wall. Due to the dilatation process of the distal neck caused by high pressure and shear rates, a saccular aneurysms may develop there. Further growth may occur in the neck and not the dome of the aneurysms.
Other investigations related to saccular aneurysms have concluded that high-speed flow entering the aneurysm leads to persistent and transient vortices. These vortices occur at the proximal and distal ends of the neck, producing dynamic patterns of elevated and oscillatory wall shear stresses [17]. However, many aneurysms do not originate at an arterial branching point. The occurrence of such non branching aneurysms may be related to the hemodynamic pressure. In case of curvature-induced aneurysms, the blood strikes the wall at an oblique angle near the abrupt arterial curvature, and then proceeds along the walls resulting in a high local shear stress upon the endothelium [43].

Not only is the growth of the aneurysm observed near the zones of maximum wall shear stress, the growth could also be related to the prolonged residence times of suspended blood cells that may affect the structure of the aneurysm wall [35]. In addition, investigations have shown that temporary reversal of WSS could trigger pathologic changes in the endothelial cells, leading to aneurysm formation [33]. In some other studies [17, 34, 35, 38], the WSS was found high around the neck of the aneurysm. Finally, some researchers have modeled the growth of aneurysms in simple geometries (model aneurysms) [34, 36]. Aneurysm formation can be influenced by strong secondary flows. These secondary flows may for instance occur due to the

obstruction in some regions of the arteries (cholesterol accumulated on the walls).

2.2 Hemodynamics

Hemodynamics is a study of the forces involved in the blood circulation. Hemodynamic parameters are believed to be largely responsible for aneurysm initiation, growth and rupture [40]. The most important hemodynamic parameters include the pulsatile nature of blood flow, blood pressure and wall shear stress. These fluid mechanical forces also intricately regulate structure and function of the endothelial cell layer, the innermost layer of a vessel wall [44].

Aneurysm and parent vessel geometry, neck size, blood viscosity, wall elasticity etc. also affect the hemodynamics of cerebral aneurysms. However, in large vessels, wall deformation, non-Newtonian fluid behaviour, slurry particles in the fluid, body forces and temperature are often neglected because of their secondary importance [45].

2.2.1 In-vitro investigations

Much of our hemodynamics knowledge comes from a range of experiments that recreate in a more or less realistic manner the steady or unsteady, 3D blood flow in laboratory models. Most of the standard fluid mechanics measurement techniques have been applied to these models. In this section we will focus on some in vitro measurement techniques that do not influence the flow. These non-intrusive methods rely on optical, often laser based signals. In the published literature the authors have mostly used Laser Doppler Velocimetry (LDV) and Particle Image Velocimetry (PIV).

Phantom models built in glass, plexiglass or silicone have been used extensively for experimental studies, in particular to develop and improve imaging techniques. The most commonly used phantoms for intracranial aneurysms are made of silicon. Many authors have carried out such experimental studies, often combined with simulations using simplified models that consider the walls of the arteries as a straight or a curved vessel with a simplified aneurysm [12, 41, 46, 47, 48, 49, 50]. Certain authors [51, 52, 53, 54, 55] carried out research work in a scaled up anatomical phantom models or in simple models and compared their results with CFD simulations. They found important results like the presence of maximum wall shear stress at the downstream of the neck, while the flow shows an unsteady and complex vortex structure inside the aneurysm. Baráth et al. [56] made an in vitro flow evaluation with laser sheet translumination on an anatomic elastic model. Liepsch et al. [57]

used glass and silastic models with Newtonian and non Newtonian perfusion fluids to simulate blood flow in aneurysms. It was found that inflow occurred at the distal lip and was directed towards center of the fundus. Outflow was found to occur at the walls of the fundus. They suggested that flow and stress are directly related to pulsatility and viscosity. Based on in vitro experiments of aneurysms on curved vessels, Niimi, Kawano, and Sugiyama [58] found that curved arteries set up significant secondary flows (rotational flows in a plane normal to the general flow direction). Liou et al. [59] and Danturthi et al. [60] both did experimental studies and show that shape of the aneurysm and neck play an important role in directing the fluid into the aneurysmal area. This was also recently confirmed by Bando et al. [61] who visualized the flow structure in the cerebral aneurysm using Steroscopic particle image velocimetry (stereoscopic PIV) and 2DPIV. The authors concluded that vortex structures along the aneurysm is seen in both steady and pulsatile flow but the direction is different. Recently, Hollnagel et al. [62] used rigid silicone models to understand the flow patterns using LDV. This study was also validated using Phase Contrast Magnetic Resonance Angiography (PC-MRA). Similarly, Tateshimaa et al. [63] validated their studies before and after aneursmal growth using CT angiography along with PIV and LDV.

Wall Shear Stress

Much attention has been given to the fluid dynamic wall shear stresses (WSS) which quantify the interaction between blood and endothelial layer. WSS is a vector whose magnitude is proportional to the blood viscosity and flow velocity gradient normal to the surface, and which acts in a direction parallel to the local velocity at the wall. It is difficult to directly measure WSS either by invivo or invitro techniques, so it is computed from the local velocity distribution near the wall. Therefore, investigation of WSS effects requires excellent knowledge of the local velocity field. Further hemodynamic studies on models of saccular aneurysms are very important in order to obtain quantitative values of hemodynamic stress. Works by Shojima et al. [38], Jou et al. [35] and Boussel et al. [64] provided evidence of the correlation between aneurysm growth and low WSS.

Dome to Neck ratio - an index to predict rupture rate ?

The geometry of a saccular aneurysm is usually described using several characteristic dimensions (Fig. 2.2.1): the neck width N, the dome diameter D, the dome semi-axis height S and the dome height H. In general, the shape

of an aneurysm is given by non-dimensional ratios like D/N, H/N, or D/H. In a study by Parlea et al. [12] the ratio between dome diameter and dome height, D/H, was found to have a mean value around 1 for aneurysms in the circle of Willis, indicating that the average intracranial aneurysm has roughly a spherical shape [12].

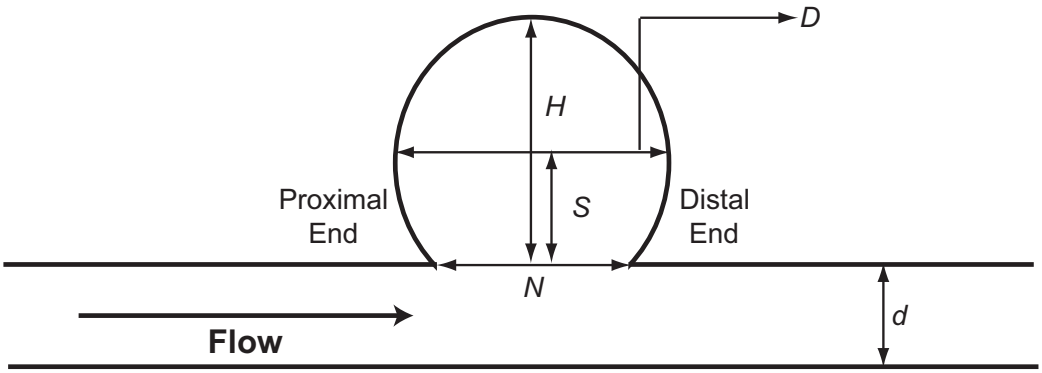

Fig. 2.2.1. Characteristic dimensions employed to describe a saccular aneurysm, as introduced in [12].

The dome-to-neck ratio D/N of an aneurysm is defined as the ratio of aneurysm dome diameter D to major diameter of neck N. For a given aneurysm size, this ratio is essential since the neck size is the factor limiting blood flow into and out of the aneurysm. A study by Ujiie et al. [65] showed that a dome-to-neck ratio higher than 1.75 is associated with at least 80% risk of rupture. The ruptured aneurysms, even those that were less than 10 mm in size, showed a dome to neck ratio exceeding 1.75 [65]. This study suggests that the dome-to-neck ratio may become a reliable index for predicting future rupture and help to analyze the operative indications for performing surgery on incidentally found aneurysms. These authors therefore concluded that the dome-to-neck ratio is a better geometric index than the maximum size alone to quantify intraaneurysmal flow and, thus, the tendency to rupture. Contradicting results were obtained by Wiebers et al. [66] who reported that out of 44 aneurysms they studied, no aneurysm less than 10 mm ruptured, while 8 out of 24 aneurysms of size greater than 10 mm ruptured.

Parent artery curvature

Aneurysms often occur at arterial bifurcations segments of arteries. Hence, investigating aneurysms on curved arteries has gained interest. Several authors have studied the effects of arterial curvatures using computaional stud-

ies [36, 42] and experimentally using Particle Tracking Velocimetry (PTV)[59]. Castro et al. [67] found that curvatures in the parent artery upstream of the aneurysm neck significantly influences the direction of the inflow jet. Extensive parametric studies on the inflow through saccular aneurysms at arterial bends were carried out by Imai et al. [68]. In their blood flow simulation through 22 models of varying arterial curvatures and bends, they have clearly demonstrated the impact of parent artery geometry on the inflow pattern and flux through aneurysms.

2.2.2 Computational studies

In the early days many researchers have modeled virtual aneurysms using simple geometries, considering a simple pipe with a sphere depicting an aneurysm and carrying out CFD studies in order to understand the flow patterns and important hemodynamic parameters.

Numerous pulsatile flow studies [37, 58, 69, 70] have been carried out in lateral side wall aneurysm and curved wall aneurysm models in order to understand the flow patterns entering the aneurysm and its dependence to aneurysm geomteries. In general, most of the authors observed that aneurysm inflow occurred at the downstream lip and outflow along the walls. A complex velocity field was observed within the aneurysm, with aneurysm speeds an order of magnitude below arterial speeds. Aneurysm wall shear stress was found to be low, except at the upstream and downstream wall regions, where strong shear stress concentrations were found. In the distensible model, aneurysm flows were higher than in the rigid model, but still low compared to arterial speeds.

Nonetheless, aneurysm aspect ratio and spatially averaged WSS may be positively correlated with risk of rupture [38]. Venugopal et al. [71] remarked that it is important to impose patient-specific inlet flow rates to accurately simulate the overall hemodynamics.

Zhao et al. [72] results illustrate that the flow field behavior is globally similar when employing fluid-structure interaction models and the one achieved under the rigid wall assumption. Though, when the dynamics of the wall is considered a general reduction in the magnitude of the WSS is observed. But fluid-structure interaction modelling is limited to assuming several patient-specific parameters as they are not usually provided in a standard clinical setting [73].

Recently, Chatziprodromou et al. [74] proposed a metric to assess the risk of cerebral aneurysmal growth formation. Specifically, their risk metric is a function of the WSS, associated with the assumptions that (a) a substantial chaotic blood flow provokes aneurysm formation and expansion[75], and (b)

a low and oscillatory WSS causes vessel wall thickening [76]. Simulations with a cerebral fusiform aneurysm highlighted the region which may exhibit further growth as at the dome of the aneurysm, which likely correlated with the location of aneurysm rupture.

Unfortunately, the risk factor is a function of parameters that are not yet experimentally measured; they should be used to properly formulate the dependence of the risk factor on its variables, like local WSS and vorticity. Second, an important factor which determines aneurysm formation may be a reduced vascular tone, which is not directly caused by high WSS but is a function of multiple factors not well known yet.

2.2.3 Image based CFD validation

With the advent of high resolution 3D medical imaging, powerful computers, and sophisticated image processing techniques, it is now possible to reliably simulate pulsatile blood flow in anatomically realistic arterial geometries derived from in vivo imaging.

The technique starts with the acquisition of the patient-specific geometry. CFD simulations are then capable of providing virtually any information that may be beneficial to medical practitioners, including information on the flow velocities, pressures, wall shear stresses, particle deposits and retention times and even the structural response to the blood flow.

Wang et al. [77] examined the flow by angiography in two identical groups of sidewall aneurysm models with varying parent-vessel curvature in order to understand the flow stagnancy. Jou et al. [35] examined the relationship between hemodynamics and aneurysmal growth. Cebral et al. [78] predicted the location of the major intra-aneurysmal flow structures using computational fluid dynamics. Recently, Hope at al. [79] evaluated intracranial arterial stenoses and aneurysms with accelerated time-resolved three-dimensional (3D) phase-contrast MRI and the validation using CFD.

Cebral et al. [41, 48] carried out cfd based studies on images obtained from CT angiography and 3-D Rotational angiography data. The author raised few important limitations such as patient specific physiological flow conditions and data obtained from multiple feed vessels may be incomplete on 3D rotational angiography. Neglecting those limitations the author concluded that methodology could well be used to draw a correlations between flow patterns and the rputure risk. Cebral et al. [80] discussed sensitivity of patient specific geometries on various hemodynamic parameters, where greater difference was found on the geometry flow field. Hoi et al. [81] underlined the importance of obtaining an accurate patient-specific spatial reconstruction, since a geometric change can lead to order of magnitude variations in blood

velocity.

2.3 Stents and Flow diverters

Choice of endovascular treatments remains criticial to patients outcome. The goal of the minimal invasive procedure is to induce thrombosis and prevent subsequent rupture.

As clipping and coiling are often dangerous or impossible for wide-necked intracranial aneurysms, alternative treatment options are desirable. One such alternative treatment is stent placement. Stents are metal device, which looks like a scaffold, is placed permanently around the neck of aneurysm to divert or alter the flow behaviour. Stent insertion alters flow paramaters such as residence time, wall shear stress thereby prmoting thrombus formation[82, 83]. Many authors have reported the importance of stent porosity and its effects on flow. A considerable difference is found in vortex location, intra-aneurysmal flow reduction and speed. [84, 85].

A flow diverter, although it looks like a stent, is markedly different in purpose and structure. The purpose of flow diverters is to redirect blood flow away from the aneurysm and to re-establish physiological flow conditions in the parent vessel. Though care should be taken that the vital side branches covered by the flow diverter, should not be eliminated. Therefore, due to their different purpose, the design requirements of a flow diverter as a vascular graft are vastly different from those of a stent.

An early investigation suggested that standard stents can act as flow diverters to occlude carotid and vertebral artery aneurysms while preserving the parent vessel [86, 87]. The idea was that stents will redirect the flow away from the aneurysm sac and the sluggish flow within the aneurysm will promote thrombosis of the aneurysm and thus exclude the aneurysm from the circulation. After some preliminary testing of the idea in laboratory animal models of aneurysms it became apparent that the concept works sometimes but not always. A optimization of the design properties of the device such as porosity, filament diameter and number of filaments is needed to achieve high, repeatable aneurysm occlusion rate.

The assessment of flow and flow changes induced by stent implantation is possible using elastic in vitro silicone models, as shown by Hoi et al. [81], where comparisons between simulations relying on Computational Fluid Dynamics (CFD) and Particle Image Velocimetry (PIV) measurements are presented for different geometries. It was proved that CFD simulations can closely match experimental measurements as long as both are performed on the same model geometry. Ford et al. [88] have compared CFD-predicted ve-

locity fields against those measured using PIV. They demonstrate that CFD not only captures the gross flow patterns but also many of the finer flow details and their associated cycle-to-cycle variations. Dorn et al. [89] used a side wall aneurysm model and LDV measurements to study the effect of different stent designs.

Many authors carried out CFD-based studies to understand the effects of stenting on the flow patterns [90, 91]. They compared different stent designs, porosity, filament size on simple geomteries and show a flow reduction into the aneurysm sac typically between 10 - 20 % [56, 84, 92].

Corresponding hemodynamic changes were assessed in [93, 94, 95]. Chopard et al. [96] described the clotting process in stented aneurysms using a lattice Boltzmann (LB) model, considering two types of aneurysm geometry, with the same neck size but with different aspect ratios. For some stent-aneurysm combinations, shear rate reduction is strongly correlated to the clotting fraction but, for other combinations, it gives a wrong trend. The employed model includes the transport of idealized red blood cells and platelets as well as an aggregation mechanism at low shear rate.

Lieber et al. [84, 90] has provided a major contribution to assess the potential of existing stents to act as flow diverters and sufficiently alter intra-aneurysmal flow. An initial study was conducted using laser-induced fluorescence (LIF) to examine the impact of woven nitinol stents of various porosities on the intra-aneurysmal flow patterns at two different flow conditions in the parent artery; namely, high and low hemodynamic settings. Four stents with porosities ranging from 76% to 85% were utilized. These observations provided a proof of concept that stenting alone dramatically alters intra-aneurysmal flow patterns. To complement the previous LIF studies he subsequently studied the effect of flow diverters on intra-aneurysmal flow patterns using Particle Image Velocimetry (PIV) in a side-wall aneurysm model [84, 97, 98]. In this study pulsatile flow over three helical stents with 76% porosity but different filament sizes was used to quantitatively determine the effect of stent filament diameter on intra-aneurysmal vorticity. For all the flow diverter, this study demonstrated that the intra-aneurysmal flow changes significantly after device implantation. The typical vortex and the fluid motion at the aneurysm dome seen in the nonstented case was barely noticeable after device placement.

To validate his previous PIV measurements the author quantified the intra-aneurysmal velocity patterns using computational models. Three-dimensional configuration were used to examine the local hemodynamics changes due to flow diverter placement in an aneurysm model using the commercial software package FIDAP. The model was studied under incompressible, pulsatile, viscous, Newtonian conditions with rigid boundaries. The results of

the CFD simulations showed considerable differences in flow patterns inside the aneurismal pouch. Flow activity inside the stented aneurysm model was substantially diminished and flow inside the parent vessel was less undulated and directed past the orifice. Results obtained with the CFD simulations compared favorably with the PIV experimental data. The simulations showed that the flow activity inside the aneurysm pouch is of an order of magnitude smaller than inside the parent vessel and it is further reduced after stenting.

2.3.1 Animal studies

Even today, some aneurysms cannot be treated with currently available methods of endovascular therapy. There is the risk of recanalization by coil compaction or regrowth of aneurysm. To close this treatment gap and constantly improve the therapeutic options, animal aneurysm models are needed. Animal models should be retained that approximately simulate human morphological and flow-related conditions of an intracranial aneurysm.

The elastase-induced aneurysm model in rabbits is at present the best animal model for in vivo validation of new materials and methods for the treatment of intracranial aneurysms. Its low morbidity and mortality, the relatively simple aneurysm induction for a high reproducibility and the human homology in terms of hemodynamics and of clotting system are advantages of this model over other available models for aneurysm [99, 100, 101]. The fact that its bifurcation aneurysm arterial wall structure is of comparable size and configuration to that of human aneurysm makes this model a good choice for corresponding studies.

Limitation of this model is that the Reynolds and Womersley numbers in the rabbit parent artery are about 2 to 3 times the corresponding values in human cerebral vessels. Another limitation is that the aneurysm sac itself is made of vein tissue such that the vascular response to the implant is unlike the response of arterial tissue [102].

In an effort to optimize flow diverting devices before implantation in the animal, Seong et al. [103] conducted experiments on a series of six flow diverters that were tested in an elastomeric replica of the elastase- induced aneurysm in rabbit. Flow through the model was analyzed using PIV. The nominal diameter of all the flow diverters was 5.5 mm and three nominal porosities of 65%, 70%, and 75% were tested. For each porosity, there were two devices, one with low and one with high (about twice as high) pore density. The mean hydrodynamic circulation after implanting the diverters was reduced to 14% or less of the mean hydrodynamic circulation before implantation. Mean kinetic energy in the aneurysm was reduced to 29% or

less of its value in the control. Overall, a high pore density flow diverter with 70% porosity yielded the best reduction of flow activity in the aneurysm of the six diverters investigated in this study.

After this detailed analysis of the literature, we can start describing our own contribution.

3. EXPERIMENTAL MEASUREMENTS AND VALIDATION

Part of this chapter has been submitted as journal article to Medical Engineering and Physics.
This chapter begins with information related to measuring the flow inside aneurysm models using Laser Doppler Velocimetry (LDV). The experimental setup used in the study is then described. Finally the validation of the computational procedure is presented.

3.1 Phantom models

Prototyping techniques (stereolithography) originally developed for building components from computer-aided designs (CAD) are now often applied for medical applications, in particular to build models of real human anatomy obtained from high-resolution multiplanar imaging data such as CT or MRI. Such models have found applications in radiotherapy and for surgical planning, particularly in the craniofacial and maxillofacial fields, and for neurosurgery. The quality of these in vitro models has progressed remarkably during the past decade and it is now possible to obtain highly accurate models and replicas for many arterial diseases [104]. Many phantom models used for past in vitro studies have a simple geometry and do not reproduce a physiological shape. There is a clear need for realistic in vitro models when evaluating endovascular techniques, testing new endovascular material, and for training purposes ahead of in vivo studies. Nowadays, many realistic phantom models are commercially available.

In the present study a Cerebral Aneurysm Artery model from the company Elastrat Sarl has been considered (Fig. 3.1.1). This phantom model contains three aneurysms, located on the anterior communicating artery (max. diameter: 9 mm, max. neck size: 4 mm), the posterior communicating artery (max. diameter: 8 mm, max. neck size: 5 mm) and the bifurcation of the middle cerebral artery (max. diameter: 10 mm, max. neck size: 7 mm). Direct access to each aneurysm is possible after removal of an obturator plugging the connection ($2-4$ mm funnel) to the model surface.

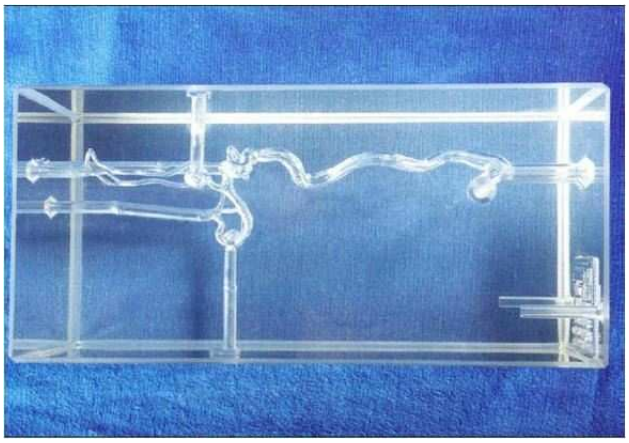

Fig. 3.1.1. Right internal carotid artery with 3 evacuable aneurysms (H+N-R-A-EV-003)

3.2 Blood analog fluid

Blood is a shear-thinning, non-Newtonian fluid that exhibits both viscous and elastic properties [105]. Because blood is opaque, generally not available in large quantity, and difficult to handle and store, it is desirable to use a transparent, blood analog fluid that has viscoelastic properties similar to blood and composed from stable and readily available materials. According to DIN EN ISO standards, testing shall be performed using a test fluid of isotonic saline, blood or a blood-equivalent fluid whose physical properties (e.g. density, viscosity at working temperature) shall be stated.

Several studies have been carried out with high molecular weight polymer solutions such as aqueous polyacrylamide (PAA), Xanthan gum and carboxymethylcellulose [106, 107, 108]. Although the viscous component of normal human blood has been matched fairly accurately with polyacrylamide solutions, the elastic component is much greater than that of blood [107, 109]. Aqueous Xanthan gum solutions have a lower elastic component than aqueous PAA solutions, but are still more elastic than normal hematocrit blood. Mann and Tarbell [109] reported experiments using an aqueous PAA blood analog fluid that produced wall shear rate waveforms that were significantly different from those of bovine blood under oscillatory flow conditions in an atherogenic curved artery model. They hypothesized that the substantial differences in wall shear rate waveforms where the result of large normal stresses present in polyacrylamide solutions that are not present in human blood [109]. They found that aqueous Xanthan gum solutions match better the shear thinning steady flow viscosity of human blood. They have normal

stress that are about one-third those of aqueous polyacrylamide solutions and do not produce abnormal wall shear stress waveforms in physiological flows. Thus, it appears that Xanthan gum solutions may provide a more suitable blood analog fluid than polyacrylamide solutions.

In the present study, aqueous Xanthan gum/glycerin solutions are used that accurately match both viscous and elastic components of the complex viscosity of low, medium and high hematocrit blood. The exact list of components can be found in the next section.

3.3 Refractive index matching

The main disadvantage of any optical technique like LDV is that the whole system (fluid and model) must be transparent and refraction-free. Therefore, an artificial fluid must be used instead of blood, which would absorb the laser light. Additionally, since two laser beams must be focused exactly onto a prescribed point of the model, any refraction must be prevented at material boundaries. Therefore, the employed liquid should fulfill three conditions simultaneously: it must be transparent at the frequency of the laser light, it must have the same refraction index as the silicone model, and it must have fluid properties as close as possible to blood.

Many fluids have been used in the past for matching index of refraction to common model materials such as Pyrex glass ($n = 1.474$), fused quartz ($n = 1.4585$) and silicone elastomers (around $n = 1.41$). From Lim et al. [110], the most commonly used blood analog is a fluid composed of 36.65% (vol.) glycerin in water to match the viscosity having a refractive index of 1.38 at 20°C. Typically, the refractive index of the blood analog mixture is adjusted with the use of chemical additives such as Sodium Iodide [111, 112], Sodium Thiocyanate (NaSCN)[111, 113, 114, 115], Potassium Thiocyanate (KSCN) [111], or Zinc Iodide (ZI) [111]. We matched the particle and fluid refractive indices in a two step process. First, we measured the refractive index of the model, and then found a fluid mixture with the same refractive index at a fixed temperature. Finding the fluid mixture with the desired refractive index was not as straightforward as in the case of the density. We mixed several fluids with the same, desired density, and refractive indices in a narrow range about the volume fraction average value. We measured the refractive indices of these various mixtures, and revised the composition until we found a mixture that matched the measured particle refractive index at temperature of 30°C.

The refractive index of the model liquid was adjusted by varying the proportions of the components. Refractive indices are typically measured

with a refractometer, of which there are many designs. They all utilise either a prism or a block, of known refractive index, through which monochromatic light is shone to determine the refractive index of a substance, usually placed on or between the prism/blocks. In the present case, the application of the emerging model serves as silicone block angle change on impact of the laser beam on the surface arranged at right angles to determine the refractive index was used. For comparison, the results were used that were obtained using an Abbe refractometer. The beam path in this experiment is shown in Figure 3.3.1. A reference beam is emitted from point R, which goes vertically through the block and marks the normal. The beam from the light source at point S meets at a certain angle on the surface of the block, where it is broken. Since the refractive index of air can be approximated to 1 the refractive index of the test material is given by:

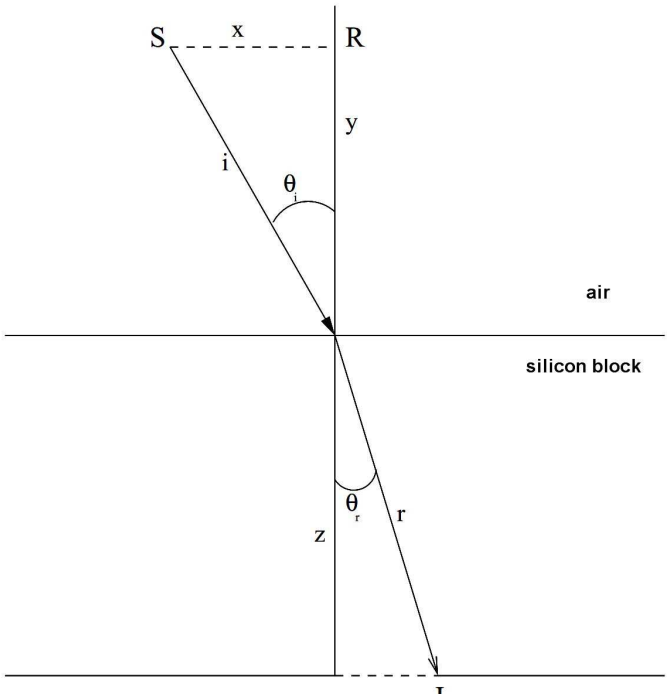

Fig. 3.3.1. Beam path of the refracted light in the transition of air into the silicone block

$$n = \frac{\sin \theta_i}{\sin \theta_r} \tag{3.1}$$

After many tests, the finally employed blood-analog fluid contains mainly water and glycerin (55%/45% mixture in volume). Xanthan gum particles

Fig. 3.3.2. Index of refraction as a percentage by volume of Sodium Chloride.

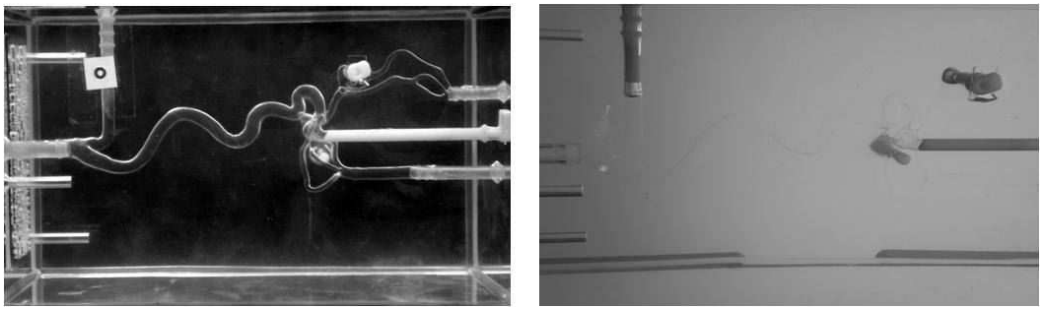

Fig. 3.3.3. Photograph of the employed phantom model filled with distilled water (left) and with our blood-analog fluid (right), leading to a perfect match of the refractive index.

with a size of 80 microns (0.2% volume) are then added to better mimic viscous properties of real blood. The addition of a (0.9% weight) of sodium chloride (NaCl) enables a matching of the refraction index of the mixture to the silicon material of the phantom (Fig. 3.3.2). Since the refraction index is temperature-dependent, the liquid mixture was maintained by a thermostat at exactly 30°C. The final mixture has a density of 1050 kg/m^3 and a viscosity of 0.0046 cp. The refraction index of the employed silicone model is equal to 1.43, as measured by the refractometer. Figure 3.3.3 shows the perfect matching obtained in refractive index when using our blood-analog fluid (right) by comparison with distilled water (left).

3.4 Experimental set-up

For all experiments, a closed circuit was realized as shown in Fig. 3.4.1. Most important for accurate predictions is the flow velocity, measured systematically with Laser Doppler Velocimetry (LDV). The working principles are explained in more details in section 3.5.

The velocity is measured within a small volume in which two laser beams of the same wavelength are crossed to form an interference pattern. A single component Laser Doppler Velocimeter (Model LDV-380, Polytec GmbH, Germany) with a receiver for the backward-scattered laser light was employed. The system incorporated a 100 mW laser diode. The measuring volume is of size 180 $\times$ 180 $\times$ 1900 μm^3 with a 4.3 μm fringe distance. For LDV, tracer particles must be added to the flow. Hollow glass particles (Topas GmbH, Dresden, Germany) with a density of 1.1 g/cm^3 and a mean

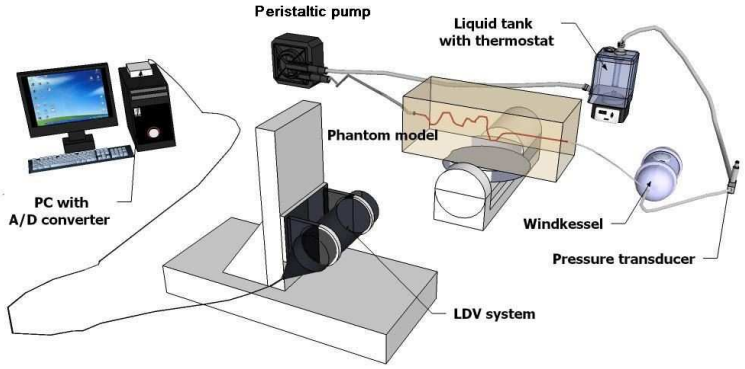

Fig. 3.4.1. Principle of the experimental setup

particle diameter of 1 μm are used for this purpose, since tests had shown that most other tracer particles deposit on the walls of the model, leading to measurement artifacts. The longitudinal velocity was measured within the phantom model by collecting 2000 samples at each position with LDV. Signal processing was realized by using the program development environment LABVIEW 8.0 from National Instruments.

3.4.1 Pump

The circulation of the blood-analog fluid in the installation is realized using a positive displacement pump as shown in Figure 3.4.2 (peristaltic pump model 520DU, from Co. Watson and Marlow, Cheltenham, England), that allows to approximately reproduce the real pulsatile conditions found in cerebral arteries (Fig. 3.4.4). The desired pressure interval is 125/75 mmHg. With these settings, the pump is running like a heart, beating 54 cycles per minute. The pump head rotates around 27 times per minute, but the pump head has two rolls, the current BPM is 54. In this way one cycle takes 1111 milliseconds. The pump was computer-controlled thanks to a LABVIEW script.

3.4.2 Windkessel

In order to obtain the desired range of pressure, an air chamber (windkessel) was placed at the outflow of the phantom model. Windkessel effect is a term used in medicine to account for the shape of the arterial pressure waveform

Fig. 3.4.2. Watson and Marlow peristaltic pump

in terms of the interaction between the stroke volume and the compliance of the aorta and large elastic arteries (Windkessel vessels).

The Windkessel effect helps in damping the fluctuation in blood pressure (pulse pressure) over the cardiac cycle and assists in the maintenance of organ perfusion during diastole when cardiac ejection ceases. The air chamber of the system is a stainless steel tank (see Figure 3.4.3).

Without the windkessel the minimum pressure is 20 mmHg and with the windkessel, the minimum pressure is 70-80 mmHg, depending on the opening of the tank. In this manner, the evolution of pressure with time could be closely adapted to the desired profile [116] as plotted in Fig. 3.4.4.

A 2-liter tank served as a main reservoir of working fluid as well as collection point for all phantom model outlets. The tank was placed inside a thermostat in order to maintain a constant temperature of the fluid, as needed for refraction index matching.

The phantom model consists of highly complicated and curved vessels. In this study, only the main velocity component (exemplified in Fig. 3.4.5) along the $X-Y$ plane was measured (see later Fig. 3.6.1). For this purpose, the whole phantom model is placed on a three-axis rotating system, allowing any angular position around the Z-axis (Fig. 3.6.1) within a range of $-50°$ to $+50°$. The laser and the phantom model are traversed with the help of a 3D motorized traverse system.

An integrated software that has been coded using LABVIEW allows the

Fig. 3.4.3. The pressure condenser/Windkessel

control of the movement of the laser, of the model on the rotating support, of the pump, and the whole LDV measurements. The three-dimensional geometry of the centerline of the vessels has been first coded into the computer as explained later, so that automatic measurements are possible. Measurement location, time, measured reference pressure and measured longitudinal velocity are stored together in a text file during the acquisition. After collecting the data along one plane the traversing system moves to the next position and, according to the centerline of the vessel inside the phantom, the rotating system adjusts all angles so that the measurement is again parallel to the external face of the model ($Z = \text{const.}$).

Before starting the measurements the first task was programming the pump. This pump creates the flow through the whirling of the pump head, made of two rolls, as illustrated in Fig. 3.4.6. As the rolls turn around they push the fluid into the tube. The tube is a special, thick-wall, flexible tube. To create the desired pressure waveform, the rotation speed is continuously adapted. For this purpose, one cycle is divided into 20 substeps [117] (Fig. 3.4.7).

After acquiring all the data, a post processing based on phase locking was used to reconstruct the time-dependent evolution of the velocity in the whole model. For this purpose, the pressure signal measured at the downstream section was employed as a reference. All velocities measured at the same

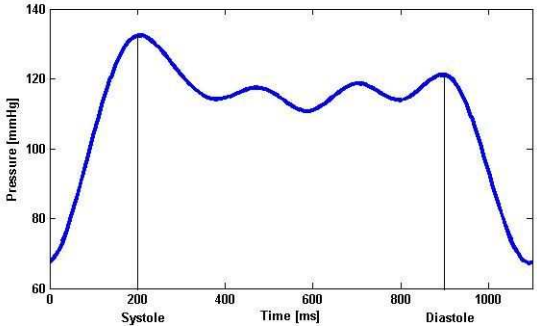

(a) Measured pressure

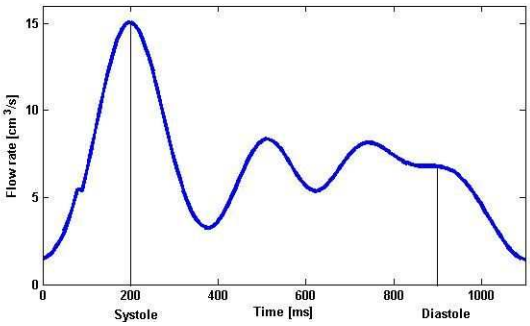

(b) Measured flow rate

Fig. 3.4.4. Measured, time-dependent pressure and inflow rate in the phantom model during one cycle.

Fig. 3.4.5. Representation of the main velocity component

Fig. 3.4.6. Pump head and rolls

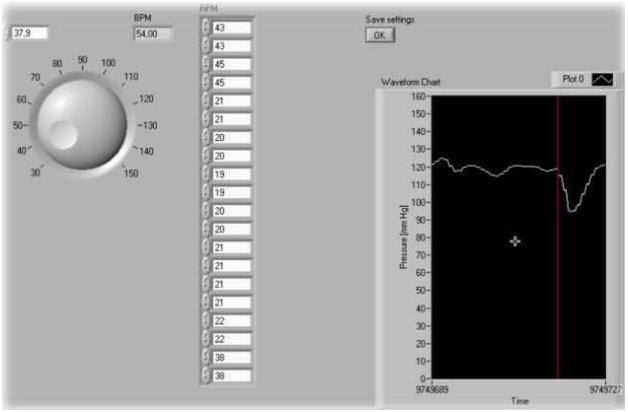

Fig. 3.4.7. The LABVIEW program: the cycle is divided into 20 parts with different rotation speeds

time for the same value of this reference pressure are averaged for several periods with 2000 samples per point, delivering the information finally used for later comparisons with CFD[118].

3.5 Principles of Laser Doppler Velocimetry

Laser Doppler Velocimetry (LDV) is an optical method to measure local velocities of transparent gaseous or liquid flows. It was first proposed by Yeh and Cummins in 1964. In comparison to traditional flow measurement techniques, e.g., the hot-wire anemometer or Prandtl probe, the LDV provides following advantages:

- The LDV method is non invasive.
- The determination of flow speeds is based on simple geometric correlations. Calibration measurements are not necessary.
- The direction of flow speed components being measured is determined by the optical arrangement.
- The LDV technique makes a high spatial and temporal resolution possible.
- The measurement distance ranges from centimeters to meters.
- Both instantaneous and averaged velocities can be measured.

The basic configuration of an LDV consists of a continuous wave laser, transmitting optics (including a beam splitter and a focusing lens), receiving optics (comprising a focusing lens, an interference filter and a photodetector), a signal conditioner and a signal processor. A general system configuration is shown in Fig. 3.5.1.

The laser beam generated from the laser system is divided into two identical laser beams. Those are forced to intersect at the measurement volume by the focusing lens. The photo detector receives light scattered from tracer particles moving through the measurement position and convert light intensity into an electrical current. Typically, the size range of tracer particles is between 1 μm and 10 μm. The scattered light contains a Doppler shift, which is proportional to the velocity component perpendicular to the bisector of the two laser beams. The noise from the signal is removed in the signal conditioner and signal processing. Then, the conversion factor between the Doppler frequency and the velocity can be calculated with a known wavelength of the laser light, and a known angle between the intersecting beams.

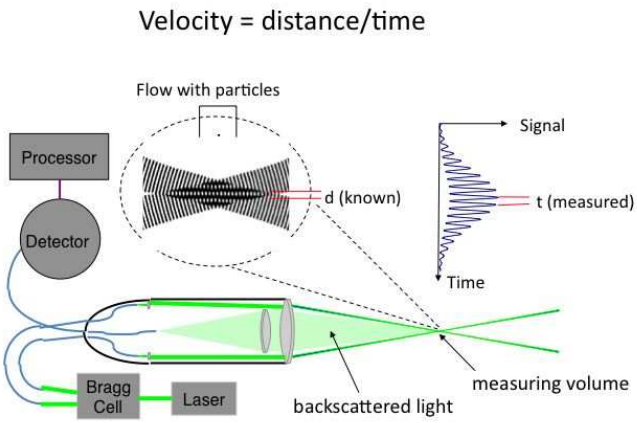

Fig. 3.5.1. System configuration of a LDV system in back scatter mode [119].

As done in the present study, back scatter mode is used most often, because it allows integration of the transmitting and receiving optics in a single head. Ideally, the particles should be small enough to follow the flow, yet large enough to scatter sufficient light to obtain a good signal-to-noise ratio at the photo-detector output.

3.5.1 The fringe model

When the two coherent laser beams intersect, they interfere with each other and form the measurement volume. Consequently, parallel planes of light and darkness are produced as shown in Fig. 3.5.1. The interference pattern consists of light and dark bands spaced at even intervals, also known as the fringe spacing. The fringe spacing δ_f depends on the laser wavelength λ and the angle θ between the two beams. The finge spacing is computed from the following relationship

$$\delta_f = \frac{\lambda}{2\sin(\theta/2)} \tag{3.1}$$

Particles passing through this interference pattern scatter light at a frequency that depends upon the particle velocity and fringe pattern spacing.

The particle velocity, u, is determined from the frequency of scattered light measured at the photodetector f_d, and the known spacing of fringe pattern as given by

$$u = \delta_f \cdot f_d \tag{3.2}$$

A drawback of the LDV-technique described so far is that negative velocities will produce negative frequencies. To handle this problem, a Brag cell is introduced in the path of one of the laser beams. To distinguish between positive and negative flow direction, frequency shift is employed. The Bragg cell adds a fixed frequency shift, f_0, to the diffracted beam, which then results in a measured frequency off a moving particle of

$$f_D \cong f_0 + \frac{2\sin(\theta/2)}{\lambda} u \tag{3.3}$$

and as long as the particle velocity does not introduce a negative frequency shift numerically larger than f_0, the Bragg cell will thus ensure a positive Doppler frequency f_D. In other words the frequency shift f_0 allows measurement of velocities down to

$$u > -\frac{\lambda f_0}{2\sin(\theta/2)} \tag{3.4}$$

without any directional ambiguity.

3.6 Measurement results

The LDV measurements have been postprocessed to extract the longitudinal velocity at different position planes within the phantom model shown in Fig. 3.6.1, following the procedure described previously.

LABVIEW programming was used to store the instantaneous velocity and pressure measurement as an ASCII file. Velocity values are determined by auto-correlation analysis using FFTs (fast Fourier transforms) .

Several criteria are adopted to check the validity of the measured velocity values. Velocity values which are outside a prescribed range are rejected. In the present study, the percentage of non-valid data is less than 1%.

As mentioned earlier the phantom model has one inlet and two outlets. The LDV measurements have been limited to the path leading from inlet to

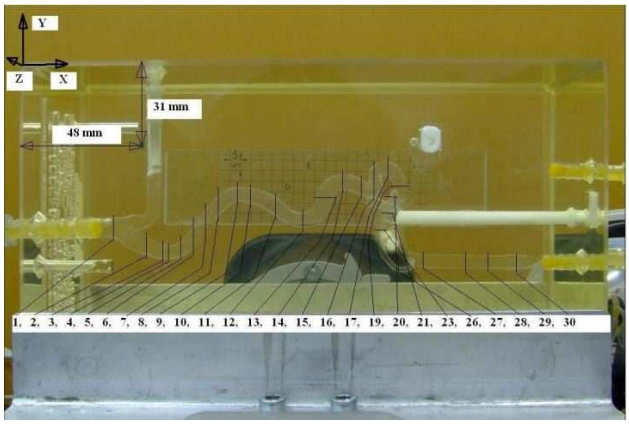

Fig. 3.6.1. Measurement planes within the phantom model

outlet1, neglecting the path to outlet2 (see Fig. 3.7.5). For this reason only the former is considered for later comparisons.

The velocity field in the neck of the aneurysm and near the wall could not be measured due high scattering. Some tracer particles stick to the wall resulting in an artificial increase in scattering due to zero velocity signals.

The cardiac cycle can be separated into two major phases referred to as systole, which is the period of contraction, and diastole, during which the heart relaxes and fills with blood ready for the next cycle. For a convenient description the same concepts are used in the present case, even if the pulsation induced by the peristaltic pump does not reproduce exactly the corresponding pressure variations found in human patients. Systole and diastole are defined for the present set-up in Fig. 3.4.4.

After the data was collected at one plane the traversing system moves to the next position and according to the centerline of the vessel inside the phantom the rotating system adjusts the phantom so that the measurement is made parallel to the flow direction. For each plane, the pressure measurements downstream the outlet are considered as reference signals, to assign phases. As shown in Figure 3.6.2, a relatively larger scatter remains, due to cycle-to-cycle variations of the employed peristaltic pump. This will lead to relatively large error bar in the experimentals results shown later.

Fig. 3.6.2. Phase averaged velocity measurement

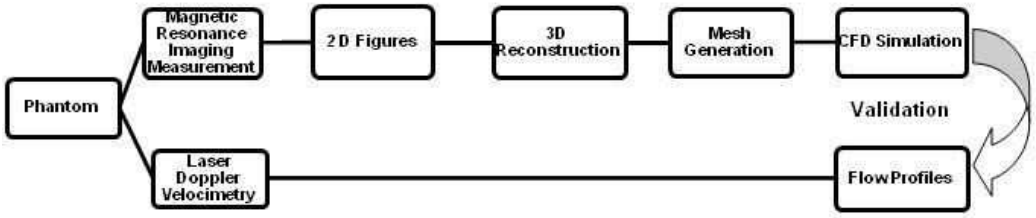

Fig. 3.7.1. Steps allowing a validation of the computational model using measurements in a phantom model.

3.7 Validation of numerical model

The simulation workflow (Fig. 3.7.1) is a chain that begins with the segmentation of the scanned model leading to tomographic images, then to 3D reconstruction. From the segmented data, an initial geometrical model is created and has to be preprocessed. Then, high-quality meshes required for running and converging the simulations are generated. Reliable physical models must be defined in order to determine the system of equations to be solved. Realistic initial and boundary conditions, based on measured data, are required for the solution of the system of partial differential equations. Mathematical models based on appropriate numerical methods need to be defined in order to discretize the system of equations and perform the simulations. Finally, proper representation and evaluation of the results is necessary to visualize, analyze and quantify the parameters of interest.

3.7.1 Magnetic Resonance Imaging

In order to automatize the measurements and to enable computer simulations of the exact model geometry, the vessel geometry has been first accurately determined by MRI. Magnetic Resonance Imaging measurements were performed on a 7-Tesla whole body MR-System (MAGNETOM 7T, Siemens Medical Solutions, Germany) in an 8-channel coil (Rapid Biomedical, Germany) using the same phantom model. The MR-data was acquired using a gradient echo sequence with the following scan parameters: image matrix = $288 \times 512 \times 240$, FoV = $144 \times 256 \times 120$ mm, $0.5 \times 0.5 \times 0.5$ mm voxelsize, TR / TE = 20.0 ms / 7.67 ms, FA = 15°, bandwidth = 170 Hz/Px, 4 averages. The phantom was filled in that case with a saline solution (0.9%) which was doped with gadolinium (GdCl3, 0.2 mmol/l) to simulate in vivo T1 / T2. Due to the difference in the fluids, no direct quantitative comparison is possible between LDV and MRI measurements of flow velocities yet.

3.7.2 Surface mesh generation from MR measurements

Segmented volume data obtained from MR scans was used to reconstruct a surface mesh of the vascular structure of the phantom, enabling CFD simulations of exactly the same model. The segmentation was carried out based on the high-resolution data set by a threshold-based method followed by connected component analysis. The segmentation process is performed in the discrete and sampled volume space. Due to this fact, aliasing artifacts are introduced onto the reconstructed surface. Simple smoothing procedures (e.g., Laplacian smoothing) degenerate vessels and alter the topology. Important details are preserved by representing them by more points. To reduce the number of created triangles, their size can be linked to local surface curvature. In that case it is important to create enough surface triangles and to ensure that the difference in size of neighboring triangles is small enough in order to later allow the creation of an adequate simulation grid based on the surface mesh. A detailed description of the employed surface reconstruction pipeline is given in [120]. The result is a smooth surface model with preserved detail information and optimized triangle quality. Thus, the resulting surface mesh is a perfect input for further mesh generation (Fig. 3.7.2), as needed for CFD.

3.7.3 Numerical setup

The result of the 3D reconstructed data of the phantom model from MR is a surface mesh which is saved in Stereolithographic (STL) format as the initial geometry for the CFD simulation. The STL geometry is then imported into a commercial package (ICEM CFD 12, ANSYS, USA) for the generation of high-quality body-conforming volumetric grids composed of tetrahedral elements and prism elements near the wall in order to obtain a better resolution. Meshing is a challenging as well as an important task because the quality of the mesh affects both the accuracy of the solution and the requirements for computing time and run-time memory [121]. Generating a high-quality mesh is difficult since numerical methods require elements which cannot be easily constructed in complicated flow domains. Hence, the complete physical domain is first divided into a number of simply-shaped regions or elements, referred to as individual blocks, each of those being meshed independently with tetrahedra elements as seen in Fig. 3.7.2 (top). The numerical mesh has been systematically refined using prism elements near the walls (Fig. 3.7.2, bottom), in order to allow proper resolution of the large velocity gradients found in that region. This is absolutely necessary to obtain a correct estimation of the wall shear-stress [121]. A total of around 2 million volume

grid elements have been finally considered for the flow simulation. For the present computations, all findings documented in [121, 122] have been fully taken into account, together with standard best practice guidelines for CFD [123].

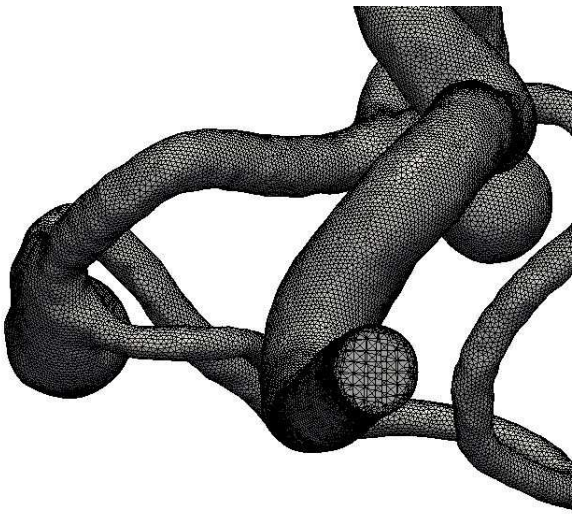

(a) Generated surface mesh

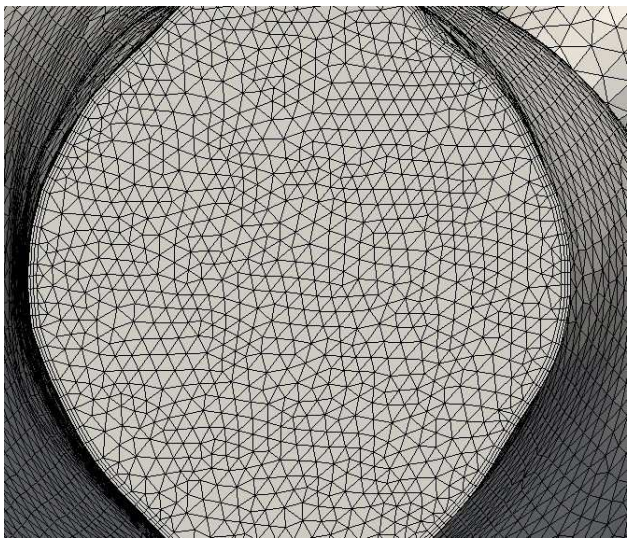

(b) Close up view of the volume mesh showing prism elements near the wall region

Fig. 3.7.2. Overview of surface and volume mesh

Inflow conditions are essential as well for CFD modeling. The inlet flow was described by a uniform, pulsatile flow velocity profile obtained from the

in vitro LDV measurement flow rate data at the inlet of the model, as shown in Fig. 3.4.4. All boundary nodes were set to zero velocity in order to enforce a no-slip boundary condition. All walls were assumed to be rigid. The model has two outlets. The relative volumetric flow rate at each outlet is imposed numerically through a value-weighted outlet boundary condition following the measurement results obtained from MRI, as described previously.

A hundred and ten time steps of constant length were used for the time discretization of the simulation per cycle. A stabilized finite-volume method with a second-order discretization and time-stepping algorithm was used to compute the flow solution using ANSYS-Fluent. The integration was carried out during 4 cycles of pulsatile flow in order to obtain finally a fully periodic solution. Comparisons with experimental measurements have been done for the last cycle. All numerical simulations have been carried out on the Karman computing cluster in Magdeburg equipped with 68 dual nodes (2.1 GHz AMD Opteron quad processors) using a high-speed Infiniband interconnection. Typical computation time for one cycle is 7 hours using 8 computing cores in parallel.

3.7.4 Governing equations and assumptions

The computational simulations are performed using a commercial finite volume CFD software (ANSYS-Fluent V12.0, ANSYS, USA) solving the Navier-Stokes equations in three dimensions. The solved equations physically describe conservation of mass and of momentum (second law of Newton). For an incompressible fluid they read:

$$\vec{\nabla} \cdot \vec{u} = 0 \tag{3.1}$$

$$\left(\frac{d\vec{u}}{dt} + \vec{u} \cdot \vec{\nabla}\vec{u}\right) - \nu \cdot \vec{\nabla}^2\vec{u} + \frac{1}{\rho}\vec{\nabla}p = 0 \tag{3.2}$$

with t the time, $\vec{u}$ the velocity of the fluid, $\vec{\nabla}$ the gradient symbol, ν the (constant) kinematic viscosity of the fluid, ρ the (constant) density of the fluid and p the pressure. Since the flow is considered incompressible and isothermal, a conservation equation for energy is not needed.

The blood analaog fluid used for the experiment has material properties that matches well with that of a Carreau model. It is a widely used and effective model for shear-thinning fluids. The Carreau model tries to describe a wide range of fluids through a curve-fit that pieces together functions for both Newtonian and shear-thinning non-Newtonian fluids. For the numerical simulation the material settings was used according to the following equation

$$\mu = \mu_\infty + \frac{(\mu_0 - \mu_\infty)}{(1 + (\lambda_t \gamma)^a)^{\frac{1-n}{a}}} \tag{3.3}$$

where $\lambda = 10.3$ s, zero strain viscosity $\mu_0 = 0.639$ cP, infinite strain viscosity $\mu_\infty = 0.0046$ cP, empirical exponent $n = 0.35$, constant $a = 2$.

3.7.5 CFD results

CFD results are exemplified in Fig. 3.7.3, showing for a fixed time selected streamlines together with a color coding of the flow magnitude along those streamlines. Additionally, Fig. 3.7.4 shows the local velocity magnitude for selected planes within the model, used later for comparisons with measurements. These results correspond to peak pressure at model outflow.

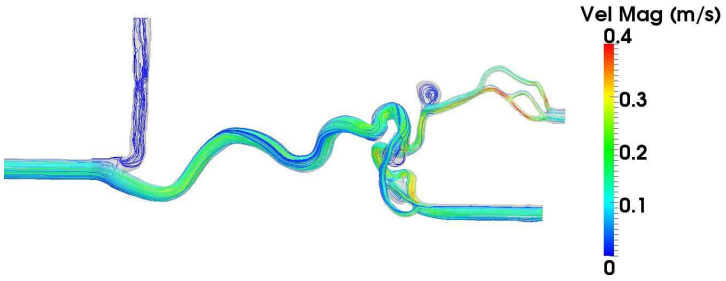

Fig. 3.7.3. Example results from CFD simulations: instantaneous streamlines and color coded velocity magnitude at late diastole

3.7.6 Comparisons between experiments and simulations

It is now possible to validate the CFD results by direct comparison with the measurements. In what follows, this comparison is shown along seven selected planes, represented in Fig. 3.7.5. Further planes have been considered as well, revealing similar behavior, so that they are not included in the further discussion.

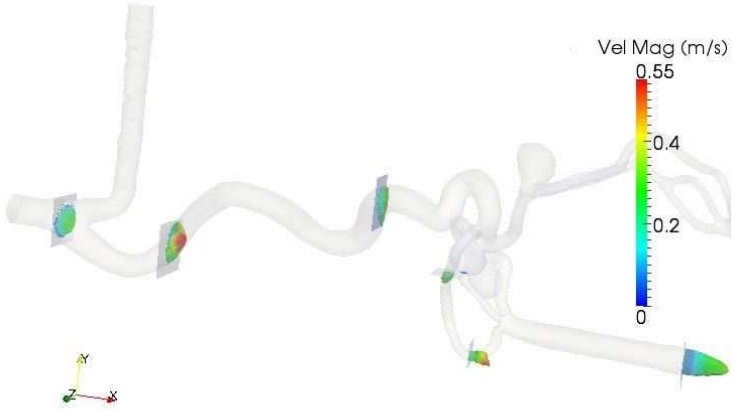

Fig. 3.7.4. Example results from CFD simulations: instantaneous velocity magnitude at different planes within the phantom model at peak pressure

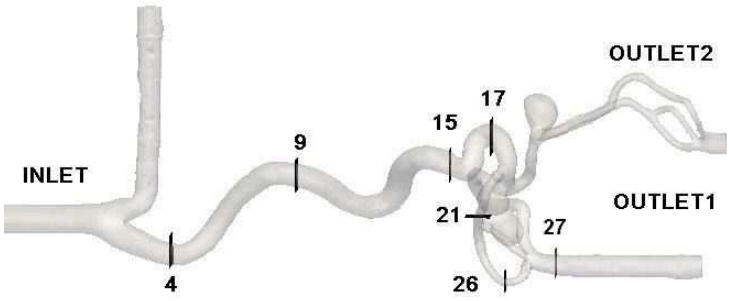

Fig. 3.7.5. Positions at which comparisons between CFD and LDV are shown

All comparisons have been carried out using the software Matlab and Paraview. The resulting flow rates were computed both for experiment and simulation by integrating the obtained velocity over the cross section. For this integral quantity, the difference between CFD and experimental measurements is always below 10%.

Figures 3.7.6 to 3.7.9 show selected comparisons of the instantaneous magnitude of the velocity in the $X - Y$-plane along a cross-section of the model at different instants. For all results, the measurement uncertainty is shown as error bars. Note that this large measurement uncertainty is not primarily associated to LDV, but mainly to the employed peristaltic pump, leading to relatively large cycle-to-cycle variations.

Considering these figures it is obvious that the velocity field is computed with a good accuracy within the whole phantom model. The comparison is very good for all the presented planes (4, 17, 21, 27) and matches experimental values well. The same holds for the other planes (not shown). It is however noticeable that the agreement is slightly worse in plane 27, i.e., near the outflow. This is probably due to the growing influence of the employed boundary condition in the CFD when approaching outlet1.

As complementary information showing flow topology, Fig. 3.7.11 displays instantaneous surface plots of longitudinal velocities along three planes at peak systole and at late diastole. Note that the color scales and perspectives were adapted for each location in order to maximize visibility and resolution. A very good agreement is systematically observed in terms of velocity and of flow topology at the three slice locations. Both simulation and LDV results show peak velocities near the middle of the vessel with very low velocities along the wall, as expected. The resulting topology is quite different from plane to plane and as a function of time, and is well reproduced by CFD. For instance, a marked crescent-shaped profile is found both in CFD and LDV along Plane 9, particularly at peak systole. Confirming previous observations, the largest differences are observed in Plane 26, i.e., again near the model outflow.

3.8 Conclusions

In order to check, develop and improve treatment options for cerebral aneurysms, accurate computational models are needed to describe in a realistic manner the associated hemodynamics and flow modifications. To quantify the accuracy of such simulations, comparisons with experimental measurements in a phantom model appear to be the most promising solution. For this purpose, the velocity field has been measured in a true-to-scale silicon phantom

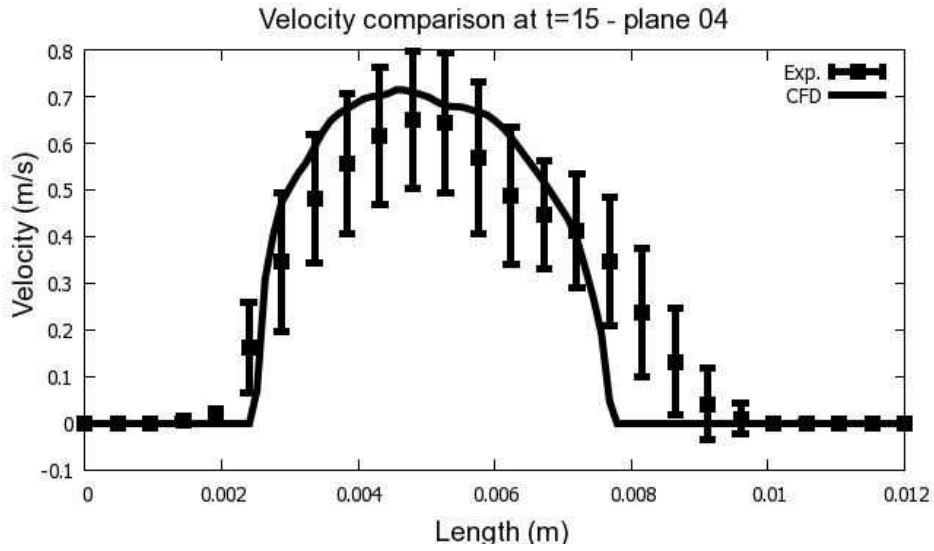

(a)

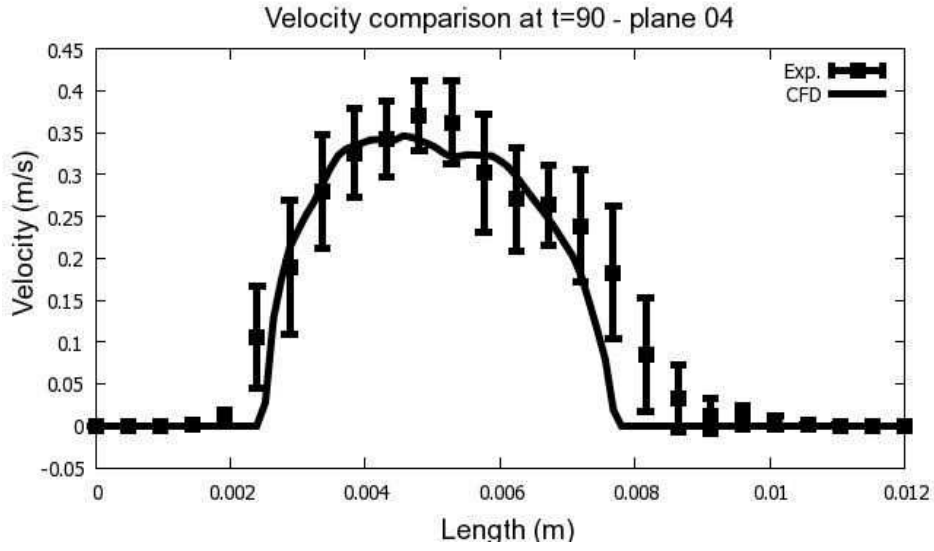

(b)

Fig. 3.7.6. Comparison of velocity magnitude in a cross-section of plane 4. (a) LDV vs. CFD at peak systole. (b) LDV vs. CFD at late diastole. Please note the different scales.

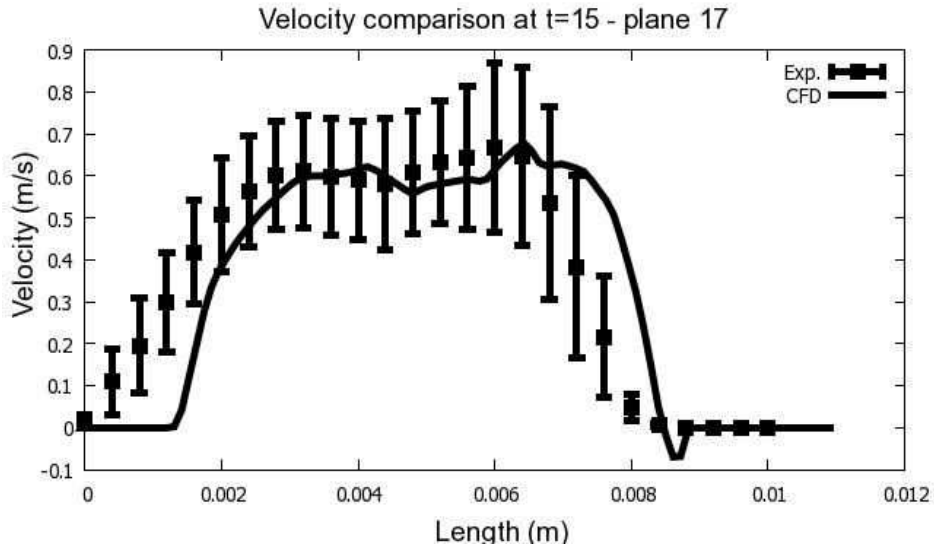

(a)

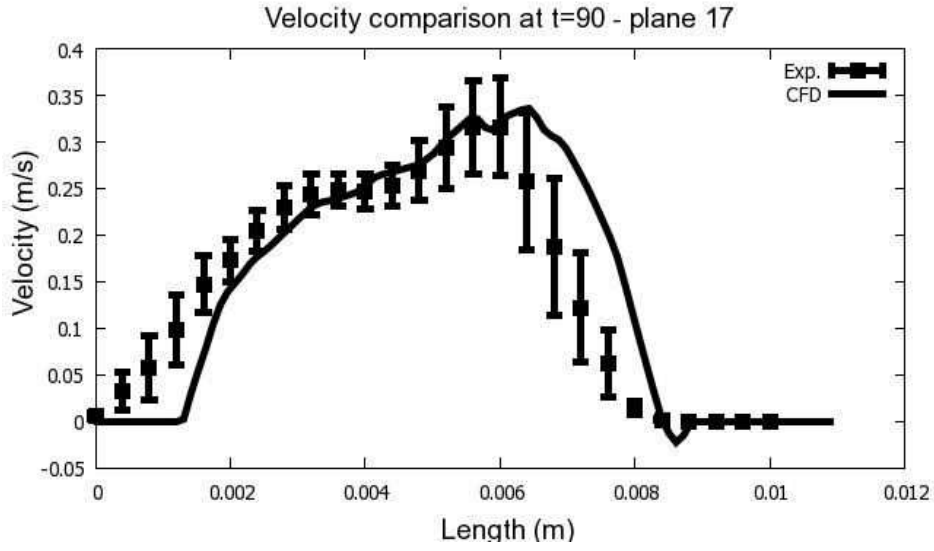

(b)

Fig. 3.7.7. Comparison of velocity magnitude in a cross-section of plane 17. (a) LDV vs. CFD at peak systole. (b) LDV vs. CFD at late diastole. Please note the different scales.

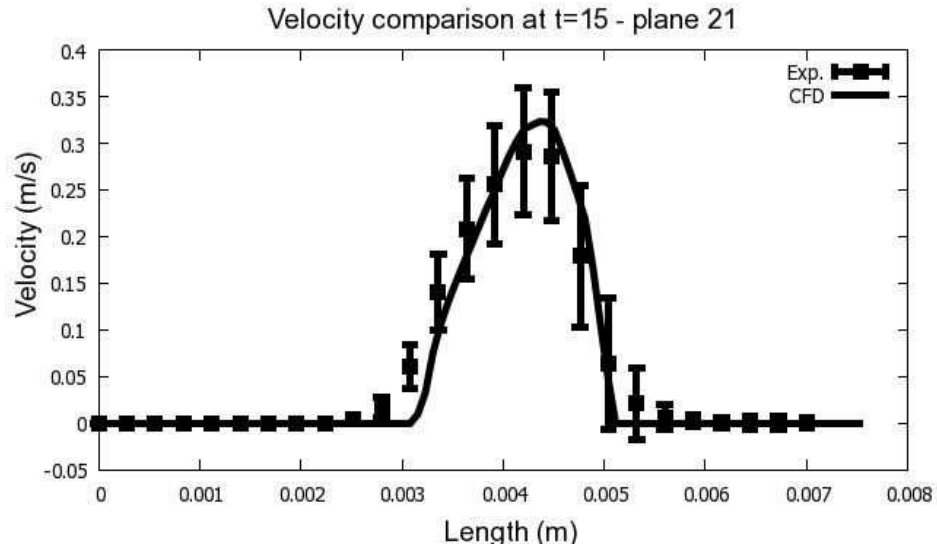

(a)

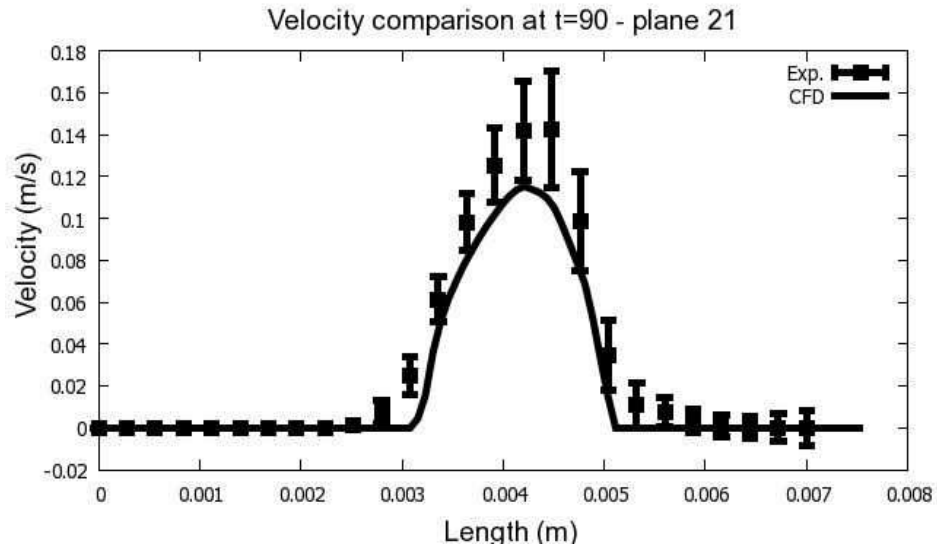

(b)

Fig. 3.7.8. Comparison of velocity magnitude in a cross-section of plane 21 (a) LDV vs. CFD at peak systole. (b) LDV vs. CFD at late diastole. Please note the different scales.

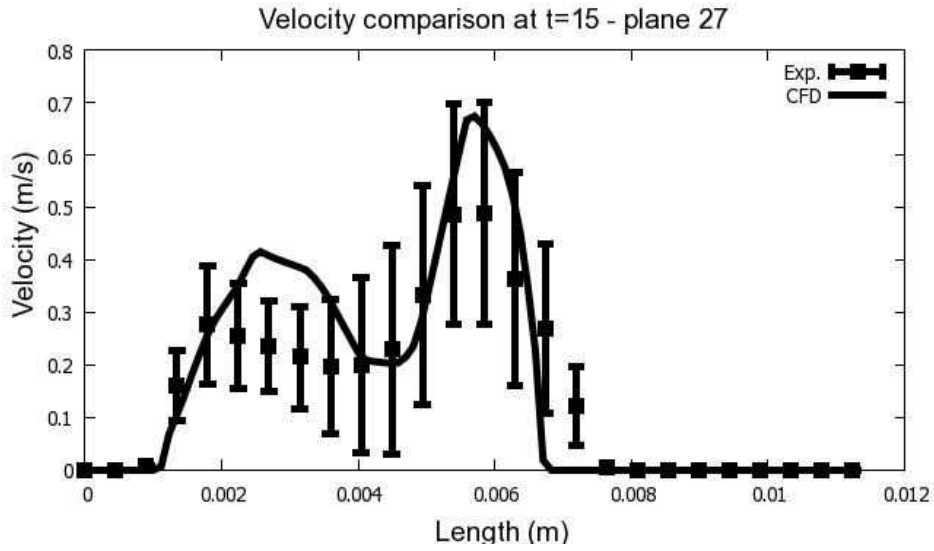

(a)

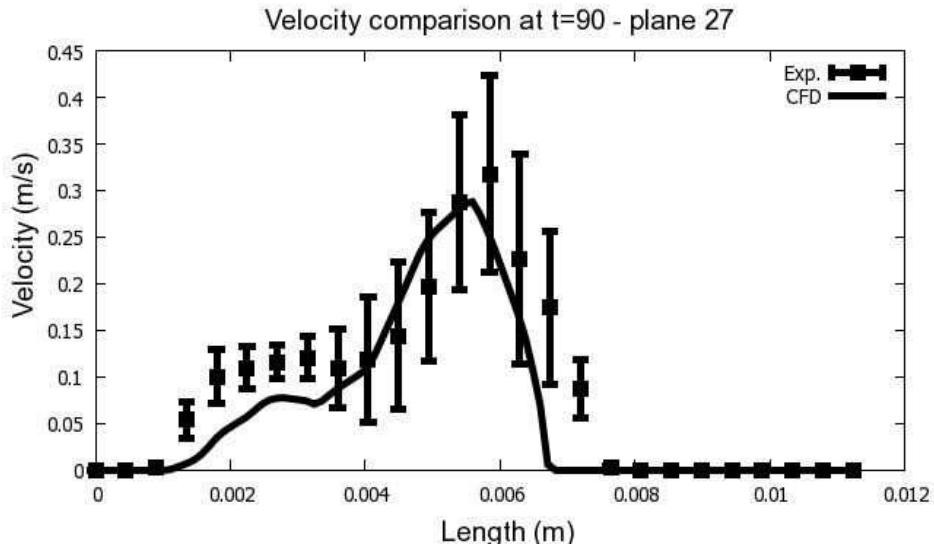

(b)

Fig. 3.7.9. Comparison of velocity magnitude in a cross-section of plane 27. (a) LDV vs. CFD at peak systole. (b) LDV vs. CFD at late diastole. Please note the different scales.

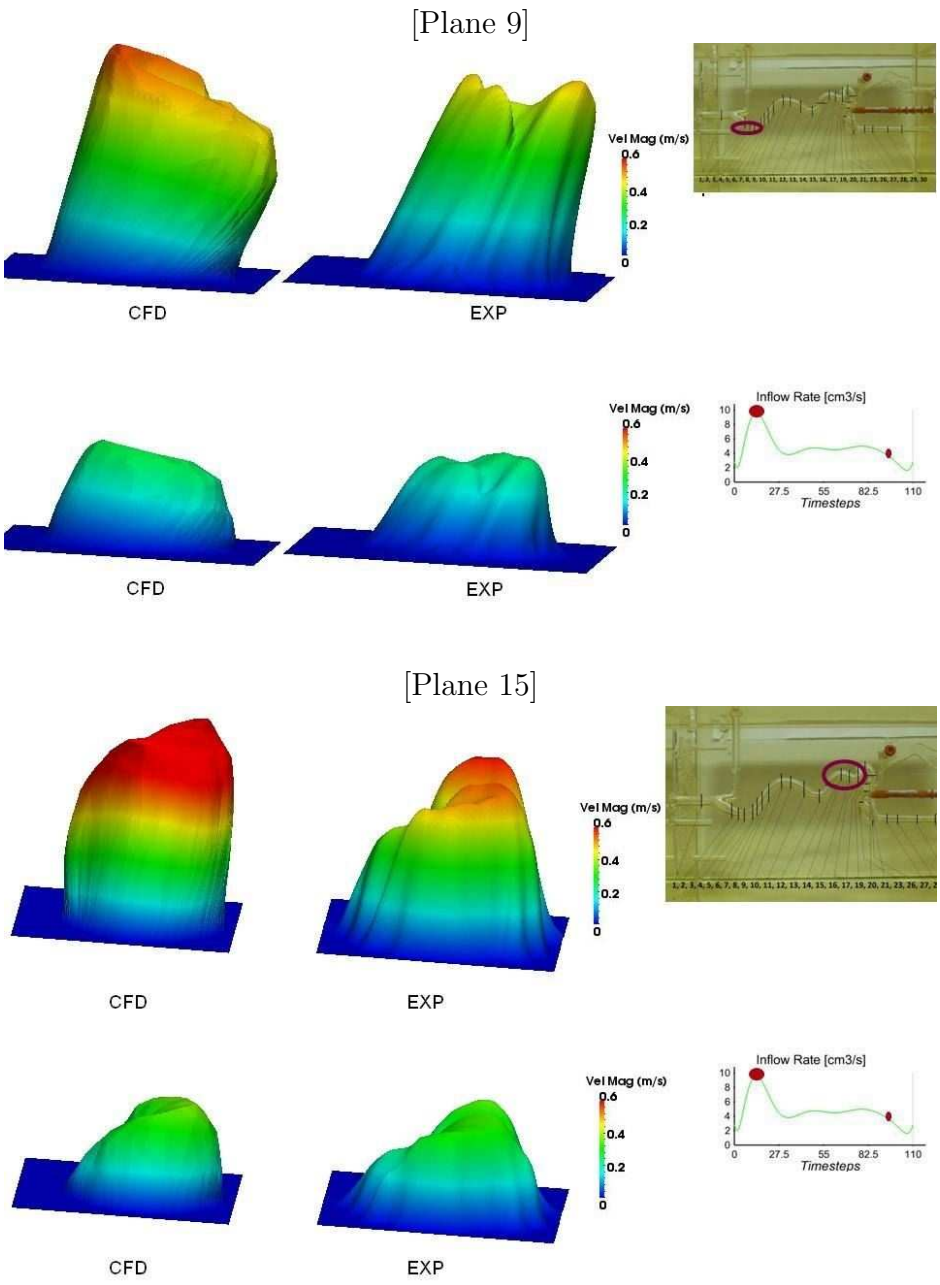

Fig. 3.7.10. Surface plot comparisons of velocities. All instantaneous comparisons are presented at two time points: (1) peak systole, top and (2) late diastole, bottom. Results from three planes obtained by CFD (left) versus LDV measurements (right). Note that different color maps have been used in each plane in order to increase resolution.

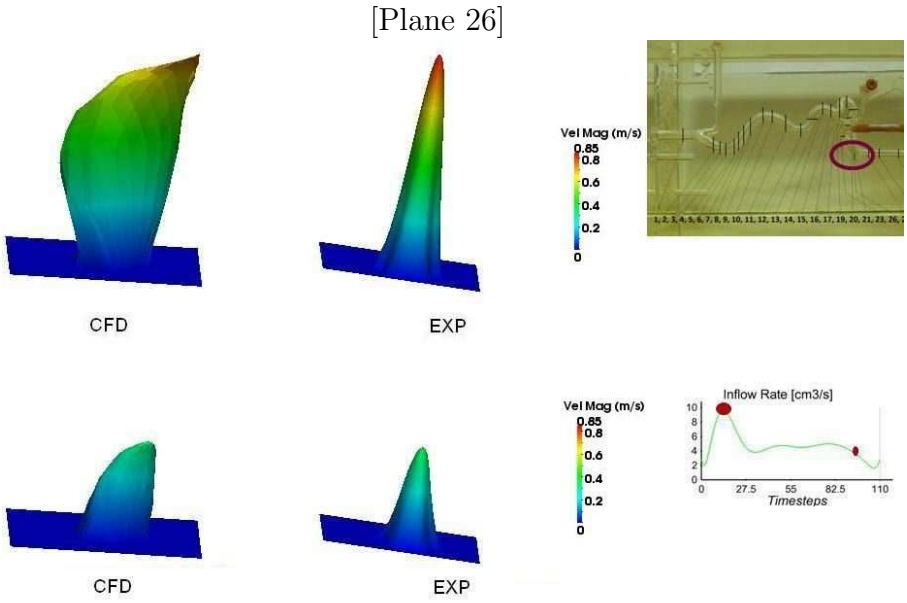

Fig. 3.7.11. Surface plot comparisons of velocities. All instantaneous comparisons are presented at two time points: (1) peak systole, top and (2) late diastole, bottom. Results from three planes obtained by CFD (left) versus LDV measurements (right). Note that different color maps have been used in each plane in order to increase resolution.

model using Laser Doppler Velocimetry. Corresponding measurements are still highly challenging, since refraction index matching is needed together with seeding particles, which may deposit on the model walls after some operation time. Most important, cyclic flow variations induced by the employed peristaltic pump lead to relatively large fluctuations and hence to corresponding measurement uncertainties. However, when carried out with great care, LDV measurements do deliver data suitable for quantitative comparisons.

Overall, the CFD results appear to describe the velocity field in the phantom model quite accurately, both concerning flow topology and velocity magnitude. This has been shown by direct comparisons along seven different planes in the model, both before and after the aneurysm. The only noticeable discrepancies are observed near the outflow of the model, as explained in the previous section. As a whole, this study demonstrates that CFD indeed offers a reliable prediction of unsteady hemodynamics in realistic patient geometries with an acceptable computational time. Given the importance attributed to local hemodynamic factors that can hardly be measured, such as shear stress, in the development of aneurysm, CFD predictions offer a good alternative to quantify patient-specific risk of rupture and to assess the best possible treatment options. Shear stress might be particularly important to understand the physiologic evolutions and thrombus formation. The good comparison of the flow patterns predicted by simulations with data measured by LDV indicates the validity of this method. As such the combination of CFD with experimental measurements appears to be a promising tool for validation studies. In addition to LDV, Particle Image Velocimetry (PIV) is now considered in order to obtain directly an instantaneous image of the velocity field in a plane, so that the perturbations induced by cycle-to-cycle variations will be less important. Based on such combined studies, it should become possible to develop better treatment options, for instance optimal flow diverters supporting thrombosis.

4. VIRTUAL STENTING ON MODEL GEOMETRY

Part of this chapter has been published as journal article in the Journal of Biomechanical Engineering.

Classical treatments for saccular aneurysms have a morbidity or mortality rate as high as 17.5% after 30 days [124]. Medical specialists are therefore confronted with extremely difficult decisions to make upon detection of an unruptured cerebral aneurysm, which now is more frequently revealed by modern visualization diagnostics like CT scans or MRI:

1. What is the risk of rupture and is it sufficiently high to justify an intervention?

2. What is the expected benefit of the intervention and how can it be maximized?

Numerous studies have been dedicated to the first issue (e.g., [125, 126]). Still, many questions remain unanswered. Hemodynamic stress is probably not sufficient to explain rupture, since bursting occurs most frequently at the dome and rarely near the neck [127]. Wall composition and properties are certainly of essential importance to predict quantitatively the risk of rupture [37]. In the present chapter, the emphasis is clearly set only on the second aspect and hence on modifying hemodynamics in a desired manner thanks to an intervention. Therefore, flow modifications in a cerebral aneurysm will be quantified using several implants presently available in the commercial market.

In current practice, the size of the aneurysm sac is the main criterion in deciding whether treatment should be performed or not. Usual treatment options have been described in Chapter 1. Clipping consists of placing a clip around the aneurysm neck, preventing blood from flowing into the aneurysm. Depending on the position of the aneurysm, it cannot always be employed or is associated with high perioperative morbidity and mortality. Due to the general trend towards minimal invasive treatments, it tends to be replaced by alternative techniques. Coil embolization consists of filling the aneurysm with a platinum coil in order to decrease blood circulation within the aneurysmal pouch and promote thrombus formation in the aneurysm.

Though efficient, considerable risks remain like coil protrusion or escape into the parent vessel during or after intervention, plus a non-negligible risk of aneurysm rupture when filling out the aneurysm sac with coils. In addition, coil-treated aneurysms may remain incompletely occluded with a persisting risk of rupture. Prior to coiling a stent may be placed in the parent artery, especially in case of wide-necked aneurysms, in order to reduce the risks mentioned previously. This approach is recommended for wide-neck aneurysms, which are defined as having a neck larger than 4 mm or a dome-to-neck ratio below 2 (see Fig. 2.2.1 on page 21).

In order to quantify the influence of implants on the aneurysmal flow, the present numerical study investigates in detail flow patterns and hemodynamic modifications for side wall, wide-neck aneurysm models. The impact of stents with different characteristics and porosity will be explored to obtain a quantitative understanding of flow modifications in these idealized aneurysm models. Key hemodynamic parameters such as the reduction in intra-aneurysmal flow and turn-over time will be evaluated by post-processing the results. Since it is known that the geometric properties of the aneurysm strongly affect its hemodynamics, the most important parameters (aneurysm size, dome-to-neck ratio and curvature of parent vessel) will be varied in a systematic manner in order to check the generality of the observations. Finally, 72 different configurations have been considered in the present work with three different, commercially available stents and flow diverters.

4.1 Configurations and Methods

As explained previously, the blood flow in and around the aneurysm completely depends on the geometry. As a consequence, it is essential to consider a variety of relevant geometrical configurations in order to obtain findings with a high generality. For this purpose, the simulations presented in this work that rely on Computational Fluid Dynamics will be repeated in a systematic manner while varying the most important geometrical parameters for the aneurysm, the blood vessel, and the stent as described next. Afterwards, the main assumptions and equations underlying the numerical study will be presented.

4.1.1 Virtual patient geometry

It is clear that aneurysm hemodynamics is completely modified by the specific geometry of the parent vessel in the vicinity of the neck. Hence, the present three-dimensional CFD simulations will consider two different typical geometries for that purpose: the sidewall aneurysm model will be placed

either on a straight parent vessel, or on a curved parent vessel at the level of the bend (Fig. 4.1.1). Three different aneurysm diameters D with values of 8, 12 and 16 mm will be analyzed. The neck size N is then varied accordingly in order to obtain dome-to-neck ratios D/N of either 1.4, 1.6, or 1.8. As discussed previously, these values have been chosen based on the results documented in [65].

Finally, 18 different, virtual patient geometries are considered (three diameter values, three dome-to-neck ratios, either straight or bent vessel, see also Table 4.1.1). All are produced using Autodesk Inventor (Autodesk, San Rafael, USA). The contact lines between the spherical aneurysms and the vessel walls are rounded with a radius of 0.2 mm in order to obtain a more realistic model geometry, contrary to most published studies in which this interface was considered as a sharp edge; this is physiologically impossible and could lead to large flow modifications, in particular concerning wall shear stress.

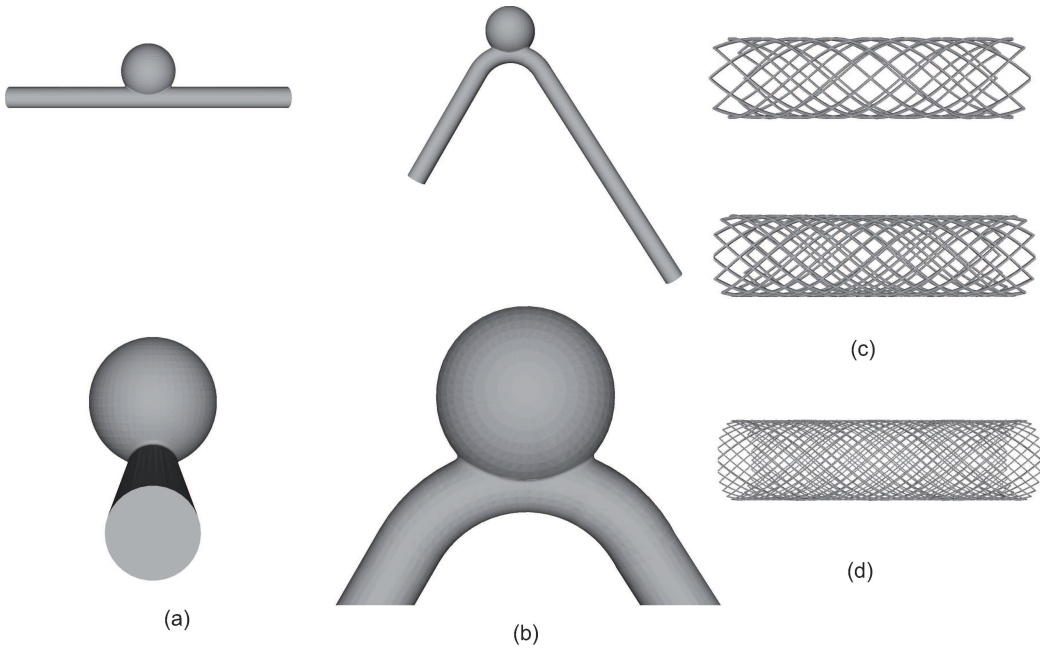

Fig. 4.1.1. Geometrical configurations considered in this study, from left to right and top to bottom. (a) Sidewall aneurysm model with straight parent vessel: top, lateral view; bottom, cross-section. (b) Sidewall aneurysm model with curved parent vessel (inner bend angle of 60°). (c) Geometry of Neuroform3 stents: top, high porosity (NHP); bottom, low porosity (NLP). (d) Geometry of the Silk4, 0 flow diverter.

4.1.2 Stent geometry

Three different, commercially available stents and flow diverters currently in use for aneurysm treatment are considered in the present work (Fig. 4.1.1, right). The first one is a Neuroform3 stent (Boston Scientific, USA) with 16 braided wires, later denoted as Neuroform high porosity (NHP). The second one is again a Neuroform3 stent but with 24 braided wires, called Neuroform low porosity (NLP). The thickness of the Neuroform wires is 0.1 mm for both stents. The third configuration is the Silk4, 0 flow diverter (Balt Extrusion, Paris, France) with 48 high-density braided wires, composed of two different wire thickness (0.05 mm and 0.03 mm), later simply denoted as SILK. All implants considered are produced of a round-wire braid reinforcement with a total implant length of 10 mm and an external diameter of 4 mm, equal to the internal diameter of the parent vessel. As a consequence, the vessel and implant surfaces are directly in contact with each other in the simulation, but without any deformation (other than bending the stent in the case of the bent vessel, parallel to the vessel wall). The middle of the implant always coincides with the center of the aneurysm neck.

4.1.3 Summary of cases

In the present, systematic study, all parameters will be varied independently from each other in order to get a general view concerning hemodynamic changes induced by stenting. As a consequence, each of the 18 different, virtual patient geometry previously mentioned will be computed four times: once without any stent (abbreviated as WOS in what follows), once with NLP, once with NHP, once with SILK. Finally, 72 computer simulations have been carried out, as summarized in Table 4.1.1. The abbreviations listed in this table will be used when analyzing the results in what follows. For instance Case SP-16-1.4-NLP corresponds to a computation with a straight parent vessel (SP) that has an aneurysm diameter D of 16 mm, and a dome-to-neck ratio D/N of 1.4 stented with a Neuroform3 low porosity stent.

4.1.4 Mesh generation

All geometric models are then imported into a commercial package (ICEM CFD 12, ANSYS) for the generation of high quality body-conforming volumetric grids composed of tetrahedral elements. ICEM CFD meshes the geometry using user-specified parameters. Hence, the complete physical domain is first divided into a number of simply-shaped regions or elements, referred to as individual computational domains, each of those being meshed

Cases considered			
Parent vessel	D (mm)	Dome-to-neck ratio D/N	Stent
Straight (SP), Bent (BP)	$8, 12, 16$	$1.4, 1.6, 1.8$	Without stent (WOS) Neuroform3 low porosity (NLP) Neuroform3 high porosity (NHP) Silk$4,0$ (SILK)

Tab. 4.1.1. Parameters varied systematically during CFD analysis.

independently with tetrahedra elements. The numerical mesh has been systematically refined near all walls, in order to allow proper resolution of the large velocity gradients observed in that region. This is absolutely necessary to obtain a correct estimation of the wall shear stress. A complete mesh refinement study has been carried out for a selected idealized patient geometry and for each stent, in order to check that the flow solution obtained is independent of the employed grid, thus ensuring grid independence. Depending on the geometry considered, about 2.3 million (for NLP/NHP) or 4.5 million (for SILK) of volume grid elements are finally taken into account in the flow simulation. The difference comes from the different thickness of the stent wires that must be resolved by the computational grid. The skewness of all employed grid volumes is always smaller than 0.80.

Note that the quality of the mesh is absolutely essential to obtain quantitative data from CFD, as demonstrated in a companion study [121, 122], in which mesh quality and mesh independence have been examined systematically for real patient geometries. In the present paper, all findings documented in [121, 122] have been fully taken into account, together with standard best practice guidelines for CFD [123].

4.1.5 Governing equations and assumptions

Computational simulations are performed to analyze the intra-aneurysmal flow using an industrial finite volume software (Fluent 12.0, ANSYS Inc, Canonsburg, PA, USA) solving the Navier-Stokes equations in three dimensions. The equations considered in the CFD physically describe conservation of mass and of momentum (see Equations (3.1) and (3.2) on page 45). Since

the flow is considered incompressible and isothermal, a conservation equation for energy is not needed.

As already discussed, 72 CFD simulations will be carried out, each of them involving several million grid points. It is therefore essential to reduce model complexity as much as possible while taking into account all important properties. This leads to the following assumptions:

1. While blood is indeed a complex fluid, in particular regarding thrombus formation, the corresponding deviations from the simple, Newtonian behavior are indeed negligible as long as the flow cross-sections are sufficiently large, as is the case here. As a consequence, blood is considered as a Newtonian fluid with constant dynamic viscosity $\nu = 4\ 10^{-6}$ m^2/s and density $\rho = 1000$ kg/m^3. Many other studies have employed the same Newtonian approximation (e.g., [69, 128, 129]).

2. Only steady-state simulations will be carried out, so that the unsteady term in Eq.(3.2) can be neglected, thus considerably reducing problem complexity. An overwhelming majority of publications dealing with aneurysmal flows employ the same hypothesis. For instance, Steiger et al. [130] observe that the flow solution obtained for a steady flow does not differ noticeably from the systolic field obtained under pulsatile conditions.

3. As a consequence of the previous point, the inflow conditions are considered constant with a parabolic velocity profile associated with a maximum longitudinal velocity (on the centerline) of $u = 1$ m/s. The inflow volumetric flow rate is fixed at 3.75 ml/min.

4. Based on these values, the Reynolds number based on the internal vessel diameter is equal here to 128, proving that the flow is completely laminar and that a turbulence model is not required, in agreement with all published studies concerning this subject. The onset of turbulence is predicted using the Reynolds number Re defined as

$$Re = \frac{\upsilon\delta}{\nu} \tag{4.1}$$

where δ is the characteristic dimension, υ is the local flow velocity, $\nu = \frac{\mu}{\rho}$ is the kinematic viscosity, μ is dynamic viscosity and ρ is fluid density.

5. Finally, all walls are assumed to be rigid. Assessing the risk of rupture certainly requires a good description of material properties, wall deformation and hence very costly coupled fluid-structure simulations, since the walls of aneurysms are weaker and more brittle than arterial walls [131]. This is however not as important when trying to assess hemodynamic modifications induced by stenting, as discussed also for instance by Kim et al. [132]. Furthermore, local material properties are usually unknown for real patient cases.

The reduced numerical model developed in this study has been validated by comparison with Laser Doppler Velocimetry measurements in several phantom models of aortic and cerebral aneurysms, as documented for instance in [133] and in the previous chapter. As a consequence, a good accuracy is expected regarding the hydrodynamic quantities computed in what follows. The numerical simulations have been carried out on the Karman cluster in Magdeburg equipped with 68 dual nodes (2.1GHz AMD Opteron quad processors) using a high-speed Infiniband interconnection. The average computation time for each simulation is around 30 minutes using four computing cores.

4.2 Results

4.2.1 Post-processing CFD data

By comparing the results of the 72 simulations, it is now possible to investigate independently the influence of 1) vessel curvature, 2) aneurysm diameter, 3) dome-to-neck ratio and 4) implant geometry (in particular porosity). For this purpose, the CFD results must be post-processed in an appropriate manner. For each case, the blood flow rate exchanged with the parent vessel through the aneurysm neck and hence the associated residence time, the mean velocity magnitude within the sac and the peak wall shear stress in the aneurysm have been computed in order to quantify the influence of stenting for the different geometries.

It must be kept in mind here that a variety of criteria have been considered in the literature to quantify hemodynamic effects, particularly in association with a prediction of the risk of rupture. For instance, not only the wall shear stress but also its spatial or temporal variation has been presented as the suitable index to predict rupture [37, 38]. There is no real agreement within the research community about the most relevant parameters yet. In what follows, classical hydrodynamic quantities will be computed and combined to get useful data concerning hemodynamic modifications.

Additionally, one specific criterion, the residence time T (in s) is introduced, since it seems particularly suitable to quantify the tendency towards thrombus formation [122, 134]. For this purpose, a control surface is first placed along the aneurysm neck in the simulation, separating the inside of the aneurysm sac from the parent vessel. Then, the volumetric flow rate $\dot{q}_{in}$ (in m^3/s) exchanged between both domains is computed at the end of the CFD simulation, considering only velocity vectors pointing towards the aneurysm lumen (entering flow rate), since the total flow rate is obviously zero for such an incompressible case (the blood quantity entering the aneurysm is the same as that leaving it at each time instant). Knowing this quantity and the total aneurysm volume V, the mean residence time of blood within the sac is computed from:

$$T = \frac{V}{\dot{q}_{in}} \tag{4.1}$$

In what follows, the relative change of T associated with stenting will be used as one major indication of stenting efficiency.

4.2.2 Aneurysmal flow without stenting

As expected, the velocity profile inside the parent vessel upstream of the aneurysm is a simple, parabolic profile corresponding to laminar inflow conditions. Since the emphasis is set on cases with stent, only major results are presented for the basic cases without stenting (WOS).

Sidewall aneurysm on straight parent vessel

As seen from Fig. 4.2.1, in which streamlines colored with the local velocity magnitude and velocity vectors in the neck region are shown, the flow within the aneurysm shows quite smooth conditions. The flow enters the distal portion of the aneurysm neck via a small zone, directed there by the junction of the aneurysm origin and parent vessel wall acting as a natural flow divider. The flow then swirls around the periphery of the aneurysm sac with a slower velocity, in a reverse vortex pattern. Finally, the flow leaves the sac in the proximal and (to a lesser extent) peripheral region around the inflow zone. For this configuration (Case SP-8-1.4-WOS) just 2% of the total incoming blood flow enters the aneurysm and the flow is shear-driven as discussed in [135].

As expected, the pressure varies linearly along the parent vessel. The pressure within the sac (not shown) is almost constant, except for a small pressure rise near the distal neck associated with the flow entering in that

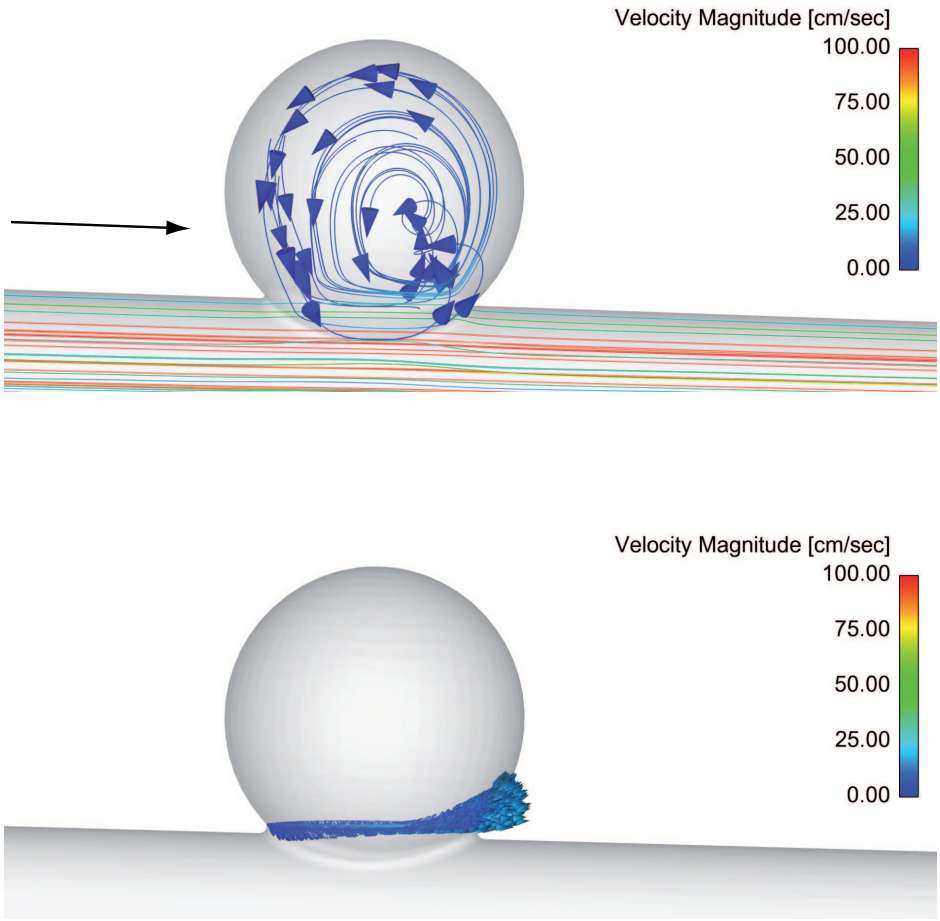

Fig. 4.2.1. Streamlines emitted from inlet and neck, colored with the local velocity magnitude (left) and velocity vectors along the neck region (right), both for Case SP-8-1.4-WOS. In all such figures, the black arrow indicates the flow direction in the parent vessel.

region and changing direction. The wall shear stress (WSS) is constant along the parent vessel upstream of the aneurysm. In the sac, much smaller WSS values are found compared to WSS in the parent vessel (not shown). The maximum WSS is found in the bottom part of the distal neck region, with a maximum value around 19 Pa, almost four times the value observed in the parent vessel just upstream of the aneurysm.

Sidewall aneurysm on bent parent vessel

The spherical aneurysm is directly centered on the bend, as seen in Fig. 4.2.4a, where the obtained streamlines are shown for the case without stenting. Comparing Fig. 4.2.4a with Fig. 4.2.1, considerable hemodynamic modifications appear clearly as a consequence of the difference in geometry. The blood inflow into the aneurysm occurs at a large angle compared to the wall of the aneurysm sac, leading to impingement on the distal aneurysmal wall. As a whole, 17% of the total arterial flow enters the aneurysm through the central and distal neck region. After entering the aneurysm at a relatively low velocity, the flow reverses and accelerates again slightly before exiting the neck partly through the proximal region, partly through the sides, as a consequence of the complex vortical structure observed in Fig. 4.2.4a. These observations are consistent with previous works (e.g., [136]), that also showed a large vortex inside the aneurysm with the flow entering mainly via the distal neck. The maximum WSS is found here at the distal neck region, with a maximum value around 79 Pa, almost 10 times the value observed in the parent vessel just upstream of the aneurysm.

Effect of aneurysm size and dome-to-neck ratio

The observations are qualitatively similar for the straight and the bent parent vessel, so that only the former is discussed in what follows. As the aneurysm size increases for a constant dome-to-neck ratio, the inflow angle into the aneurysm sac remains almost constant. Globally, the velocity fields do not show major structural changes when doubling the aneurysm diameter (figure not shown). The residence time T increases only slightly with increasing diameter for a constant value of D/N.

As visible in Fig. 4.2.2, varying the dome-to-neck ratio for a constant aneurysm size leads to more changes in the velocity field. However, the inflow into the aneurysm stays along the distal neck, with a low velocity. The intra aneurysmal flow in the three aneurysms is still characterized by a single counter rotating vortex that moves slightly towards the distal neck when decreasing D/N. The exchanged flow rate doubles when decreasing the

dome-to-neck ratio from 1.8 to 1.4, amounting to only 1.8% of the incoming blood flow rate for SP-12-1.8-WOS but already to 3.9% for SP-12-1.4-WOS.

4.2.3 Effect of stenting

Now, the hemodynamic changes induced by the three different stent and flow diverter models considered in this study (NLP, NHP, SILK) will be quantified and discussed. Stenting leads to considerable hemodynamic modifications both for the straight and for the bent parent vessel. The resulting changes are more easily seen for the bent parent vessel, which has therefore been chosen in Fig. 4.2.4 . All implants lead in particular to reduced peak velocities (compare Fig. 4.2.3a) to Fig. 4.2.3(b) and Fig. 4.2.4(a,b)). The reverse flow (from left to right) near the aneurysm dome is slowed down, especially with SILK. Before leaving the sac in a direction almost parallel to the upper wall of the parent vessel (and hence to the implant itself), the flow accelerates again slightly. The observed streamlines and peak velocities within the sac are initial indication of a high stenting efficiency, particularly for SILK.

Impact of stenting on average velocity

A first important quantity is the mean velocity magnitude within the aneurysm sac. The obtained values for all cases corresponding to a dome-to-neck ratio of 1.4 are presented in Fig. 4.2.5 for both straight (top) and bent parent vessel (bottom). For the straight vessel (Fig. 4.2.5a), this average velocity (about 1 cm/s) is already two orders of magnitude smaller than the peak velocity in the parent vessel (1 m/s) without any stent (Cases SP-WOS). Stenting systematically leads to a further reduction of the mean velocity magnitude by about one order of magnitude. The resulting mean velocities after stenting are best expressed in mm/s. For the same aneurysm size, the difference between the different models is more pronounced in a small aneurysm (factor 4 between SILK and NHP for 8 mm diameter) than a very large one (factor 2 between SILK and NHP for 16 mm diameter). Furthermore, the reduction in mean velocity is always more pronounced in a small aneurysm (8 mm), with a reduced relative influence of stenting when increasing aneurysm size, which has been systematically observed for all stent and flow diverter models.

Considering now the bent parent vessel (Fig. 4.2.5b), the observed average velocities in the aneurysm without any stent (Cases BP-WOS) are almost 10 times higher than for the straight parent vessel (compare to Fig. 4.2.5a), but still one order of magnitude smaller than the peak velocity in the parent vessel (1 m/s). Stenting systematically leads to a further reduction of the

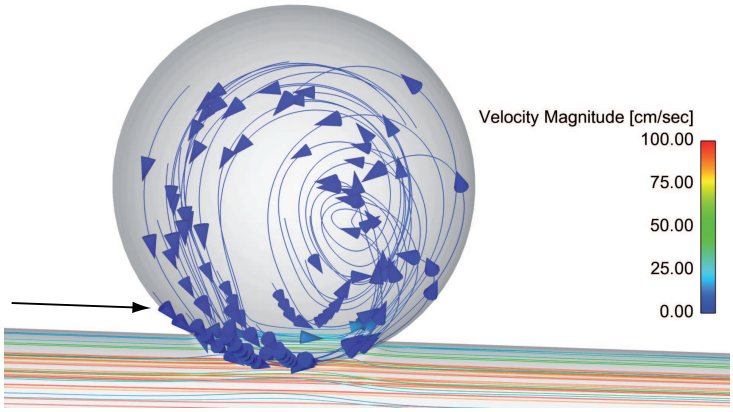

(a)

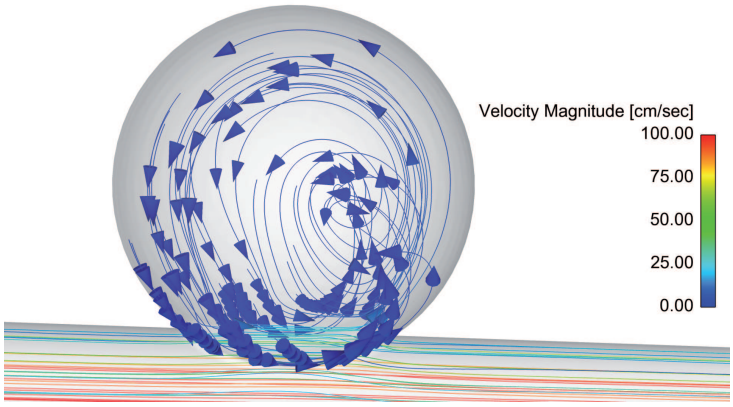

(b)

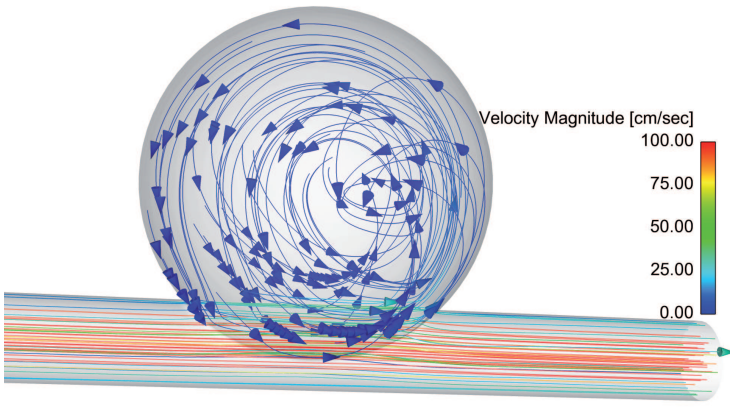

(c)

Fig. 4.2.2. Streamlines emitted from inlet and neck, colored with the local velocity magnitude, showing the influence of a decreasing dome-to-neck-ratio for a constant sac diameter of 12 mm: a) 1.8 (Case SP-12-1.8-WOS), b) 1.6 (Case SP-12-1.6-WOS) and c) 1.4 (Case SP-12-1.4-WOS).

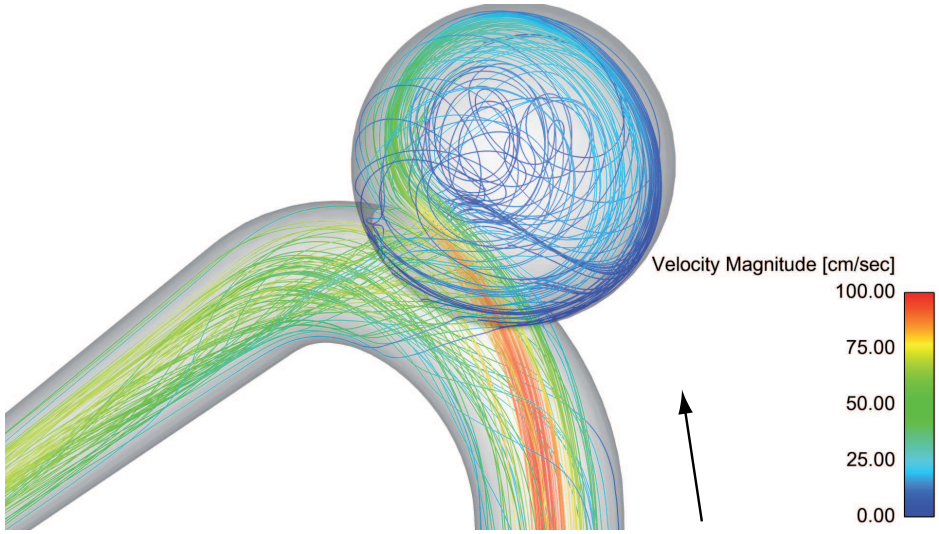

(a) WOS

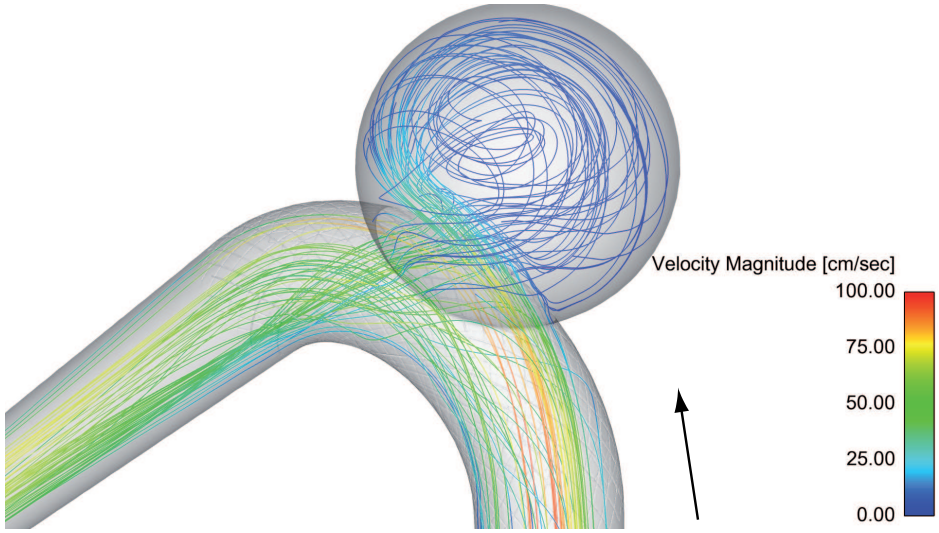

(b) SILK

Fig. 4.2.3. Streamlines emitted from inlet and neck, colored with the local velocity magnitude, plotted for the same vascular geometry and for the three different stent and flow diverter models considered in this study: a) Without stent (Case BP-8-1.4-WOS) b) SILK (Case BP-8-1.4-SILK).

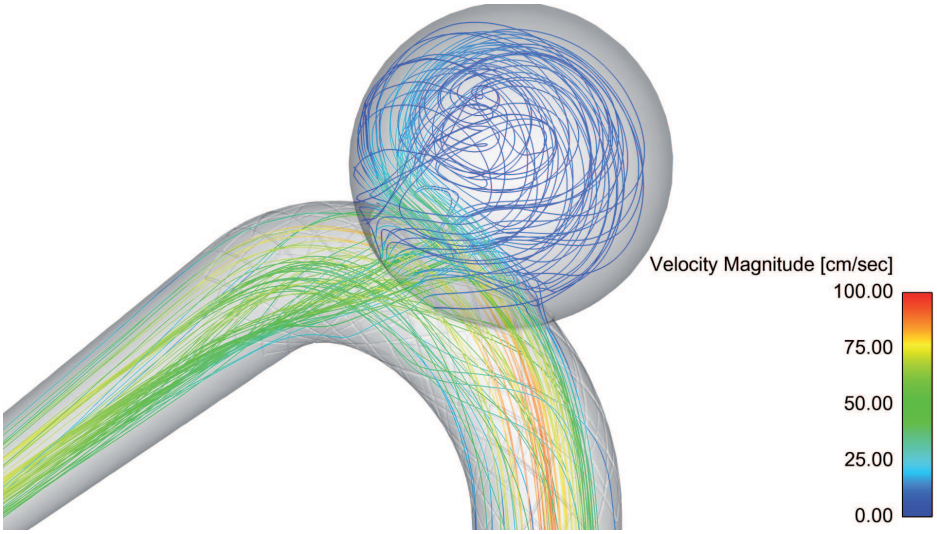

(a) NLP

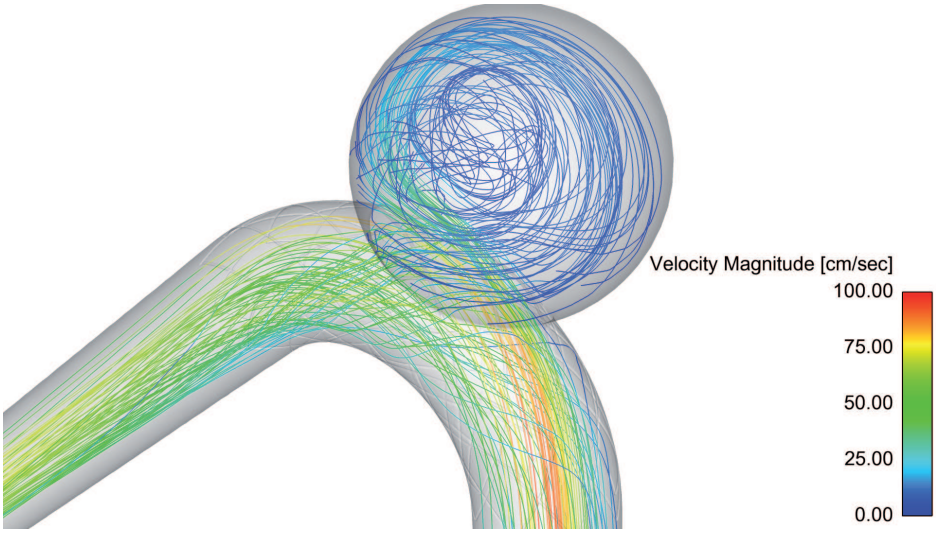

(b) NHP

Fig. 4.2.4. Streamlines emitted from inlet and neck, colored with the local velocity magnitude, plotted for the same vascular geometry and for the three different stent and flow diverter models considered in this study: a) NLP (Case BP-8-1.4-NLP), b) NHP (Case BP-8-1.4-NHP).

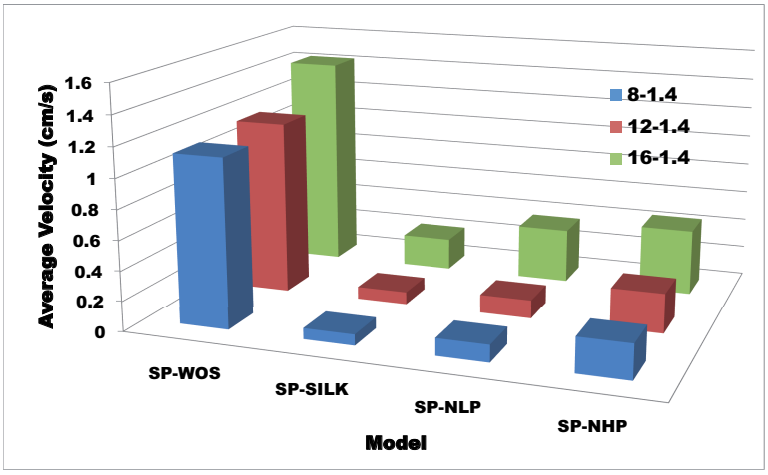

(a)

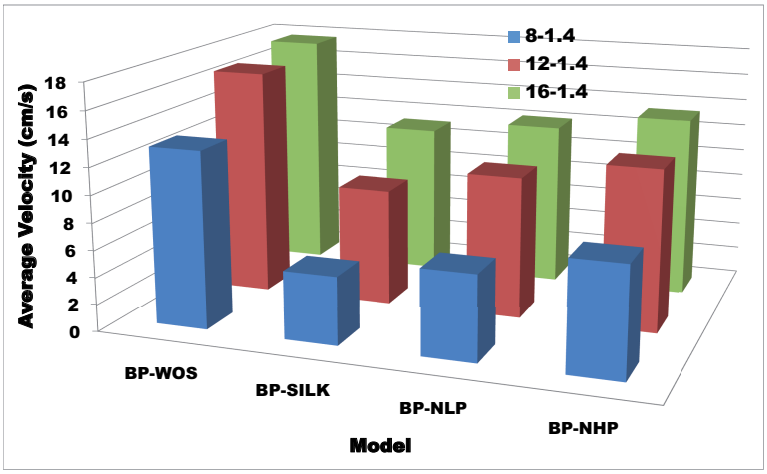

(b)

Fig. 4.2.5. Average velocity magnitude (cm/s) within the aneurysm sac for all cases with a constant dome-to-neck ratio of 1.4 for (a) straight parent vessel; (b) bent parent vessel.

mean velocity magnitude, but only by a factor of about 2 (compared to a factor of about 10 for the straight configuration, SP). In the best case (BP-8-1.4-SILK) the mean velocity is now reduced only by a factor of 3. The resulting mean velocities after stenting are best expressed in cm/s.

Clear trends can be observed for both parent geometries in Fig. 4.2.5. The NHP (83% porosity) systematically leads to the highest value for the mean velocity, while the NLP (67% porosity) is associated with a noticeably lower value. In all considered cases, SILK always leads to the lowest mean velocity. Considering mean velocity as the main parameter, stenting efficiency would therefore be SILK > NLP > NHP.

Impact of stenting on peak wall shear stress

In the non-stented cases WSS is higher near the distal part of the aneurysm sac compared to the proximal part of the aneurysm. In what follows, only the peak WSS in the sac is considered to compare stenting efficiency.

Globally, the findings apparent in Fig. 4.2.6a for the straight parent vessel show trends similar to that already discussed concerning the mean velocity (see again Fig. 4.2.5a). In all cases, stenting leads to a reduction of peak WSS within the aneurysm sac. SILK always leads to the lowest WSS value, followed by NLP and finally NHP. For a constant dome-to-neck ratio, increasing sac diameter is always associated with a higher WSS, both with and without stenting. As already discussed previously, the effect of stenting in terms of WSS reduction is noticeably smaller for the larger aneurysm (look in particular at Cases SP-16-1.4 in Fig. 4.2.6a). Conversely, for a constant aneurysm diameter, the WSS values are systematically reduced when increasing the dome-to-neck ratio for stented aneurysms, while it stays almost unchanged or even increases without stenting (compare for instance SP-16-1.4-WOS with SP-16-1.8-WOS). Concerning WSS reduction, the effect of stenting appears to be considerably reduced for a smaller dome-to-neck ratio.

For the bent parent vessel as well, the findings apparent in Fig.4.2.6b show trends similar to that discussed in association with the mean velocity. In all cases, stenting leads to a reduction of peak WSS within the aneurysm sac, and this reduction is even more pronounced compared to the straight parent vessel (compare to Fig. 4.2.6a), starting however from higher values in non-stented cases. Typically, WSS evolve between 10 Pa (WOS) and 2-8 Pa (with stents) in the straight case, while values of 30 Pa (WOS) reduced to 5-20 Pa with stenting are found in the bent vessel. Hence, WSS reduction is more pronounced but still at a considerably higher level than for the straight vessel configuration. In the best case (Case BP-8-1.4-SILK), the maximum WSS decreases by a factor of 4. In all cases, SILK always leads to the lowest WSS

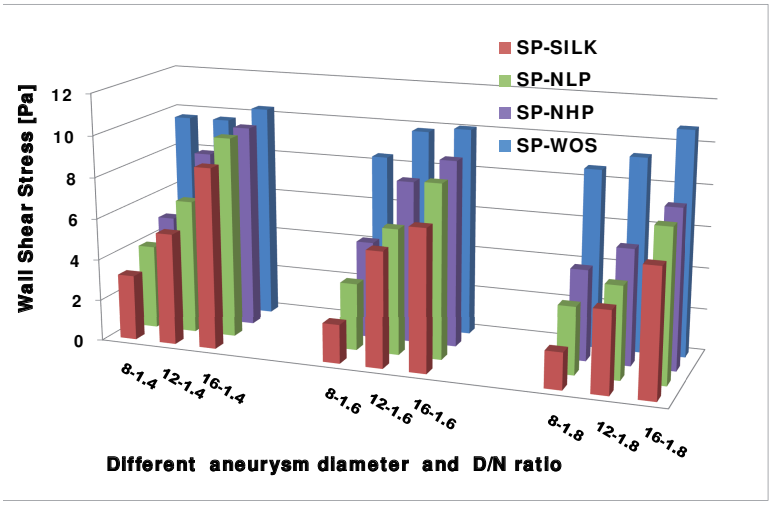

(a)

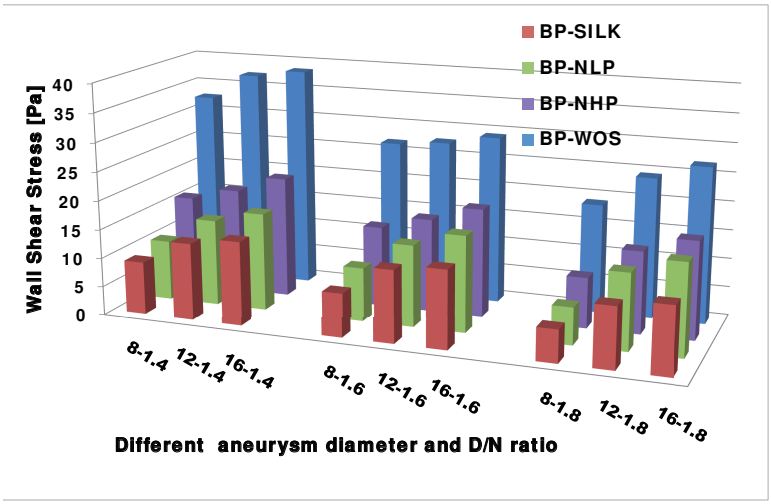

(b)

Fig. 4.2.6. Peak wall shear stress within the aneurysm sac for all cases (a) straight parent vessel; (b) bent parent vessel.

value, followed by NLP and finally NHP. For a constant dome-to-neck ratio, increasing sac diameter is always associated with a higher WSS, both with and without stenting. As already observed previously, the effect of stenting in terms of WSS reduction is slightly smaller for larger aneurysms. Conversely, for a constant aneurysm diameter, the WSS values are systematically reduced when increasing the dome-to-neck ratio for aneurysms without stents. The same is also true for stented aneurysms but is only really noticeable for small diameters.

Impact of stenting on residence time

From the point of view of stenting efficiency for a straight parent vessel, Fig. 4.2.7a perhaps depicts the most interesting indicator, since it shows the relative increase (in %) of blood residence time T within the aneurysm sac for SILK, compared to the case without stenting (WOS). This quantity allows a global analysis of hemodynamic changes, in particular with a view toward thrombus formation in the sac. Similar results (comparison not shown) have of course been computed for NLP and NHP. The findings visible in Fig. 4.2.7a confirm previous observations. First, stenting indeed leads to a considerable increase of residence time within the aneurysm sac (180% in the best configuration, Case SP-8-1.4-SILK). In all considered cases, SILK leads to the largest increase in residence time (comparison not shown). Furthermore, stenting efficiency considering T as reference quantity is better for a smaller aneurysm diameter.

All these observations are qualitatively confirmed for the bent parent vessel, but Fig. 4.2.7b nevertheless shows noticeable quantitative differences. Stenting leads again to a considerable increase of residence time within the aneurysm sac, the maximum value (250% for Case BP-8-1.4-SILK) being even much larger than for the straight geometry (180%, for the same Case). SILK always leads to the largest increase in residence time (comparison not shown) and stenting efficiency is again better for a smaller aneurysm diameter. For the bent vessel, the influence of the dome-to-neck ratio is clear. For small diameters, increasing the dome-to-neck ratio leads to a considerable decrease of changes in T and hence to a lower stenting efficiency. This is not much visible for the larger diameter (16 mm), since the stenting efficiency is globally smaller in this configuration.

4.3 Discussion

Techniques for the endovascular treatment of intracerebral aneurysms have advanced significantly in the last few years. This treatment is increasingly

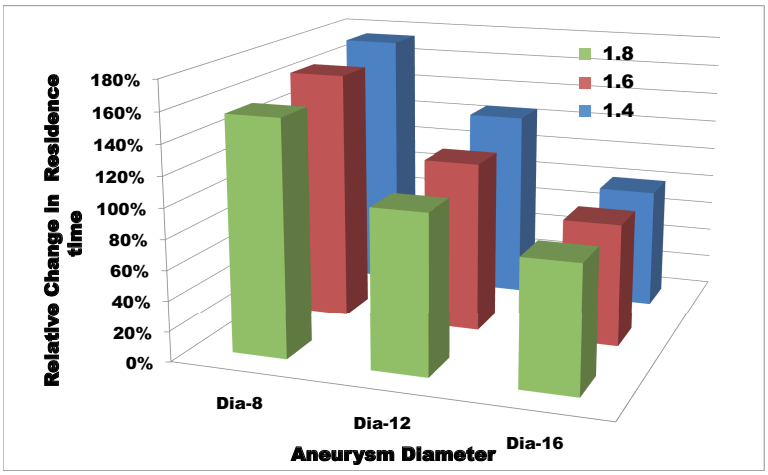

(a) Straight parent vessel

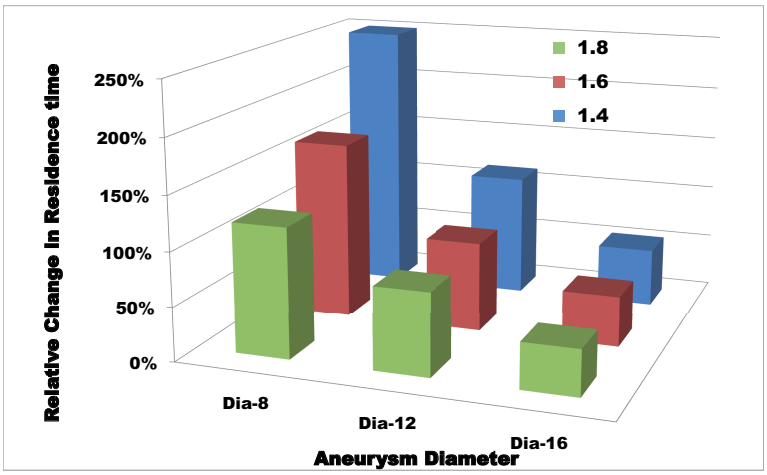

(b) Bent parent vessel

Fig. 4.2.7. Relative increase (in %) of blood residence time T within the aneurysm sac for a SILK flow diverter compared to the case without stenting (WOS) for (a) straight parent vessel; (b) bent parent vessel.

performed by endovascular means, but wide-necked aneurysms continue to present a technical challenge. Endovascular coiling is associated with several hazards (coil protrusion into the parent vessel, subtotal aneurysm occlusion, recanalization of the aneurysm); intravascular stenting would therefore be an attractive alternative if its efficiency would prove sufficient. In order to develop optimal flow diverters for treating cerebral aneurysms, a detailed knowledge of the associated hemodynamic changes is needed.

Currently, the decision for a treatment is based on an individual risk assessment which includes factors such as the condition of a patient and main characteristics of the aneurysm like location, size and shape. None of the available treatment options can be really deemed satisfactory yet.

While stents were originally only used as a complement to endovascular coiling, various earlier studies have demonstrated that such stents could sometimes be considered as a valid standalone treatment. This finding has been verified by in vivo and in vitro investigations, as well as numerous numerical studies. All these works indicate that some stents are indeed able to either reduce the intraaneurysmal flow and/or to permanently occlude the aneurysms (see for earlier publications on this subject [84, 90, 136, 137, 138, 139, 140]). Complementary studies demonstrate that implant geometry (wire diameter and porosity), mechanical and material properties (alloy, surface charge, surface tension), and finally biocompatibility are most important for immediate and long-term successful results [141, 142] when using stents as standalone treatment. Among those properties, the porosity of the implant is of key importance for hemodynamic modifications since it controls resistance to blood flow through the inter-wire gaps and the associated pressure difference, thereby allowing the possibility of flow stasis in the pouch, hence promoting rapid thrombosis. In the late 2000s, new stents became available: the so-called "flow diverting" stents. These models are now at the forefront of standalone endovascular neurosurgery.

Recently, Cebral et al. [125] have investigated the flow changes induced by the implantation of a stent using an adaptive embedding technique for a lateral aneurysm model on a straight vessel and for a personalized curved vessel reconstructed from medical images. Kim et al. [132] have demonstrated that the placement of multiple stents on a patient-specific aneurysm considerably modifies the hemodynamic parameters. They found out that the influence of the stent design on aneurysm hemodynamics is significant in the double-stented aneurysms but less so in single- and triple-stented aneurysm models. Depending on the quality of the stent deployment, the impact of stenting on aneurysm hemodynamics varied substantially. Meng et al. [135] have used a commercial simulation code (STAR-CD) to study hemodynamic implications of stent placement in a model canine venous pouch on a straight

vessel and in a model rabbit spherical pouch on a curved vessel considering steady-state flow conditions. Their numerical results and dye flow visualizations indicate viscous shear-driven flow and inertia-driven flow in straight- and curved-vessel aneurysm models, respectively.

Apart from a few in vitro quantitative investigations (e.g., [59]), many in vivo studies have been conducted on cerebral aneurysms so as to determine the critical size, since it is the primary parameter currently used to determine whether an aneurysm is likely to rupture or not. Even if the critical size at which an aneurysm becomes hazardous cannot be determined exactly, studies by Kassel and Torner [143] showed that for large aneurysms (> 10 mm), treatment is required since the risk of rupture is high. Another study by Weir [144] demonstrated, however, that for aneurysms smaller than 4 mm, size alone would suggest that all of these lesions are safe and unlikely to rupture following [143]. In reality, some of these small lesions do rupture while larger aneurysms remain stable, hence implying that additional predictors are needed. As a consequence, it is of interest to consider aneurysm hemodynamics for a variety of sizes. Thus, in the present study, aneurysms with a diameter between 8 and 16 mm are analyzed.

In spite of all published studies and due to the highly complex, coupled phenomena controlling aneurysm thrombosis, many issues are still unclear concerning the optimal hemodynamic modifications that could be induced by a stent. A better understanding of this aspect would open the possibility for a dedicated optimization of the geometrical properties of an implant.

For this purpose, different hydrodynamic quantities have been computed and analyzed in the present study (mean velocity in the aneurysm, peak wall shear stress in the sac, residence time within the aneurysm). Important observations can be drawn from combining these quantities for a variety of configurations (three different aneurysm diameters, three different dome-to-neck ratios, two different parent vessel geometries - straight or bent -, three different implants), but are obtained obviously with a high computational burden (72 different CFD computations).

It is well-known from previous studies that the real geometry of the vascular system is of fundamental importance to quantify stenting efficiency. In an effort to reduce complexity while keeping key properties into account, two different idealized vessel geometries have been retained. Finally, a spherical aneurysm placed either on a straight vessel or at the bend of a curved vessel has been retained. Computational results confirm large quantitative differences between both cases. However, the qualitative findings are mostly identical, so that the conclusions drawn from the analysis should have a high level of generality.

The first few computations consider the aneurysm model without stent.

For the straight parent vessel, it is observed that a large aneurysm size and a large dome-to-neck ratio lead to lower hydrodynamic load, long residence time and hence should favor intra-aneurysmal thrombosis. Changing now to a curved vessel, a drastic change in blood flow dynamics is observed within the aneurysm, with an average velocity about 10 times higher in the sac. The maximum value of WSS (in the distal neck region) is almost 10 times higher than along the parent vessel.

Building on top of these first results, three different implants (Neuroform3 with either high or low porosity, Silk4, 0) have been numerically introduced into the vessel at the level of the aneurysm. The most significant finding is a systematic reduction of flow activity inside the aneurysmal pouch after stenting, particularly for stents with a lower porosity and for flow divertors, as documented by all hydrodynamic indicators. The mean velocity in the aneurysm as well as the peak shear stress in the sac is always lower after stenting. At the same time, the blood residence time within the aneurysm is increased by up to 250% depending on the conditions, leading to more stagnant conditions that could facilitate thrombus formation. The presence of the implant partially uncouples the aneurysmal flow from that of the parent vessel and hence reduces momentum and mass exchange between the two. However, large quantitative differences are observed. Stent porosity and geometry play a major role for hydrodynamic changes. Summarizing the conclusions obtained from the analysis of the 72 simulations, the following observations can be made:

- Silk4, 0 always leads to the largest hemodynamic modification, independent of the considered criterion and geometry.
- The observed differences in efficiency among the different stent and flow diverter models are noticeably greater for a small aneurysm than for a large one.
- Stenting is systematically more efficient for the smallest aneurysm diameter (8 mm), with a decreasing impact as the size goes up to 12 or 16 mm.
- The influence of the dome-to-neck ratio on the findings is not completely clear and differs between stented and non-stented aneurysms. Without a stent, a large dome-to-neck ratio is favorable to reduce hydrodynamic load. For stented aneurysms, the same appears to be true when considering wall shear stress. However, the (advantageous) increase in blood residence time is higher for a low dome-to-neck ratio, which would conversely indicate a higher efficiency of stenting for such conditions.

Optimization of the wire network geometry with a view towards suitably tailored hydrodynamics around the neck region is now attempted. Similar studies involving realistic flows in real patient geometries [121] must also be pursued in order to fully check the generality of our findings, as explained in the next chapter. Finally, developing accurate blood clotting models including suitable non-Newtonian properties will be necessary for a full understanding of thrombus formation in the aneurysm. Further issues associated with implant flexibility leading to an easy endovascular delivery and implantation into the tortuous cerebrovascular system will also play an important role for practice.

5. VIRTUAL STENTING ON REAL PATIENT GEOMETRY

Part of this chapter has been submitted as journal article to Journal of Biomechanics.

In recent years, intracranial stenting has been proven to be an effective support tool in the endovascular treatment of ruptured and unruptured cerebral aneurysms. Up to recently, the interventional approach was mostly confined to coiling alone. With the additional use of stents, a substantial number of aneurysms are now suitable for endovascular treatment, where surgical clipping was the only option in the past. This includes broad-necked aneurysms and cases in which the aneurysm neck incorporates important vessels without collateral flow. It was soon noticed that intracranial stents might considerably reduce the flow entering the aneurysm sack. Even complete thrombosis has been observed. This fact consequently led to the development of so-called "flow diverters", stents with a higher mesh density. With such devices, flow alteration is more effective and complete occlusion of aneurysms occurs more frequently as compared to conventional stent designs. In addition, no coiling is required. Leaving the vulnerable aneurysm sack itself outside the treatment strategy reduces complications associated with the coiling procedure. Nevertheless, the treatment with flow diverters is still associated with known problems. As opposed to stents with conventional design, branching vessels should not be covered with this device. Otherwise, blood flow in these branches would be critically reduced with infarction in the dependent territory as a consequence. Another drawback is at present the restriction to vessels with a sufficient diameter, for example the internal carotid artery. Furthermore, time to thrombosis seems to take up to several months, which is not sufficient in an emergency situation, i.e., for acutely ruptured aneurysms with a high risk of early rerupture in the absence of an efficient treatment. Thus, stents need to be developed that rapidly modify hemodynamics in a very circumscribed segment of the vessel (near the aneurysm ostium), while leaving the flow unchanged proximally and distally to the aneurysm and in nearby branching arteries. If available, such devices would yield a further decline of complication rates and an improvement of treatment success. An accurate simulation of hemodynamics in the patient's geometry is required to choose and possibly develop the most appropriate stent designs. Simultaneously, it

would guide deployment strategies in order to improve aneurysm occlusion and to avoid complications. Note that, for the sake of brevity, generic issues associated with flow simulations of cerebral aneurysms are not discussed in the present chapter. The interested reader is referred to the recent review of Sforza et al. and to chapter 2 for corresponding information [145]. Stuhne and Steinman [146] performed a mesh convergence analysis with a varying node spacing near the stent to come up with a mesh resolution requirement to run flow simulations with stents. However, simulating blood-flow past endovascular devices such as stents in patient-specific models poses a number of challenges [147, 148, 81]. These include techniques for virtual deployment of stents, meshing the vascular model and the deployed stent, developing appropriate pre- and post-stenting boundary conditions, and handling of relatively large computational meshes. The numerical flow simulation provides various hemodynamic quantities. After a first qualitative examination relying on contour or vector plots of the velocity field, the modification of key hemodynamic parameters is analyzed quantitatively in what follows. For the sake of completeness, not only the commonly investigated wall shear stress has been studied in detail, since it is still unclear how this parameter may correlate with the risk of rupture. As an important additional quantity, the inflow rate at the aneurysm neck and the stasis in the aneurysm have been investigated, since they should allow a measure of thrombotic conditions. The flow stasis has been computed through the turnover time, as it has been done in [134] and in the previous chapter for idealized and patient-specific geometries. A successful stenting treatment should change the hemodynamics in the aneurysm and produce thrombogenic conditions, i.e., reduce the flow velocity and elongate the stasis. To stimulate the aneurysmal thrombosis, the increase of the stasis in the aneurysm should be specifically targeted [98]. Previous studies [98, 149, 24] have shown that increasing aneurysmal flow turnover time supports thrombus formation in cerebral aneurysms. Considering all these results, the turnover time is thus used as a major indicator of stasis [106] in the present chapter.

In order to check all these issues, well-documented, generic patient geometries with a cerebral aneurysm are needed. Considering that it is better if such geometries are available for the whole research community, it was decided to rely on the geometries of the Virtual Intracranial Stenting Challenge (VISC) 2009 for the present study. The central objective of VISC [150] is to assess the ability of engineering teams with expertise in computational hemodynamics in providing clinical partners with valuable pre-treatment information within the time constraints of an elective endovascular intervention. Under the auspices of the International Intracranial Stent Meeting 2009 (http://www.ics09.org/), the 3rd Virtual Intracranial Stenting Chal-

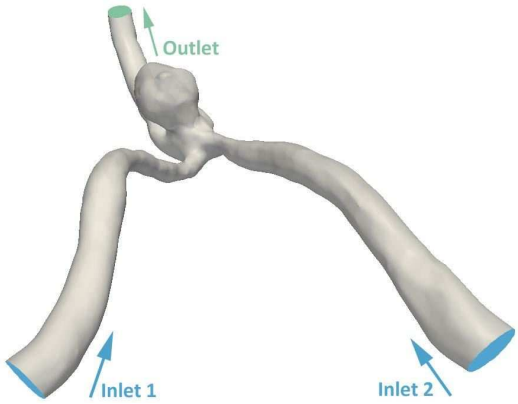

Fig. 5.0.1. Original flow configuration of the first case provided for the VISC09 challenge [122].

lenge (VISC09) has been announced in Sendai, Japan. The research team MOBESTAN (a German abbreviation standing for Modeling and Control of the Flow Behavior in Aneurysms) at the University of Magdeburg "Otto von Guericke" in Germany has been selected as one of the few contributors to this challenge. The patient data and the stent data have been provided by the organizers and employed to perform 3D vascular geometry reconstruction, virtual stent deployment and hemodynamic simulations using the given flow and stent information. The organizers of VISC09 have provided two different cases (i.e., patient data). In what follows, the first case has been retained throughout and will be used to illustrate all solution steps and encountered difficulties when virtually stenting a real patient geometry [122].

5.1 Computational geometry and mesh

The considered computational geometry is shown in Figure 5.0.1 before stent deployment. As explained previously, the corresponding dataset has been obtained from the reconstruction of a real patient data provided by the organizers of VISC09.

5.1.1 Computational geometry

The dataset has been saved as an STL-mesh, a standard commonly used to store the reconstructed geometry in image-based intracranial simulations. STL stands for stereolithography and is also often used for rapid prototyping. This format employs a set of unstructured triangles to describe the surface of a given volume. The stent geometry has been deployed manually on a

trial and error basis after deforming the vessel geometry. The straight stent geometry prescribed by the VISC09 organizers has first been reproduced. In order to deploy the stent in the patient-specific geometry, the stent had to be scaled, bent, rotated and moved in the desired position. Figure 5.1.1 shows the modified patient geometry obtained after deploying the stent (red wireframe) compared to the original configuration (opaque), as discussed in following section.

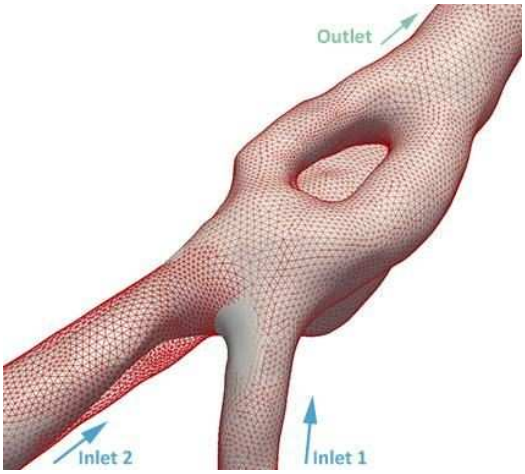

Fig. 5.1.1. Bottom view of the deformed patient geometry (red wireframe) over the original geometry (opaque) from Fig. 5.0.1 after stent deployment. Surface optimization (as described in Section 5.1.2) has already been performed.

5.1.2 Modification of the provided geometry

The provided surface geometry and stent are first modified during two preprocessing tasks: 1. Improvement of surface mesh quality; 2. Geometry deformation associated with stent deployment.

Improving surface mesh quality

All the provided geometries exhibit insufficient quality for a highly accurate CFD simulation. The meshes suffer locally from strong scalene triangle shapes (e.g., acute-angled triangles) as illustrated in Figure 5.1.2. The mesh quality has been improved by systematically remeshing the surface using an advancing front mesh generator [151]. It employs a two-step approach to recreate the mesh. As an initial step, special points and edges are defined as invariable positions to steer the advancing front. For the considered appli-

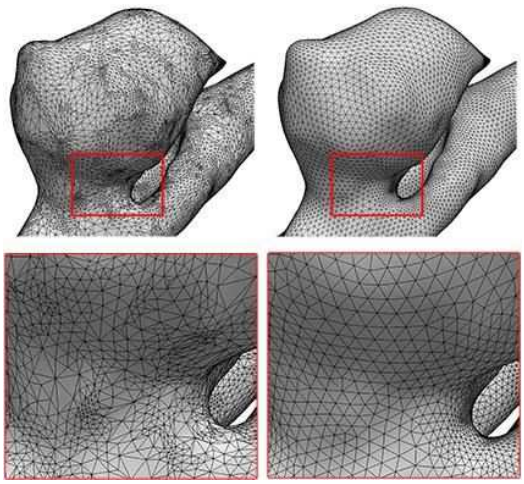

Fig. 5.1.2. (a) Original, insufficient mesh quality due to scalene triangle shapes, (b) Improved mesh quality after adaptive re-meshing

cation it is particularly important to preserve the feature edges at the inlet and outlets, as shown in Figure 5.1.3.

Therefore, these edges are marked as fixed boundaries for the advancing front approach, based on their feature angle. This feature angle is used to specify where surfaces will be broken by curves and vertices representing the maximum angle between mesh edges and faces at which geometric features will be defined [152]. The threshold for the selection must be selected appropriately to avoid an inclusion of sharp surface features, which would lead to an unwanted increase of the required mesh resolution. Surface features with a higher feature angle than the orthogonally cut in- and outlets are most likely the result of reconstruction artifacts. They can be smoothed locally (e.g., with a Laplacian) to avoid their inclusion as boundary edges for the advancing front approach. The size of the resulting mesh triangles depends on the local surface curvature (Figure 5.1.4) and is adapted locally, delivering a good surface mesh with nearly equilateral triangles.

Nevertheless, mesh quality can be improved further, as done in a second step. A point-wise relaxation Broyden-Fletcher-Goldfarb-Shanno (BFGS) of an angle/area-based error functional is employed to move the points towards the center of gravity defined by their neighbors. Topological changes such as edge swaps and point collapses are finally used. As a result, an excellent surface mesh quality is obtained, which is an absolute pre-requisite for a good volumetric mesh [153].

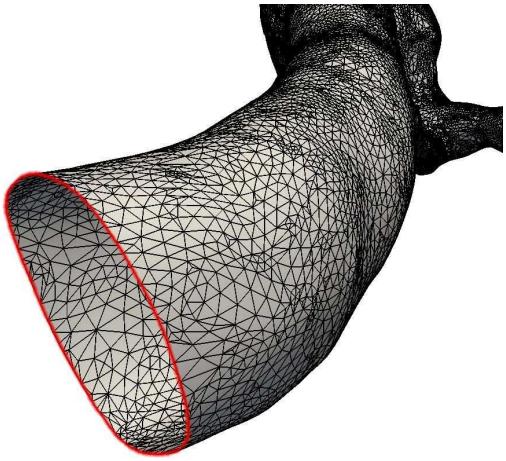

Fig. 5.1.3. Selection of the outlet (red) and inlet boundaries to mark their edges as feature edges

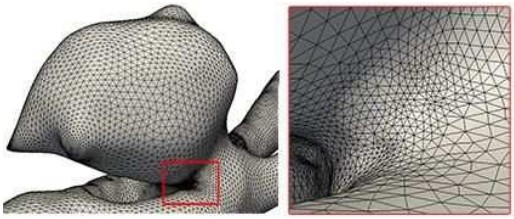

Fig. 5.1.4. Detail view on a high curvature region efficiently discretized with small triangle shapes

Reconstruction of the Stent

The stent geometry specified by the organizers of VISC09 representing a commercial Silk 4,0 flow diverter (Balt Extrusion, Paris, France) exhibited some inconsistencies regarding normal vector directions and vertex ordering. Therefore, the obtained mesh was not directly suitable for the application of the advancing front approach. Remeshing would have been of course possible. However, the stent graft is based on recurring patterns that can be easily parameterized, avoiding a computationally expensive full remeshing. Instead, a reconstruction of the given stent geometry has been carried out using Computer Aided Design (CAD), allowing direct control over mesh quality, granularity and feature edge handling.

Geometry and Mesh Deformation

Many published studies consider rigid walls during stent deployment. However, medical doctors often observe vessel expansions of up to 30% under real conditions, depending on patient-specific properties and geometry. In the present project, the involved clinical partners guided stent placement for a maximal therapeutic benefit based on their experience. Within the targeted area, the stent is initially aligned along the centerline of the vessel, computed using the polygonal model rather than the underlying image data. Thus, the accuracy of the resulting centerline depends on the local mesh resolution rather than on the image resolution (a meaningless quantity for the final CFD). The embedded Voronoi diagram is used to calculate the centerline [154]. This is the discrete solution for the continuous problem of finding the locus of centers of all maximum-inscribing spheres. This type of centerline calculation leads to a very natural centerline pathway, even in pathological areas where the vessel differs from a tube-like morphology. The stent is then placed and aligned along the centerline computed in this way. In stenotic areas near the ostium of the aneurysm, the stent leads to a dilatation of the vessel. The necessary deformation was prescribed manually in several iterations, steered by the experience of the clinical partners. This manual, expert-supported approach appears to be necessary in the absence of any information concerning wall thickness and local wall properties, hindering a physically-based computation of the deformation. Obviously, the resulting geometry is partly heuristic, which is always the case when exact material properties are now known (this is in practice the rule and not the exception). The retained procedure has the advantage of building on top of practical experience based on hundreds of corresponding interventions by medical specialists. Figure 5.1.5 illustrates the resulting deformation of pa-

tient geometry and stent. The finally retained stent pathway (black line with arrow in Fig. 5.1.5) leads from the inlet to one of the outlets. A local dilatation is applied to the stenotic area (dashed black circle in Fig. 5.1.5) of the inflow vessel ahead of the aneurysm. A distance-based weighting for each vertex displacement (color-coded with red to blue in Fig. 5.1.6) has been applied, the weights being distributed according to a Gaussian function.

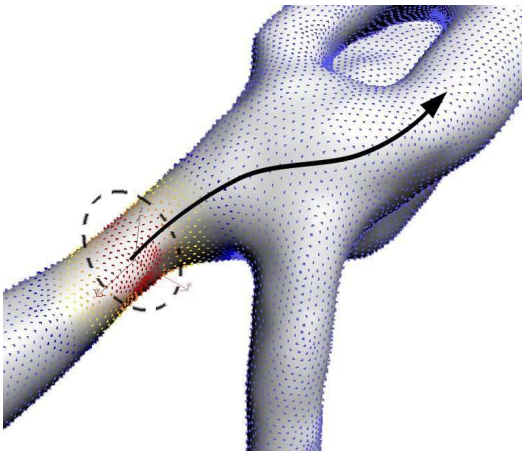

Fig. 5.1.5. Illustration of the final stent course (black) and main deformation region (dashed black circle), combined with an elastic, distance-based shape deformation of the vessel wall (red=100%, blue=0%)

5.1.3 Numerical Mesh

Figure 5.1.6 depicts the final configuration after stent deployment. The high-quality surface mesh obtained thanks to the previously described procedure can now be directly used for generating the volume mesh required for CFD.

The resulting volume mesh quality has been quantified based on the equi-angle as well as on the equi-volume skewness, two standard criteria for CFD [123]. A volume mesh has always a much lower quality compared with the quality of the associated surface mesh. Therefore, the excellent quality of the surface mesh is a crucial step of the mesh generation, since the quality of the final volume mesh highly influences the numerical results, as shown in what follows. An insufficient mesh quality may lead to convergence problems or - even worse - to a completely wrong solution.

Part of the obtained volume mesh is shown in a cut through the aneurysm sac in Fig 5.1.7. The region with a strongly refined mesh corresponds to a cut through the stent

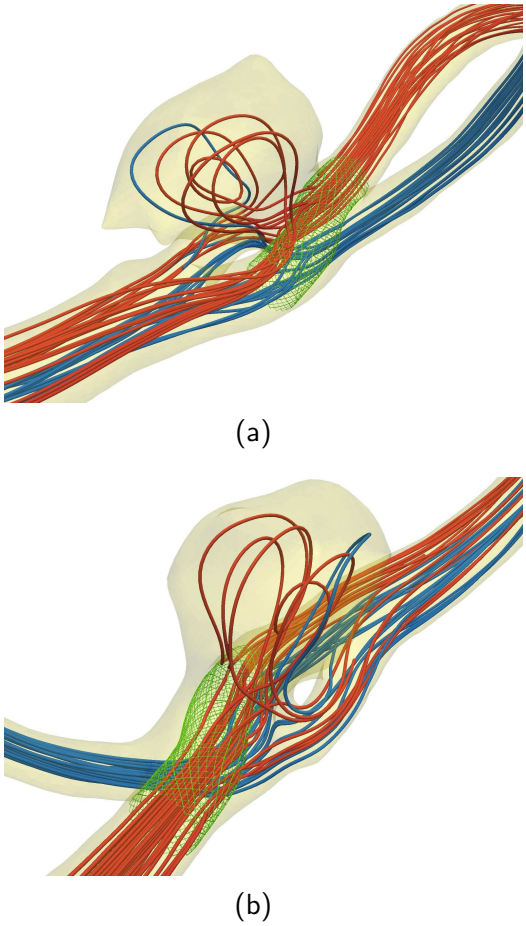

Fig. 5.1.6. Virtual stent (green wireframe) in the patient geometry after deformation, together with selected streamlines (red from Inlet 1, blue from Inlet 2) in the stented geometry for Case 5M-p3 (see later Table 1 for the definition of all Cases)

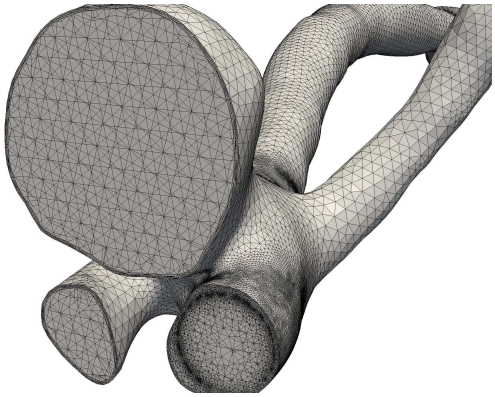

Fig. 5.1.7. Part of the obtained volume mesh shown in a cut through the aneurysm sac. The region with a strongly refined mesh corresponds to a cut through the stent.

The easiest and in practice widely used mesh for such a complex geometry is a pure tetrahedron mesh. Many automatic meshing tools are available to create such an unstructured mesh. If this volume mesh is sufficiently fine, it may indeed accurately predict the fluid flow. However, a previous study of the authors has shown that the wall shear stress distribution cannot be predicted accurately in this manner even using a very fine and well-resolved mesh [155]. An additional, fine prism mesh is absolutely required near the wall as commonly used in, e.g., external aerodynamics. This drawback of the pure tetrahedron mesh has also been reported in other numerical simulations of intracranial aneurysms [156].

As a consequence, one- and three-layer-prism meshes have been built along the walls, leading to an average elevation from the first mesh element to the wall around 20 μm. Obtaining such a fine resolution is hardly possible using only tetrahedron cells without an excessive skewness quality problem. On the other hand, the core region of the domain can be indeed meshed by tetrahedron, finite volume cells. The virtually stented configuration has been finally discretized with a total number of 4,590,290 cells for Case 5M-p3 (see later Table 5.2.1). Figure 5.1.7 shows a cut through the aneurysm sac, where the finer mesh indicates the stent location.

5.2 Computational hemodynamics

Blood rheology is represented using a Newtonian description with constant density and viscosity, where the blood density is chosen as 1000 kg/m^3 and the dynamic viscosity as 4×10^{-3} Pa s [150, 157]. Previous studies have

demonstrated that using a more realistic, non-Newtonian fluid model should not be necessary for the conditions considered in the present configuration [42], since it involves only large vessels ($\geq$ 0.5 mm) and comparatively low shear rates. However, this might not be true in general and appropriate rheological models will be certainly needed.

5.2.1 Inlet boundary condition

At the inlet of the computational domain the inlet velocity is usually given as a Dirichlet boundary condition (prescribed values). Corresponding velocity values can be measured, e.g., by Doppler ultrasound or phase-contrast magnetic resonance angiography. For most published numerical studies this information was not directly accessible. Therefore, only estimations based on integrated quantities or on the literature are employed, often combined with the assumption of a constant, uniform velocity profile. This very simple situation might however lead to misleading interpretations. For instance, the computed wall shear stress values in the vicinity of the inlet are completely meaningless, since a uniform velocity profile leads theoretically to an infinite, local wall shear stress (or, in practical CFD, to extremely large values).

In order to overcome this issue, the inlet cross-section is extracted from the considered computational domain and a separate channel flow is simulated in a pre-processing step. Only a short channel is considered and meshed, but the two ends of this section are connected using a periodic boundary condition, modeling an infinite channel flow with a uniform cross-section and a prescribed mass flow rate. Obviously, the position of this inlet should be chosen in a suitable way, sufficiently far from any strong bend. At the end of the pre-processing step, a fully developed velocity distribution is obtained and implemented as fixed boundary condition for the further CFD of the flow in the patient geometry, eliminating the problem mentioned previously.

In the present case a steady flow condition is finally retained with an inlet flow rate of 2.36 10^{-6} m^3/s at each inlet, as prescribed by the organizers of VISC09. Due to the different cross-sections, this leads to mean velocity values of 0.2045 m/s and 0.1102 m/s at the first and second inlet, respectively. The Reynolds number at the outlet of the considered geometry is 470 based on the mean velocity and hydraulic diameter, proving that the flow is laminar and eliminating the need for any turbulence model. All vascular walls are assumed to be rigid, as done in most published studies (see [145] and cited references in this review), since real wall material properties are completely unknown and highly patient-dependent. A standard, no-slip boundary condition is employed at all contact points with surfaces (vessels, stent).

5.2.2 Outlet boundary condition

At the outlet, either resistance or traction-free boundary conditions are usually applied. The resistance model is described by $p = Rq$, where R denotes the resistance and q the mass flux. A vascular bed model can be used to evaluate the resistance R [158]. The traction-free condition prescribes directly the pressure at the outlet. In this study only one outlet is considered. Hence, both boundary conditions deliver the same results for a steady flow. As a consequence, the outlet boundary condition has been simply chosen as a prescribed, uniform relative pressure of 0 Pa.

5.2.3 Computational details

All simulations have been carried out on the Kármán Linux cluster in Magdeburg equipped with 68 dual nodes (2.1GHz AMD Opteron 64-bit quad processors) using a high-speed Infiniband interconnection. The numerical computations are performed in parallel using up to five computing cores applying the commercial CFD solver ANSYS-Fluent 6.3. As explained previously, the mesh quality is essential for accurate results. Getting correct predictions is of course a key requirement if the results should be used to guide treatment options considered by the medical doctors. As a consequence, several different meshes have been compared in this work as described in Table 5.2.1, containing also the number of prism layers along the artery wall (figure following letter p in the Case name). The figure preceding M in the Case name gives roughly the number of computational cells, expressed in millions. The first case correspond to the patient geometry without stenting, all other cases contain the stent placed as described previously. The employed body-conform grids involve roughly between 1 and 7 million finite volume cells. Larger meshes cannot be considered on a single processor PC due to the corresponding memory requirements. For instance, the mesh with 7 million elements requires a total amount of 10 GB of memory applying a double-precision solver on a 64-bit system. The computation with this particular mesh is realized within less than 7 hours wall-clock-time using second- order discretization reaching normalized residuals of 10^{-8} using 8 computing cores in parallel. The influence of several numerical parameters has been checked :

1. Single-precision vs. double-precision computations: Case 5M-p3 has been computed with both a single as well as a double precision solver, on either a 32 bit and a 64 bit system, yielding four results. Surprisingly, all the relevant variables are within 1% of each other. As a consequence, single-precision simulations are recommended, since they are considerably faster.

2. All computations have been performed applying either first or second-order accurate numerical discretization schemes. It has been observed, that the peak velocity value within the aneurysm sac might show more than 15% relative difference between a first-order and a second-order computation, all other parameters and grid being identical. Therefore, second-order computations are highly recommended when a corresponding accuracy is required.

3. Different residual reduction values have been also prescribed to detect convergence. From this analysis, it can be stated that the default settings of commercial CFD solver are usually not a sufficient constraint. Following our present experience, residual reduction should be at least a factor 10^5 for the mass conservation equation (continuity). This is normally enough to ensure simultaneously convergence for all other flow quantities.

Then, the mesh dependence of the numerical results has been carefully checked when including the stent. The first mesh with less than 1 million finite volume cells (Case 0.5M) is not included in the further analysis, because it was impossible to obtain a converged flow solution. This is not a real surprise, but a direct consequence of an inappropriate mesh quality (second row in Table 5.2.1). In one previous study the effect of the numerical mesh has been examined comparing the wall-shear stress distribution [155], choosing the finest mesh (however, without prism layer) as a reference grid. In the present case, this finest mesh involves almost 7 million finite volume cells (last row in Table 5.2.1). The computation with a second-order upwind discretization scheme performed for Case 7M-p3 is again retained here as a reference solution and all the other numerical simulations are compared with this result. Two different tetrahedron meshes have been investigated for 2 million cells. The uniform type (Case 2M-tetra-uniform) is uniform throughout the cross-section, while the non-uniform mesh is refined close to the wall, leading on the other hand to relatively large volume elements in the core region.

5.3 Results and discussion

The computational results are exemplified in Figures 5.3.1 and 5.3.2. In Figure 5.3.2 selected streamlines are presented, demonstrating the reduction of the flow entering the aneurysm sac. A quantitative analysis is now essential in order to accurately quantify the impact of stent deployment. Unfortunately, no general agreement can be found in the literature concerning the

Tab. 5.2.1. Number of finite volume cells and mesh quality considered in the computations

Case	Number of cells	Prism layers on the wall	Maximum equi-volume skewness	Maximum equi-angle skewness
No stent	4 360 896	0	0.8	0.819
0.5M	535 325	0	0.998	0.991
2M-p1	1 983 938	1	0.918	0.862
2M-tetra-uniform	1 726 582	0	0.933	0.892
2M-tetra-non-uniform	1 667 001	0	0.9	0.902
5M-p3	4 590 290	3	0.905	0.914
5M-tetra	4 785 186	0	0.934	0.904
7M-tetra	6 985 877	0	0.836	0.875
7M-p3	6 939 966	3	0.853	0.853

most relevant criterion for cerebral aneurysms. Geometric properties have been extensively analyzed, e.g., in [159, 160]. The hemodynamic characterization was the subject of the work published by Burleson and Turitto [161], considering in particular hemodynamic shear stress and residence time of the blood within the aneurismal sac. Both morphological and hemodynamic parameters were investigated in [162] for more than 100 cases. Several authors stated that excessive wall shear stress might cause rupture, while others consider that low values are dangerous and should be eliminated. Considering that the emphasis is placed here more on the computational procedure, only the peak wall shear-stress (WSS) values are listed in Table 5.3.1. Indeed, the employed computational meshes lead to considerable variations of this property. Moreover, the flow stasis within the aneurysm has been computed from the residence time [134, 163] and is shown as well in Table 5.3.1. This residence time is simply determined by dividing the full aneurysm volume by the inlet volume flow rate found at the aneurysm neck, defined as a straight plane placed slightly above the stent (Figure 5.3.2a). The aneurysmal inflow rate is obtained by integrating the entering flow rate over the full cross section. To check mass conservation, the outflow rate has also been determined along the same plane and is indeed found equal to the inflow rate, as expected. Finally, the maximum and the mean values of the velocity magnitude within the aneurysm sac (Figure 5.3.2b) have been listed in Table 5.3.2. Table 5.3.1 illustrates the computed residence times and the peak wall shear stress in the aneurysm sac after deploying the stent. All numerical grids with less than 3 million cells under predict the turnover time by more than 10%, except when a suitable local refinement is employed. The cases 5M-p3 and 5M-tetra are in good agreement with the reference result, with less than 5% difference. On the other hand, only the meshes with prism layers are able to determine the wall shear stress values with an accuracy comparable to that of the very fine, reference mesh with a pure tetra grid. The cases 2M-p1 and 5M-p3 shown an error in peak WSS below 5% compared with the reference solution. On the other hand, the computations with coarser tetra meshes without prism layer overpredict significantly the maximum wall shear-stress values. Combining both criteria, only the case 5M-p3 appears able to predict both key quantities with a precision level comparable to the reference mesh but at a considerably reduced computational cost. From the point of view of stenting efficiency, the inflow rate exchanged between the main vessel and the aneurysm is reduced to 60% of its original value after stenting, leading to a corresponding increase of the residence time by the same factor. The hemodynamic alteration is hence successful in the present case when applying the chosen stent-design in the manner described previously (Figure 5.3.2b). A similar modification (reduction by about a factor 2) is observed for the

Tab. 5.3.1. Quantitative comparison of inflow rate, residence time, and maximum wall shear stress in the aneurysm sac for all meshes

Case	Inflow rate $[cm^3/s]$	Residence time [s]	Relative difference compared to 7M-p3	Maximum WSS [Pa]	Relative difference compared to 7M-p3
No stent	0.4456	0.646	-37.94%	6.507	-24.02%
0.5M	-	-	-	-	-
2M-p1	0.3043	0.944	-9.32%	9.205	7.48%
2M-tetra uniform	0.3124	0.919	-11.72%	11.486	34.12%
2M-tetra-non-uniform	0.2751	1.046	0.48%	13.525	57.93%
5M-p3	0.2766	1.037	-0.38%	8.755	2.23%
5M-tetra	0.2845	1.008	-3.17%	9.797	14.40%
7M-tetra	0.2716	1.058	1.63%	8.928	4.25%
7M-p3	0.2758	1.041	Ref	8.564	Ref

average and maximum velocity within the aneurysm sac (Table 5.3.1).

It is now possible to summarize the main findings of the present study as follows:

1. The importance of an accurate reconstruction of the patient geometry is obvious in order to obtain results useful to decide further specific treatment options.

2. The quality of the geometric reconstruction directly conditions the quality of the surface grid and will hence strongly impact the quality of the volume grid. Since this parameter controls in turn the key hemodynamic parameters, the pre-processing steps (geometric reconstruction, generation of a surface grid) must be carried out with great care.

3. As long as vessel and aneurysm vessel properties cannot be measured locally and in a patient-specific manner with an acceptable accuracy, it seems as well to assume rigid walls in the simulation.

4. Single-precision vs. double-precision computations: no significant difference has been observed. Therefore, single-precision simulations are

Tab. 5.3.2. Quantitative comparison of average and peak velocity magnitude in the aneurysm sac for all meshes

Case	Average velocity magnitude $[cm/s]$	Relative difference compared to 7M-p3	Peak velocity magnitude $[cm/s]$	Relative difference compared to 7M-p3
No stent	3.4	88.89%	37.37	80.53%
0.5M	-	-	-	-
2M-p1	1.605	-10.83%	20.07	-3.04%
2M-tetra uniform	1.82	1.11%	16.76	-19.03%
2M-tetra-non-uniform	1.605	-10.83%	16.26	-21.45%
5M-p3	1.722	-4.33%	19.43	-6.14%
5M-tetra	1.666	-7.44%	18.49	-10.68%
7M-tetra	1.696	-5.78%	20.16	-2.61%
7M-p3	1.8	Ref	20.7	Ref

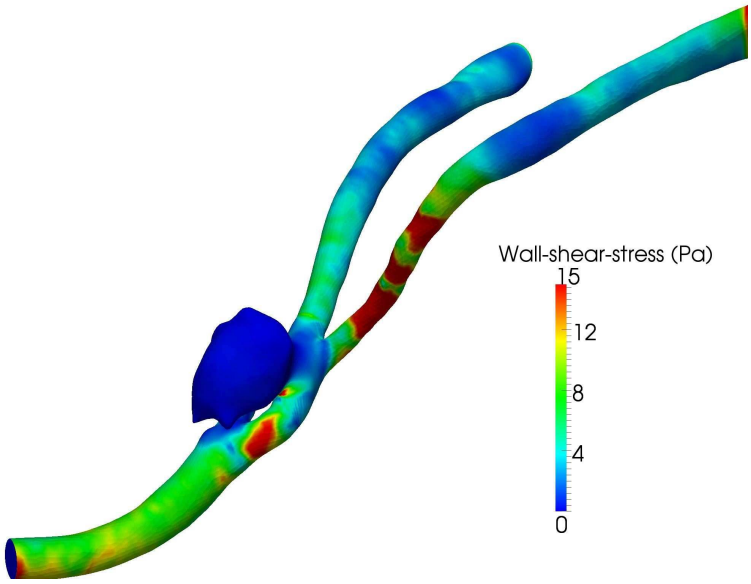

(a)

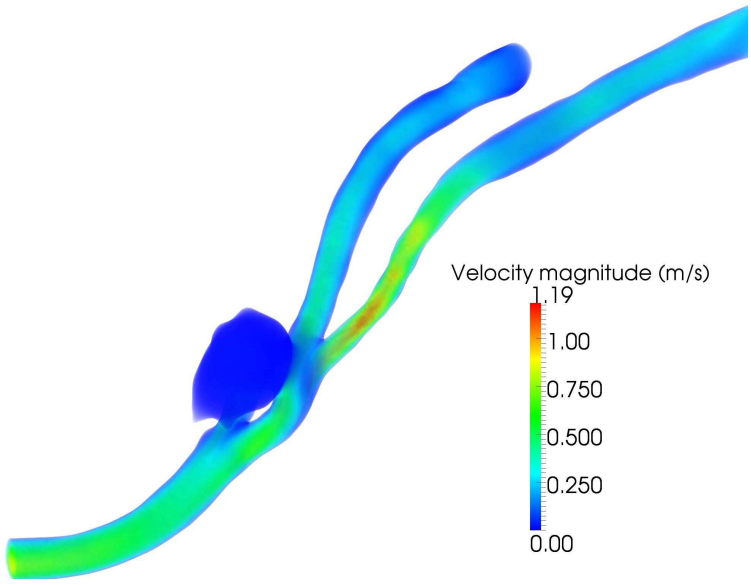

(b)

Fig. 5.3.1. (a) Computed wall shear-stress distribution and (b) Volume rendering of the velocity magnitude, both for Case 7M-p3

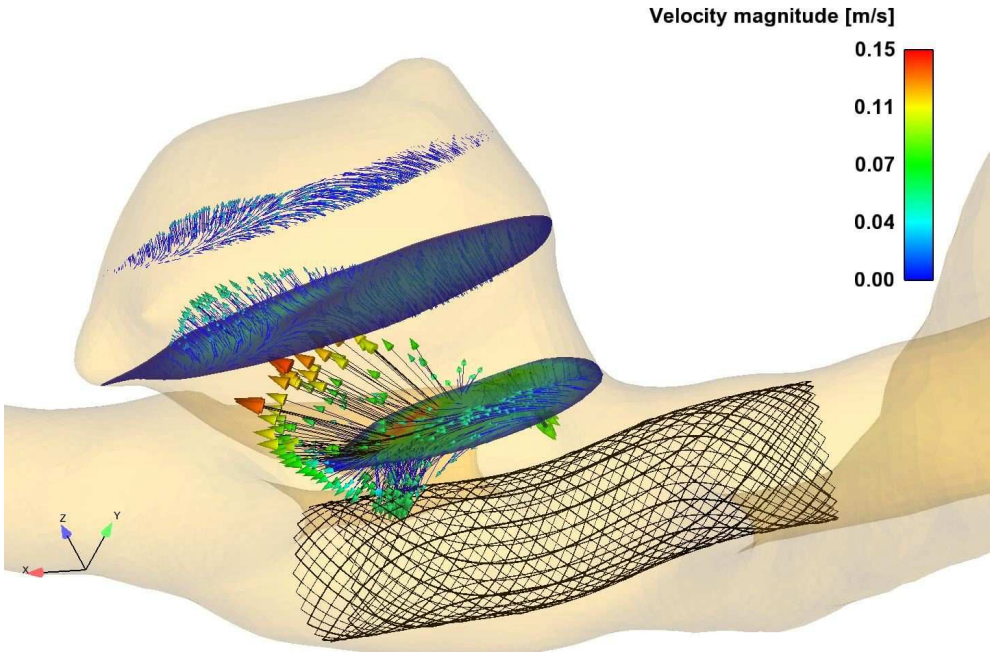

(a)

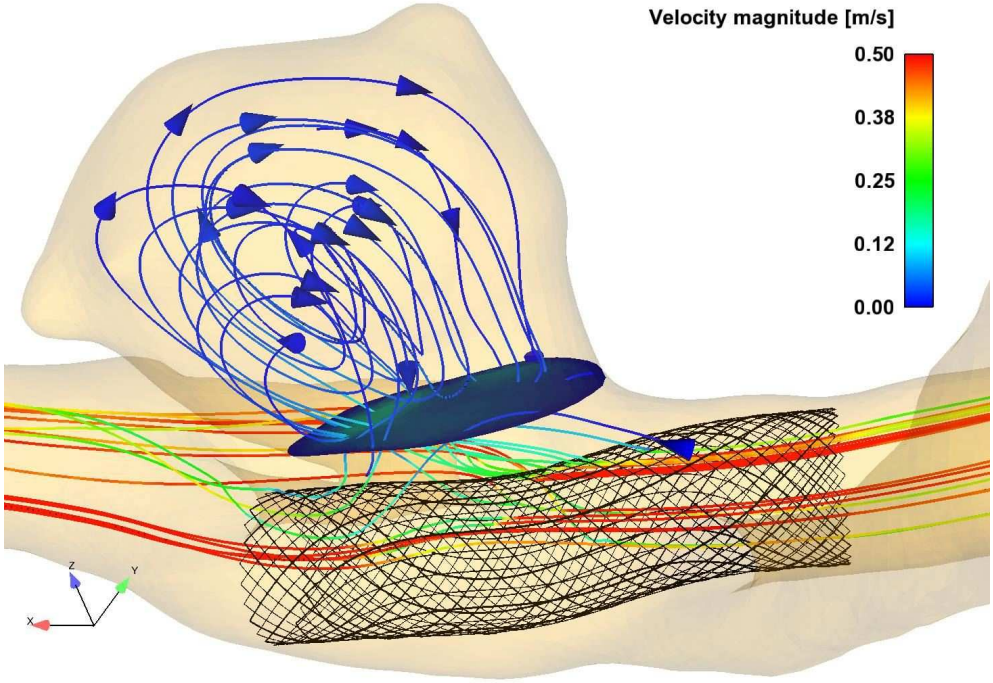

(b)

Fig. 5.3.2. (a) Computed velocity vectors in the aneurysm and (b) Selected streamlines for Case 5M-p3, colored by local velocity magnitude

recommended, being faster.

5. First-order vs. second-order discretization: considerable differences are observed and a second-order discretization is recommended, in particular for relatively coarse meshes. The difference is reduced for very fine grids [164].

6. Residual values for the convergence: tests reveal that a residual reduction by a factor of 10^{-5} is needed (and sufficient) to avoid a noticeable impact of this value on the results.

7. Retaining simultaneously the residence time, the peak velocity and the peak WSS in the aneurysm sac as key hemodynamic quantities, a relatively coarse computational mesh (2M-p1, coarsest acceptable grid resolution) can still be used to predict all resulting flow conditions with an accuracy better than 20%. When an accuracy better than 10% is needed, 5 million volume elements should be used. At least a few prism layers are absolutely necessary if wall shear-stress must be accurately predicted, but are superfluous for the other listed quantities.

Note that some remaining issues cannot be tested in the present configuration. For the considered case, prescribing suitable inflow and outflow boundary conditions is relatively straightforward, as described previously. The issue becomes much more complex when several outflows are taken into account simultaneously. Only steady-state computations have been presented, as prescribed by the organizers of VISC09. Even if many publications tend to show that unsteady simulations do not lead to very different results, this might not apply when discussing relative differences as low as 10%. Hence, further unsteady simulations have been carried out and used to validate the procedure as described in [163] and in Chapter 3. Considering blood as a simple Newtonian fluid should be applicable for the present geometry but might certainly be unsuitable for other geometries involving much smaller vessels or when trying to simulate the progress of thrombosis.

5.4 Conclusions

In this chapter, the impact of the computational settings on the CFD results has been investigated considering a stented aneurysm within a real patient data. Geometry deformation has been applied in order to deploy the stent in a realistic manner. The quality of the surface mesh has been first improved in order to produce finally high-quality volume meshes, as required for computations that should ultimately support medical treatment options.

All steady-state simulations have been performed using the commercial flow solver ANSYS-Fluent. The computational results have been compared before and after deploying the virtual stent. Both qualitative and quantitative analyses have been employed to predict the effect of the virtual stent deployment and the influence of the mesh and of all numerical parameters. It has been found that the stent deployment increases the residence time in the aneurysm by a factor of almost two. It is believed that this modification should facilitate thrombus formation. A sufficiently fine mesh is necessary to resolve the stent and to get accurate CFD estimations, depending on the acceptable error level. Finally, guidelines have been proposed concerning CFD for virtual stenting applications, covering a variety of issues from surface mesh to boundary conditions and from second-order discretization to residual values at convergence.

6. SOME OPEN ISSUES

6.1 Newtonian vs. Non-Newtonian fluid model

Understanding of blood flow dynamics is very important for biomedical applications. Blood is a suspension of blood cells and platelets in plasma. The cells suspended in blood are not righid spheres, and the volume fraction of erythrocytes is about 40 to 45%. Therefore, one should accept that the real behaviour of blood is non-Newtonian. But it has been shown that blood is Newtonian at all rates of shear for hematocrits up to 12%. When the shear rates are sufficiently high (>100 s^{-1}), blood can be treated as a Newtonian fluid, which seems to be a reasonable assumption in large arterial flow simulations.

A few studies [113, 165] showed that there is no significant difference between the simulation results obtained through Newtonian and non-Newtonian blood flow models. In a Newtonian fluid, the relationship between the shear rate γ and the shear stress σ is linear:

$$\sigma = \mu\gamma \tag{6.1}$$

where the dynamic viscosity μ does not depend on the shear rate. The non-Newtonian behaviour of blood is due to the proteins in the plasma, and the elasticity and aggregation of the red cells. This non-Newtonian behaviour is more evident when the shear rate is small, such as it occurs in arterioles and capillaries [166]. The viscosity is affected by these properties and, in general, increases with shear rate (see [167] for the description of some blood flow models).

Several studies have been conducted to investigate the effects of shear thinning by considering different fluid models. Cebral et al. [20] demonstrated that the overall flow pattern characteristics and distribution of mean WSS of aneurysms were relatively unaffected by the use of the non-Newtonian Casson model. Valencia et al. [53] studied the non-Newtonian effect on two virtual saccular aneurysm models with different inclination angles and one healthy model of the basilar artery. They found that the effect of geometry (in this case represented by different aneurysm inclination angle) had a stronger effect

on the relative magnitude of the flow-induced stresses than the assumption of blood as a non-Newtonian fluid.

However, it is important to note that the above studies either did not perform quantitative comparison of the results from different fluid models or did not examine realistic, non-spherical aneurysm shapes, especially those sidewall aneurysms like in our study where the fluid dynamics are much more complex and blood rheology tends to be more non-Newtonian.

Our own results indicate that the Newtonian fluid assumption in general is acceptable in CFD modeling of healthy vessels and "well-behaved "aneurysms that do not harbor regions of significant low-shear flows as discussed in chapter 5. However, the current data suggest that the non-Newtonian blood properties should be considered when simulating the flow in aneurysms with slow and recirculating flow regions (low-shear flow), which are sometimes found in aneurysms with very complex geometry. The Newtonian model cannot capture the increased viscosity in low-shear region and consequently overestimates the shear rate and WSS. When the non-Newtonian effects are disregarded for such aneurysms, the shear rate and WSS appear falsely higher in the low-shear regions, thereby under-representing the risk of clot formation and aneurysm growth and rupture.

Therefore, it is suggested that researchers conducting CFD simulations of blood flow either adopt non-Newtonian models from the beginning, or identify low shear regions in an initial run using the Newtonian assumption, and then validate the results using a more accurate non-Newtonian model.

While non-Newtonian constitutive models thus supply important information for blood flow simulations, one needs to be aware that their use adds additional uncertainties. There are many non-Newtonian models to choose from, and additional variations arise from their experimentally determined modeling parameters. Thus, it is very difficult to determine the best non-Newtonian model to use.

For example, consider our virtual aneurysm study as discussed in Chapter 4 (Fig. 6.1.1). BP-8-1.4-SILK yielded the highest turnover time and has been retained for a comparison to understand the effect of different blood flow models.

The different non-Newtonian models considered are the Power law model, the Herschel-Bulkley model and the Carreau model.

The Power law model is also known as the Ostwald-De Waele model. It can be used to model pseudoplastic fluids. The shear stress is written as a power of shear rate.

$$\mu = \mu_0 \times (\dot{\gamma})^n \tag{6.2}$$

where $\mu_0 = 0.0046$ cP and $n = 0.027$ is the power law index value used for the simulation, as taken from the literature.

The Herschel-Bulkley (H-B) fluid model of blood assumes that the viscosity varies according to the law :

$$\mu = k(\dot{\gamma})^{n-1} + \frac{\tau_0}{\dot{\gamma}} \tag{6.3}$$

Recommended experimental values for blood are: $k = 8.9721$ cP.s^{n-1}, $n = 0.8601$, and $\tau_0 = 17.5$ mPa [55].

The equation and the values for the Carreau model have been already mentioned in Chapter 3.

All simulations were carried under the same conditions as in Chapter 4. Power law model and Casson model predicted lower average WSS compared to a Newtonian flow, but yielded different values. The Herschel-Bulkley model predicted higher average WSS compared to all the other models. The Power law model predicted 69%, Carreau model 91% and the H-B model 115% of the average the average WSS from the Newtonian case. Moreover, the Power-law gave 8%, the Carreau model 65% and H-B 85% of the average velocity of the Newtonian case (Fig. 6.1.2).

However these considerable differences do not hold for the unsteady simulations considered for a realistic geometry in chapter 3, where the difference

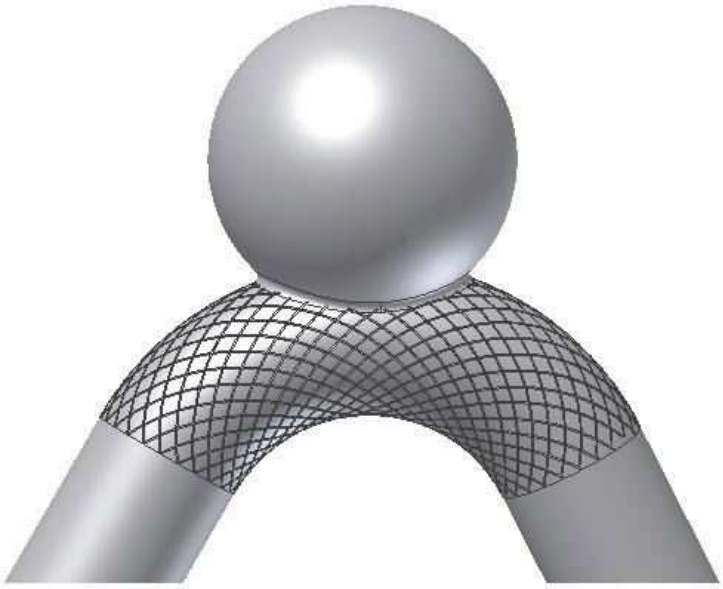

Fig. 6.1.1. Sidewall aneurysm model with curved parent vessel (inner bend angle of 60°).

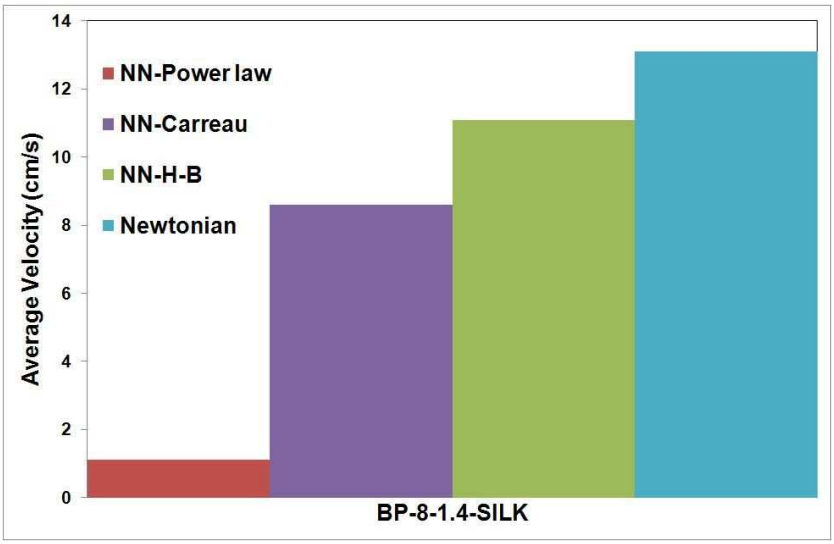

Fig. 6.1.2. Effects of different blood flow model on BP-8-1.4-SILK

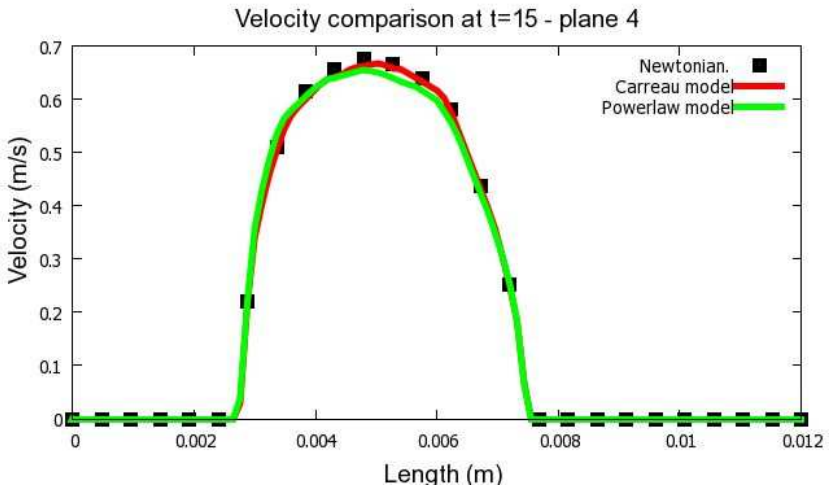

Fig. 6.1.3. Effects of different blood flow model on cerebral aneurysm phantom model in cross section of plane 4 at peak systole.

between the Newtonian and all non-Newtonian models were less than 10 % for velocity values, as seen in Fig. 6.1.3. It is therefore completely unclear yet, how relevant this issue might be.

Another problem associated with non-Newtonian models is the fact that the H-B model has no lower limit for viscosity at very high shear (where the viscosity tends to zero). This unrealistic behavior may unduly influence the flow field. Therefore, in the future, more investigations should be dedicated to produce consistent shear thinning model and care should be taken to accurately determine experimentally suitable non-Newtonian model parameters.

6.2 Fluid-structure interaction

Fluid-structure interaction has been an important field of study for many years. It is a technique used in numerical problems to provide an understanding of the impact of the flow on structures, both within and surrounding the flow. Due to the drastic increase in computing power over the last decade, numerical methods are becoming increasingly effective. This has resulted in the increased utilization and research in the field of numerical methods to predict FSI motions and other responses. Originally, this method was used to simulate cases of aeroelasticity for aerodynamic research, but recently it has been actively integrated in various biomechanical researches, including those involving blood flows through aneurysms arteries [168, 169, 170]. FSI analysis of cerebral arteries is not so common because the cerebral arteries deform less and are smaller than other arteries and consequently have lower influence. However, no matter how small, these small deformations may affect and interact with the dynamics of blood flow in the brain and this makes the arterial wall deformations in cerebral arteries important.

One such effort has been sucessfully carried out in our group using a virtual aneurysm geometry and a patient specific geometry (Fig. 6.2.1). The considered idealized side wall aneurysm model has a diameter of 3.6 mm for the pipe and 8 mm diameter for the aneurysm. A thickness of 0.3 mm was considered to represent the vascular lumen (inner layer of blood vessel) for both geometries. The software ANSYS 12 was used for the simulation of fluid-structure interaction between the wall and the lumen.

The governing equations for the fluid domain are the continuity and Navier-Stokes equations with the assumptions of homogenous, incompressible, and Newtonian flow. Since the fluid domain is deformable in an FSI problem, an Arbitrary Lagrangian-Eulerian (ALE) formulation has been adopted. The ALE formulation introduces a moving coordinate system to model the deformation of the fluid domain.

(a) Idealized sidewall aneurysm geometry

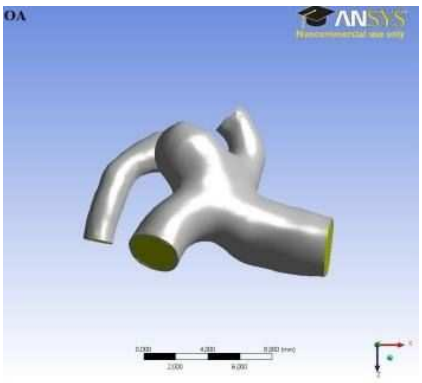

(b) Patient specific aneurysm geometry

Fig. 6.2.1. Two different geometries considered for the FSI study [171]

As boundary conditions, a simple sinus waveform is defined at the inlet. This simplification is justified because the main focus of the investigation lies on the deformation of the cerebral vessel wall. Thus, for the inlet boundary condition, a time-dependent flow rate V_{puls} is defined by

$$V_{puls} = 0.8 + 0.5.\sin(2\pi t + \frac{3}{2}\pi) \tag{6.1}$$

For the outflow of the fluid a time-independent "Pressure outlet" is used. For this purpose, an average relative static pressure P_{spec} is computed by

$$P_{spec} = \frac{1}{A}\int_s P_{ip} dA \tag{6.2}$$

where P_{ip} is the static pressure at each integration point on the surface of the outflow. On the structural side, the annular space around the entrance and exit surfaces of the flow are firmly fixed, so there is no shift there. This ensures that the flow reaching the entrance surface is always perpendicular to the fluid domain. The vessel wall is assumed to be an isotropic, linear, elastic solid with Young modulus of elasticity $E = 1$ MPa and Poisson ratio $\nu = 0.45$. At the FSI interface the fluid obeys no-slip condition. Crucial in influencing the convergence behavior of the simulation, is an additional source term with respect to its continuity. This source term shows that the mass flow through the fluid-structure interface is zero, so there will be no mass exchange between the fluid and structure. The Reynolds number varies between 246 and 1066 for the considered geometries.

Tab. 6.2.1. Number of finite volume cells considered in the computations

	Fluid	Solid
Idealized geometry - Mesh1	91211	26888
Idealized geometry - Mesh2	104237	41813
Patient specific geomtry - Mesh 1	84672	20719
Patient specific geomtry - Mesh 2	106887	29476

Mesh generation is done using commercial mesh generation tool ANSYS workbench. Mesh sensitivity study was carried out with two different mesh sizes for both models, as shown in Table. 6.2

The results of the simulations are shown at minimum (t= 1 s) and maximum (t = 1.5 s) inlet velocity. The deformation of the blood vessel wall as illustrated in Fig. 6.2.2 represents the total mesh displacement when considering FSI. The maximum displacement of the structural region is observed on the dome of the aneurysm with a value of 1.58 mm for idealized geometry and 0.25 mm for patient specific geometry. The reason for the much lower deformation of the structure area of patient-specific geometry compared to the simplified geometry can be found in the much larger volume of the fluid region, by which the energy of the incoming flow can be distributed to arger area. Another explanation could be the natural origin of the patient-specific geometry.

Concerning the wall shear stress distribution, for both the patient-specific and the simplified geometry, the wall shear stress at the dome of the aneurysm is relatively low, but relatively high at the neck of the aneurysm. Average wall shear stress values as shown in Figure 6.2.3 indicate a minor difference between the simulation with and without FSI for both geometries. A similar trend was also observed for the average velocity and pressure values.

Even though the FSI simulations show only a minor differences this very first attempt clearly showed that FSI simulation can be successfully carried out on a patient-specific geometry. As a further improvement to this topic more realistic inlet and outlet boundary conditions have to be considered. In case of multiple exits from the computational domain, the specification of the various pressures at outlet is very important in order to achieve the desired mass flow ratios through the various branches. This information can be obtained by improved measurement techniques.

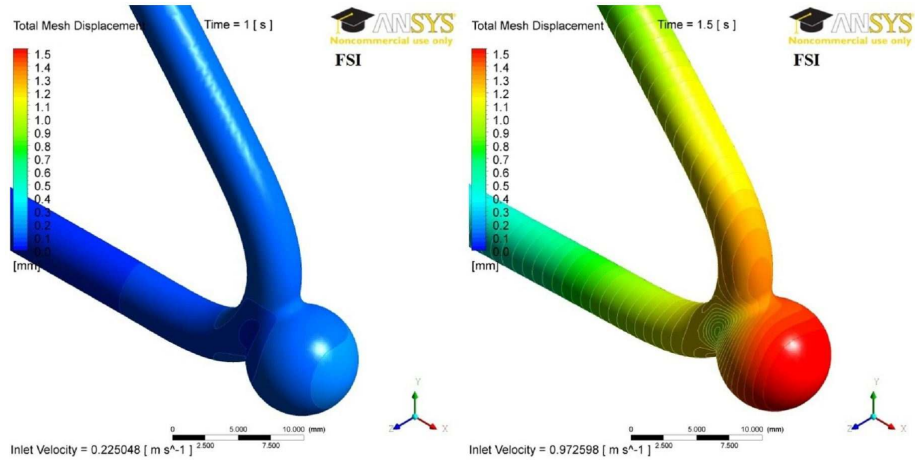

(a) Idealied sidewall aneurysm model

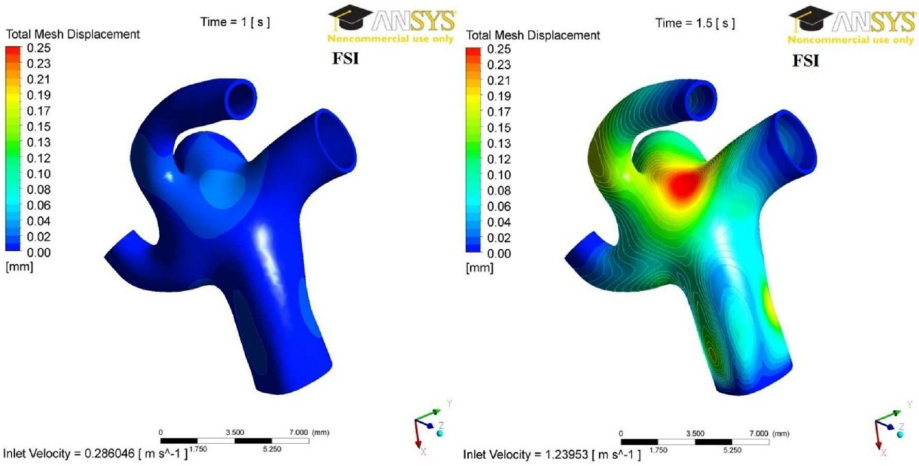

(b) Patient specific aneurysm model

Fig. 6.2.2. Deformation of the blood vessel at minimum (left) and maximum (right) structural load [171].

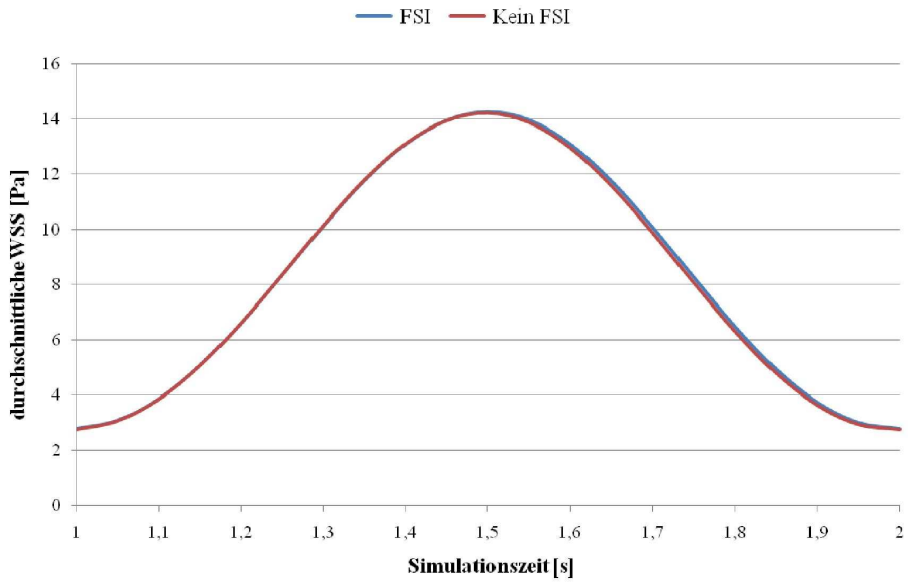

(a) Idealied sidewall aneurysm model

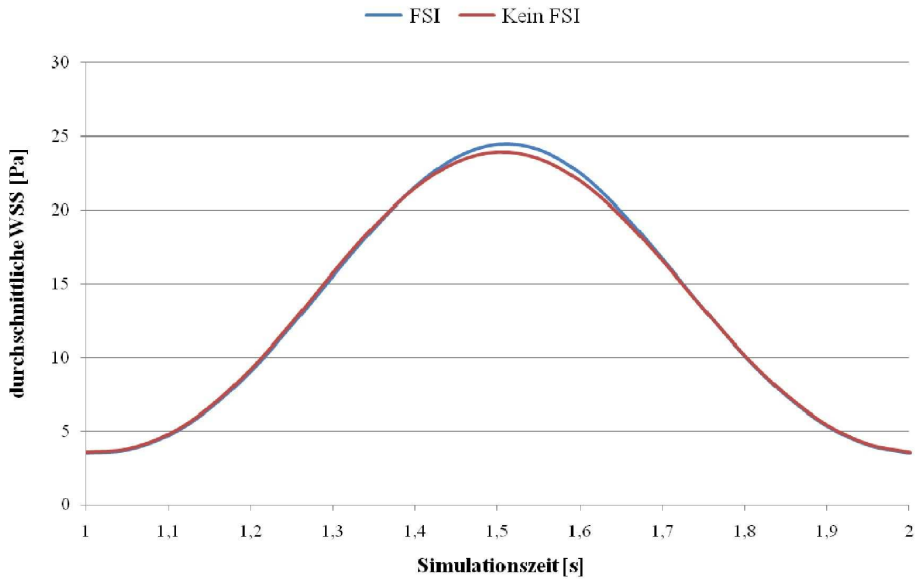

(b) Patient specific aneurysm model

Fig. 6.2.3. Comparison of average wall shear stress values over one cardiac cycle for the geometries considered. The X-scale denotes the simulation time (in s) and the Y-scale is the average wall shear stress in the aneurysm (in Pa)[171].

6.3 Imaging techniques

Rapidly improving medical imaging techniques are a first and essential source of information, delivering anatomical and morphological details. However, from the technical point of view, measuring accurately the blood flow in space and time with a high resolution is a very ambitious goal. This is mainly due to the complex geometries involved and to the high velocity of blood in the circulation, preventing for instance adequate X-ray or computer tomography scanning of contrast agent dynamics. Furthermore, for intracranial measurements, the skull hinders the successful application of many methods, for instance ultrasonic measurements. Measurements based on Magnetic Resonance Imaging are very promising but may also lead to many experimental artifacts. As a consequence, the global accuracy is often not sufficient to check the quality of numerical predictions at a sufficient level of detail. For patient-specific biomechanical simulations, great care has to be taken when generating the three-dimensional description of the geometry of interest. A fine and adequate segmentation is a prerequisite to achieve accurate and stable numerical results.

The segmentation of the MRI images performed in a semi-automatic way in this thesis showed good results, but is a time-consuming process. In order to facilitate a clinical implementation of this step, further development in the segmentation techniques and the application of more sophisticated, vessel-specific and automated algorithms are needed to improve the results in terms of accuracy and speed. Furthermore, the homogeneous wall thickness assumed in the FSI study mentioned in the previous section underestimates the wall stresses compared to a variable thickness approach. An accurate modeling of the variable wall thickness is a crucial factor affecting the computation of wall stresses. A more reliable modeling requires therefore the detection of the real non-homogeneous wall thickness from the patient images. This in turn requires further development and improvement in the current imaging techniques.

7. CONCLUSIONS AND PERSPECTIVES

7.1 Conclusions

The purpose of this work was to provide an insight into cerebral aneurysm blood flow conditions that could support clinical treatment.

The first objective of the dissertation was to validate the blood flow inside a cerebral aneurysm phantom model by comparing CFD and LDV measurements. From the literature study it was quite clear that very few authors have carried out a validation study on a true-to-scale aneurysm models. Most of the validation studies have been on simple geometries or on scaled up models. Thus, our validation study was done on a 1:1 silicone model. Experimental measurements have been carried out using non-intrusive LDV. The working fluid within in vitro models is subject to a number of constraints. First, optical techniques impose a requirement that images of the flow be undistorted. A second constraint is the requirement for matching the physical properties of the fluid. A very good refractive index matching of the fluid with that of the silicone model has been obtained with a close match of physical properties to that of blood, finally allowing successful measurement. The most challenging task during the LDV experiments, is when the hollow glass spheres seeding particle stick to the wall of the silicone model, resulting in scattering of the laser sheet and zero velocity biasing. Measurement uncertainities are attributed to the sticking of seeding particle and to large fluctuations created by the employed peristaltic pump. The data for the 3D reconstruction of the model have been provided by MRI measurement. Good agreement between the CFD and LDV was obtained for pulsatile flow in the cerebral phantom model at different planes and at different times before and after the aneurysm inside the model. Blood flow patterns and average velocity values match well. Discrepancies were most evident near model outflow. The achieved results show that CFD is helpful for better treament planning and to provide useful information regarding the hemodynamic characteristics.

As a part of the second objective the literature study showed the shortcomings of the currently employed treatment options. Even though many previous works by various authors showed that stents and flow diverterss could be sometimes considered for standalone treatment, many issues are

still unclear concerning the hemodynamic modifications induced by stent. The hemodynamic factors that influence the aneurismal formation and development are still controversial. Many investigations have been carried out, leading to ambiguous hypothesis. The most controversial parameter is the wall shear stress which is highly debated: at present, most researchers believe that high WSS trigger aneurysms rupture but low WSS trigger aneurysm growth. Therefore, the current investigation should check possible hemodynamic factors that can cause such disease. Through the use of an idealized side wall aneurysm geometry the flow dynamics have been studied considering various modifications that include straight and curved parent vessel, varying the dome to neck ratio, the aneurysm diameter the porosity of different stents and flow diverterss. Altogether 72 different cases were considered. We have investigated the effects of stenting both qualitatively and quantitatively, defining the residence time which is belived to induce thrombosis inside the aneurysm. Among the three devices considered, SILK flow diverters showed the maximum effect.

Later the virtual stenting technique has been extended to a patient specific geometry. In this manner we were able to achieve a realistic virtual stenting approach on patient geometry and to study the effects of a flow diverter on a real aneurysm. We have proposed CFD guidelines and user must take into account when doing virtual stenting in a patient specific geometries. These reommendations include mesh dependency, prism layers at the boundary regions, single-precision vs. double-precision computation, first-order vs. fecond-order discretization, and residual values for the convergence.

At last current issues have been discussed concerning in particular Newtonian vs. Non-newtonian models. Computations showed that great care must be taken when considering the blood flow model. Later, we showed that fluid-structure interaction can be successfully implemented for simple as well as patient specific geometry models. Even though the results showed only small differences with and without FSI, it is quite clear that deformation of a vessel under pressure depends on the geometry. At last we addressed the need for better image acquisition techniques to have a better representaion of computational geomtries and to allow a more accurate validation of CFD.

In conclusion of all these studies, there is no doubt that hemodynamics play a significant role in the aneurysm physiology. The methods that were developed as part of this thesis, now allow the clinician to quantify and visualize several hemodynamic patterns that were previously thought not possible, and has opened doors for future research in this area. The next step would be to conduct a larger clinical study, correlating the hemodynamic patterns with parameters of clinical outcome, and to better optimize the design of stents and flow diverters.

7.2 Perspectives

There are still numerous issues which need to be addressed in the future, ranging from computational speed, better validation, improved approaches for outflow boundary conditions, to the incorporation of models for wall mechanics. A few of the most urgent research topics to address are:

- Validation : Although the current CFD solver gave reasonably good validation results using Laser Doppler Velocimetry results, further experimental measurement techniques like Particle image velocimetry (PIV) or In vivo techniques like Magnetic Resonance Imaging should be used to refine the validation. The flow velocity should be compared first. Then, WSS value could be experimentally calculated from the velocity gradients from Stereoscopic PIV (SPIV) or Holographic PIV (HPIV).

- Outflow boundary conditions : Another topic of further research is an improved method to describe outflow boundary conditions, since there is no clear guideline. Some impose velocity or pressure-based boundary conditions, some impose zero pressure for steady-state computation, some use mass-weighted averages for single-inlet/single-outlet cases. This issue becomes even more difficult when considering several outlets.

- Optimization : Animal experiments and recent clinical trials of flow diverters [172, 173, 174, 175, 176, 177, 178] have demonstrated the utility of this approach for the treatment and exclusion of brain aneurysms from the circulation. The optimization of the wire geometry is just beginning. One such effort has been conducted by our lab on the shape of a stent design by varying different geometrical parameters, but must be pursued.

The methodology and guidelines introduced in this thesis will be used to further test hypotheses regarding hemodynamics factors and will provide the computational foundation for further research into the topics identified above. Computational modeling will enable clinicians to make treatment decisions that are quantitatively based, drastically cutting down risk of failure or need for re-treatment. It will become possible to design interventions on an individual basis, improving treatment efficiency and reducing associated risks.

REFERENCES

[1] W. Harvey. *On the Motion of the Heart and Blood in Animals.* Prometheus Books, USA, 1993.

[2] J. R. Levick. *An Introduction to Cardiovascular Physiology.* Oxford University Press, USA, 2003.

[3] G. Mchedlishvili. *Arterial Behavior and Blood Circulation in the Brain.* Bevan, J. A., Consultants Bureau, New York, 1986.

[4] P. Scheinberg and H. W. Joyne. Factors influencing cerebral blood flow and metabolism. *Circulation*, 5:225–236, 1952.

[5] J. L. Brisman, J. K. Song, and D. W. Newell. Cerebral aneurysms. *New England Journal of Medicine*, 355(9):928–939, 2006.

[6] N. F. Kassell, J. C. Torner, E. C. Jr Haley, J. A. Jane, H. P. Adams, and G. L. Kongable. The international cooperative study on the timing of aneurysm surgery. part 1: Overall management results. *Journal of Neurosurgery*, 73(1):18 – 36, 1990.

[7] G. A. Osborn. *Introduction to Cerebral Angiography.* Lippincott Williams & Wilkins; 2 edition, 1980.

[8] http://www.nlm.nih.gov.

[9] H. W. Pia. Classification of vertebro-basilar aneurysms. *Acta Neurochirurgica*, 47(1-2):3–30, 1979.

[10] J. L. Fox. *Intracranial Aneurysm*, volume 2. New York : Springer-Verlag, 1983.

[11] D. O. Wiebers. Unruptured intracranial aneurysms - risk of rupture and risks of surgical intervention. *New England Journal of Medicine*, 339(24):1725–1733, 1998.

[12] L. Parlea, R. Fahrig, D. W. Holdsworth, and S. P. Lownie. An analysis of the geometry of saccular intracranial aneurysms. *American Journal of Neuroradiology*, 20(6):1079–1089, 1999.

[13] www.bafound.org.

[14] C. T. Crowe, D. F. Elger, J. A. Roberson, and B. C. Williams. *Engineering Fluid Mechanics*. Wiley; 9th edition, 2008.

[15] J. D. Anderson. *Fundamentals of aerodynamics*. McGraw-Hill, 3rd edition, 1984.

[16] A. J. Geers, I. Larrabide, H. G. Radaelli, H. Bogunovic, H. A. F. G. van Andel, C. B. Majoie, and A. F. Frangi. Reproducibility of image-based computational hemodynamics in intracranial aneurysms: Comparison of CTA and 3DRA. In *IEEE International Symposium on Biomedical Imaging*, pages 610–613, 2009.

[17] D. A. Steinman, J. S. Milner, C. J. Norley, S. P. Lownie, and D. W. Holdsworth. Image-based computational simulation of flow dynamics in a giant intracranial aneurysm. *American Journal of Neuroradiology*, 24(4):559–566, 2003.

[18] T Hassan, E. V. Timofeev, T. Saito, H. Shimizu, M. Ezura, T. Tominaga, A. Takahashi, and K. Takayama. Computational replicas: Anatomic reconstructions of cerebral vessels as volume numerical grids at three-dimensional angiography. *American Journal of Neuroradiology*, 25(8):1356–1365, 2004.

[19] L. Jiang, C. G. Huang, P. Liu, B. Yan, J. X. Chen, H. R. Chen, R. L. Bai, and Y. C. Lu. 3-Dimensional rotational angiography for the treatment of spinal cord vascular malformations. *Surgical Neurology*, 69(4):369–373, 2008.

[20] J. R. Cebral, M. A. Castro, T. Satoh, J. Burgess, and C. M. Putman. Evaluation of image-based CFD models of cerebral aneurysms using MRI. In *ISMRM Flow Motion Workshop*, Zurich, Switzerland, 2004.

[21] C. Taylor and D. Steinman. Image-based modeling of blood flow and vessel wall dynamics: Applications, methods and future directions. *Annals of Biomedical Engineering*, 38(3):1188–1203, 2010.

[22] W. E. Dandy. Intracranial aneurysm of the internal carotid artery:cured by operation. *Annals of Surgery*, 107:654–655, 1938.

[23] Y. Orz, S. Kobayashi, M. Osawa, and Y. Tanaka. Aneurysm size: A prognostic factor for rupture. *British Journal of Neurosurgery*, 11(2):144–149, 1997.

[24] A. K. Wakhloo, G. Lanzino, B. B. Lieber, and L. N. Hopkins. Stent for intracranial aneurysms: the beginning of a new endovascular era? *Neurosurgery*, 43:377–379, 1998.

[25] www.cxvascular.com/vn-archives/vascular-news.

[26] J. Moret, L. Pierot, and A. Boulin. Remodelling of the arterial wall of the parent vessel in the endovascular treatment of intracranial aneurysms. *Neuroradiology*, Suppl 1:383, 1994.

[27] L. Solymosi, R. Chapot, and M. Bendszus. Stent, ballon oder clip? *Klinische Neuroradiologie*, 15:145–160, 2005.

[28] www.ev3.net.

[29] S. D. Simon, D. K. Lopes, and R. A. Mericle. Use of intracranial stenting to secure unstable liquid embolic casts in wide-neck sidewall intracranial aneurysms. *Neurosurgery*, 66(92-7), 2010.

[30] www.bostonscientific.com.

[31] www.cordis.com.

[32] B. Utter and J. S. Rossmann. Influence of shape on saccular aneurysm hemodynamics and risk of rupture. In *32nd annual Bioengineering Conference Proceeding of IEEE*, pages 21–22, 2006.

[33] A. Mantha, C. Karmonik, G. Benndorf, C. Strother, and R. Metcalfe. Hemodynamics in a cerebral artery before and after the formation of an aneurysm. *American Journal of Neuroradiology*, 27(5):1113–8, 2006.

[34] Y. Feng, S. Wada, K. Tsubota, and T. Yamaguchi. Growth of intracranial aneurysms arised from curved vessels under the influence of elevated wall shear stress : a computer simulation study. *Japan Society of Mechanical Engineering International Journal*, 47:1035–1042, 2004.

[35] L. D. Jou, G. Wong, B. Dispensa, M. T. Lawton, R. T. Higashida, W. L. Young, and D. Saloner. Correlation between lumenal geometry changes and hemodynamics in fusiform intracranial aneurysms. *American Journal of Neuroradiology*, 26(9):2357–2363, 2005.

[36] G. N. Foutrakis, H. Yonas, and R. J. Sclabassi. Finite element methods in the simulation and analysis of intracranial blood flow. *Neurological Research*, 19(2):174–86, 1997.

[37] C. F. Gonzalez, Y. I. Cho, H. V. Ortega, and J. Moret. Intracranial aneurysms: Flow analysis of their origin and progression. *American Journal of Neuroradiology*, 13(1):181–188, 1992.

[38] M. Shojima, M. Oshima, K. Takagi, R. Torii, M. Hayakawa, K. Katada, A. Morita, and T. Kirino. Magnitude and role of wall shear stress on cerebral aneurysm: computational fluid dynamic study of 20 middle cerebral artery aneurysms. *Stroke*, 35(11):2500–2505, 2004.

[39] W. E. Stehbens. Etiology of intracranial berry aneurysm. *Journal of Neurosurgery*, 70:823–831, 1989.

[40] H. J. Steiger. Pathophysiology of development and rupture of cerebral aneurysms. *Acta Neurochirurgica, Supplement*, 48:1–57, 1990.

[41] J. R. Cebral, M. A. Castro, J. E. Burgess, R. S. Pergolizzi, M. J. Sheridan, and C. M. Putman. Characterization of cerebral aneurysms for assessing risk of rupture by using patient-specific computational hemodynamics models. *American Journal of Neuroradiology*, 26(10):2550–9, 2005.

[42] Y. Hoi, H. Meng, S. H. Woodward, B. R. Bendok, R. A. Hanel, L. R. Guterman, and L. N. Hopkins. Effects of arterial geometry on aneurysm growth: three-dimensional computational fluid dynamics study. *Journal of Neurosurgery*, 101(4):676–81, 2004.

[43] Y. Yoshimoto. Cerebral aneurysms unrelated to arterial bifurcations. *Acta Neurochirurgica*, 138(8):958, 1996.

[44] L. G. Schachter and A. I. Barakat. Computational study of arterial flow disturbance induced by intravascular stents. In *American Society of Mechanical Engineers, Bioengineering Division (Publication) BED*, volume 50, pages 877–878, 2001.

[45] D. M. Wootton and D. N. Ku. Fluid mechanics of vascular systems, diseases, and thrombosis. *Annual Review of Biomedical Engineering*, 1:299–329, 1999.

[46] I. Chatziprodromou, V. D. Butty, V. B. Makhijani, D. Poulikakos, and Y. Ventikos. Pulsatile blood flow in anatomically accurate vessels

with multiple aneurysms: A medical intervention planning application of computational hemodynamics. *Flow, Turbulence and Combustion*, 71(1-4):333–346, 2003.

[47] J. R. Cebral and R. Löhner. From medical images to CFD meshes. In *Proceedings of the 8th International Meshing Roundtable*, pages 321–331, 1999.

[48] J. R. Cebral, M. A. Castro, D. Millan, A. Frangi, and C. M. Putman. Pilot clinical study of aneurysm rupture using image-based computational fluid dynamics models. In *Progress in Biomedical Optics and Imaging - Proceedings of SPIE*, volume 5746, pages 245–256, 2005.

[49] V. D. Butty, P. Buchel, Y. Ventikos, K. Gudjonsson, V. B. Makhijani, and D. Poulikakos. Flow through a realistic arterial geometry with two aneurysms: Mixing characteristics and residence times. *American Society of Mechanical Engineers, Fluids Engineering Division (Publication) FED*, 256:53–58, 2000.

[50] V. D. Butty, K. Gudjonsson, P. Buchel, V. B. Makhijani, Y. Ventikos, and D. Poulikakos. Residence times and basins of attraction for a realistic right internal carotid artery with two aneurysms. *Biorheology*, 39(3-4):387–393, 2002.

[51] A. C. Burleson, C. M. Strother, V. T. Turitto, H. H. Batjer, S. Kobayashi, and R. E. Harbaugh. Computer modeling of intracranial saccular and lateral aneurysms for the study of their hemodynamics. *Neurosurgery*, 37(4):774–784, 1995.

[52] H. V. Ortega. Technical report: Computer simulation helps predict cerebral aneurysms. *Journal of Medical Engineering and Technology*, 22(4):179–181, 1998.

[53] A. Valencia, A. Zarate, M. Galvez, and L. Badilla. Non-newtonian blood flow dynamics in a right internal carotid artery with a saccular aneurysm. *International Journal for Numerical Methods in Fluids*, 50(6):751–764, 2006.

[54] A. Valencia. Simulation of unsteady laminar flow in models of terminal aneurysm of the basilar artery. *International Journal of Computational Fluid Dynamics*, 19(4):337–345, 2005.

[55] A. Valencia and F. Solis. Blood flow dynamics and arterial wall interaction in a saccular aneurysm model of the basilar artery. *Computers and Structures*, 84(21):1326–1337, 2006.

[56] K. Baráth, F. Cassot, D. A. Rüfenacht, and J. H. D. Fasel. Anatomically shaped internal carotid artery aneurysm in vitro model for flow analysis to evaluate stent effect. *American Journal of Neuroradiology*, 25(10):1750–1759, 2004.

[57] D. W. Liepsch, H. J. Steiger, A. Poll, and H. J. Reulen. Hemodynamic stress in lateral saccular aneurysms. *Biorheology*, 24(6):689–710, 1987.

[58] H. Niimi, Y. Kawano, and I. Sugiyama. Structure of blood flow through a curved vessel with an aneurysm. *Biorheology*, 21(4):603–615, 1984.

[59] T. M. Liou, W. C. Chang, and C. C. Liao. Experimental study of steady and pulsatile flows in cerebral aneurysm model of various sizes at branching site. *Journal of Biomechanical Engineering*, 119(3):325–332, 1997.

[60] R. S. Danturthi, L. D. Partridge, and V. T. Turitto. Investigation of flow in the models of intracranial lateral aneurysms by particle image velocimetry. In *Southern Biomedical Engineering Conference - Proceedings*, pages 437–440, 1997.

[61] Y. Bando, M. Oshima, and M. Oishi. Stereoscopic PIV measurement of pulsatile flow in an in vitro model of cerebral aneurysm. In *12th International Symposium on Flow Visualization*, pages 1–7, German Aerospace Center (DLR), Göttingen, Germany, 2006.

[62] D. I. Hollnagel, P. E. Summers, S. S. Kollias, and D. Poulikakos. Laser doppler velocimetry LDV and 3D phase-contrast magnetic resonance angiography PC-MRA velocity measurements: Validation in an anatomically accurate cerebral artery aneurysm model with steady flow. *Journal of Magnetic Resonance Imaging*, 26(6):1493–1505, 2007.

[63] S. Tateshima, K. Tanishita, H. Omura, J. P. Villablanca, and F. Vinuela. Intra-aneurysmal hemodynamics during the growth of an unruptured aneurysm: In vitro study using longitudinal CT angiogram database. *American Journal of Neuroradiology*, 28(4):622–627, 2007.

[64] L. Boussel, V. Rayz, C. McCulloch, A. Martin, G. Acevedo-Bolton, M. Lawton, R. Higashida, W. S. Smith, W. L. Young, and D. Saloner.

Aneurysm growth occurs at region of low wall shear stress. Patient-specic correlation of hemodynamics and growth in a longitudinal study. *Stroke*, (39):2997–3002, 2008.

[65] H. Ujiie, Y. Tamano, K. Sasaki, and T. Hori. Is the aspect ratio a reliable index for predicting the rupture of a saccular aneurysm? *Neurosurgery*, 48(3):495–503, 2001.

[66] D. O. Wiebers, J. P. Whisnant, and T. M. Sundt. The significance of unruptured intracranial saceular aneurysms. *Journal of Neurosurgery*, 66:23–29, 1987.

[67] M. A. Castro, C. M. Putman, and J. R. Cebral. Patient-specific computational modeling of cerebral aneurysms with multiple avenues of flow from 3d rotational angiography images. *Academic Radiolology*, 13(7):811–821, 2006.

[68] Y. Imai, K. Sato, T. Ishikawa, and T. Yamaguchi. Inflow into saccular cerebral aneurysms at arterial bends. *Annals of Biomedical Engineering*, 36(9):1489 –1495, 2008.

[69] K. Perktold, T. Kenner, D. Hilbert, B. Spork, and H. Florian. Numerical blood flow analysis: arterial bifurcation with a saccular aneurysm. *Basic Research in Cardiology*, 83(1):24–31, 1988.

[70] M. Low, K. Perktold, and R. Raunig. Hemodynamics in rigid and distensible saccular aneurysms: A numerical study of pulsatile flow characteristics. *Biorheology*, 30(3-4):287–298, 1993.

[71] P. Venugopal, D. Valentino, H. Schmitt, J. P. Villablanca, F. Vinuela, and G. Duckwiler. Sensitivity of patient-specific numerical simulation of cerebal aneurysm hemodynamics to inflow boundary conditions. *Journal of Neurosurgery*, 106:1051–1060, 2007.

[72] S. Z. Zhao, X. Y. Xu, A. D. Hughes, S. A. Thom, A. V. Stanton, B. Ari, and B. Long. Blood flow and vessel mechanics in a physiologically realistic model of a human carotid arterial bifurcation. *Journal of Biomechanical Engineering*, 33(8):975–984, 2000.

[73] E. S. Di Martino, G. Guadagni, G. Ballerini A. Fumero, R. Spirito, P. Biglioli, and A. Redaelli. Fluid-structure interaction within realistic three-dimensional models of the aneurysmatic aorta as a guidance to assess the risk of rupture of the aneurysm. *Medical Engineering and Physics*, 23(9):647–655, 2001.

[74] I. Chatziprodromou, D. Poulikakos, and Y. Ventikos. On the influence of variation in hemodynamic conditions on the generation and growth of cerebral aneurysms and atherogenesis: A computational model. *Journal of Biomechanical Engineering*, 40(16):3626–3640, 2007.

[75] A. Gnasso, C. Carallo, C. Irace, M. S. De Franceschi, P. L. Mattioli, C. Motti, and C. Cortese. Association between wall shear stress and flow-mediated vasodilation in healthy men. *Atherosclerosis*, 156(1):171–176, 2001.

[76] D. N. Ku, D. P. Giddens, C. Z. Zarins, and S. Glagov. Pulsatile flow and atherosclerosis in the human carotid bifurcation. *Arteriosclerosis*, 5(8):293–302, 1985.

[77] Q. H. Wang, L. T. Ma, Z. Q. Wu, J. Q. Gong, J. H. Dai, X. J. Zhang, and F. Shu. Formation and hemodynamics of pseudoaneurysm after rupture and bleeding of aneurysm: an experiment with dogs. *Zhonghua Yi Xue Za Zhi (National Medical Journal of China)*, 85(32):2259–2263, 2005.

[78] J. R. Cebral, R. S. Pergolizzi Jr, and C. M. Putman. Computational fluid dynamics modeling of intracranial aneurysms: Qualitative comparison with cerebral angiography. *Academic Radiolology*, 14(7):804–813, 2007.

[79] T. A. Hope, M. D. Hope, D. D. Purcell, C. Morze, D. B. Vignerona, M. T. Alleyb, and W. P. Dillona. Evaluation of intracranial stenoses and aneurysms with accelerated 4d flow. *Magnetic Resonance Imaging*, 28:41–46, 2010.

[80] J. R. Cebral, R. Löhner, and J. Burgess. Computer simulation of cerebral artery clipping: Relevance to aneurysm neuro-surgery planning. In *European Congress on Computational Methods in Applied Sciences and Engineering, ECCOMAS 2000*, pages 1–20, Barcelona, 2000.

[81] Y. Hoi, C. N. Ionita, R. V. Tranquebar, K. R. Hoffmann, S. H. Woodward, D. B. Taulbee, H. Meng, and S. Rudin. Flow modification in canine intracranial aneurysm model by an asymmetric stent: Studies using digital subtraction angiography DSA and image-based computational fluid dynamics CFD analyses. In *Progress in Biomedical Optics and Imaging - Proceedings of SPIE*, volume 6143 I, 2006.

[82] H. Niazmand, A. Sepehr, and P. B. Shahabi. Numerical analysis of aneurysm using pulsatile blood flow through a locally expanded vessel.

In P. Wesseling, E. Oñate, and J. Périaux, editors, *European Conference on Computational Fluid Dynamics, ECCOMAS CFD 2006*, pages 303/1–18, Egmond aan Zee (The Netherlands), 2006.

[83] R. Oshima, M. Torii and T. Kobayashi. Experimental and computational visualization of blood flows in macro and micro scales. In *12th International Symposium on Flow Visualization*, pages 1–8, German Aerospace Center (DLR), Göttingen, Germany, 2006.

[84] B. B. Lieber, V. Livescu, L. N. Hopkins, and A. K. Wakhloo. Particle image velocimetry assessment of stent design influence on intraaneurysmal flow. *Annals of Biomedical Engineering*, 30(6):768–777, 2002.

[85] M. L. Li, C. Y. Chou, L. C. Lee, C. Y. Shen, and R. J. Shih. Nonnewtonian flow analysis in intracoronary stent placement. In *12th International Symposium on Flow Visualization*, pages 1–7, Göttingen, Germany, 2006.

[86] A. K. Wakhloo, F. Schellhammer, J. de Vries, J. Haberstroh, and M. Schumacher. Selfexpanding and ballon-expandable stents in the treatment of carotid aneurysms: an experimental study in a canine model. *American Journal of Neuroradiology*, 15:493–502, 1994.

[87] G. Geremia, M. Haklin, and L. Brennecke. Embolization of experimentally created aneurysms with intravascular stent devices. *American Journal of Neuroradiology*, 15:1223–1231, 1994.

[88] M. D. Ford, H. N. Nikolov, J. S. Milner, S. P. Lownie, E. M. DeMont, W. Kalata, F. Loth, D. W. Holdsworth, and D. A. Steinman. PIV - measured versus CFD - predicted flow dynamics in anatomically realistic cerebral aneurysm models. *Journal of Biomechanical Engineering*, 130(2):02–10, 2008.

[89] F. Dorn, F. Niedermeyer, A. Balasso, D. Liepsch, and T. Liebig. The effect of stents on intra-aneurysmal hemodynamics: in vitro evaluation of a pulsatile sidewall aneurysm using laser Doppler anemometry. *Neuroradiology*, 53(4):267–272, 2010.

[90] B. B. Lieber, M. Aenis, Y. Zhao, and A. K. Wakhloo. Flow characteristics in a stented and non-stented side wall aneurysm model. In *American Society of Mechanical Engineers, Bioengineering Division (Publication) BED*, volume 31, pages 379–380, 1995.

[91] C. C. Nichita, B. B. Lieber, and E. B. Pitman. Numerical simulation of flow in a stented and nonstented cerebral arterial segment with a side wall aneurysm using the immersed boundary technique. *Annals of Biomedical Engineering*, 28(1):61, 2000.

[92] G. Canton, D. I. Levy, and J. C. Lasheras. Changes in the intra-aneurysmal hemodynamics due to stent placement in sidewall and bifurcating cerebrovascular aneurysms. In *Division of Fluid Dynamics, 56th Annual Meeting*, 2003.

[93] F. Nicoud, H. Vernhet, and M. Dauzat. A numerical assessment of wall shear stress changes after endovascular stenting. *Journal of Biomechanics*, 38(10):2019–2027, 2005.

[94] M. Ohta, S. G. Wetzel, P. Dantan, C. Bachelet, K. O. Lovblad, H. Yilmaz, P. Flaud, and D. A. Rüfenacht. Rheological changes after stenting of a cerebral aneurysm: A finite element modeling approach. *Cardio-Vascular and Interventional Radiology*, 28(6):768–772, 2005.

[95] R. Balossino, F. Gervaso, F. Migliavacca, and G. Dubini. Effects of different stent designs on local hemodynamics in stented arteries. *Journal of Biomechanics*, 41(5):1053–1061, 2008.

[96] B. Chopard, R. Ouared, and D. A. Rüfenacht. A Lattice Boltzmann simulation of clotting in stented aneursysms and comparison with velocity or shear rate reductions. *Mathematics and Computers in Simulation*, 72(2-6):108–112, 2006.

[97] B. B. Lieber, A. P. Stancampiano, and A. K. Wakhloo. Alteration of hemodynamics in aneurysm models by stenting: Influence of stent porosity. *Annals of Biomedical Engineering*, 25(3):460–469, 1997.

[98] T. M. Liou and S. N. Liou. Pulsatile flows in a lateral aneurysm anchored on a stented and curved parent vessel. *Experimental Mechanics*, 44(3):253–260, 2004.

[99] L. Miskolczi, L. R. Guterman, J. D. Flaherty, I. Szikora, and L. N. Hopkins. Rapid saccular aneurysm induction by elastase application in vitro. *Neurosurgery*, 41:220–229, 1997.

[100] L. Miskolczi, L. R. Guterman, J. D. Flaherty, and L. N. Hopkins. Saccular aneurysm induction by elastase digestion of the arterial wall: A new animal model. *Neurosurgery*, 43:595–600, 1998.

[101] H. J. Cloft, T. A. Altes, W. F. Marx, R. J. Raible, S. B. Hudson, G. A. Helm, J. W. Mandell, M. E. Jensen, J. E. Dion, and D. F. Kallmes. Endovascular creation of an in vivo bifurcation aneurysm model in rabbits. *Radiology*, 213(223-228), 1999.

[102] W. E. Stehbens. Histological changes in chronic experimental aneurysms surgically fashioned in sheep. *Pathology*, 29(4):374–379, 1997.

[103] J. Seong, A. K. Wakhloo, and B. B. Lieber. In vitro evaluation of flow divertors in an elastase-induced saccular aneurysm model in rabbit. *Journal of Biomechanical Engineering*, 129(6):863–872, 2007.

[104] K. Knox, C. W. Kerber, S. A. Singel, M. J. Bailey, and S. G. Imbesi. Rapid prototyping to create vascular replicas from CT scan data: Making tools to teach, rehearse, and choose treatment strategies. *Catheterization and Cardiovascular Interventions*, 65(1):47–53, 2005.

[105] G. R. Cokelet. The rheology of the human blood. In Y. C. Fun, N. Perrone, and M. Anliker, editors, *Biomechanics: Its Functions and Objectives*, pages 63–103. Prentice-Hall, Englewood Cliffs, New Jersey, 1972.

[106] D. W. Liepsch. Flow in tubes and arteries - a comparison. *Biorheology*, 23(4):395–433, 1986.

[107] G. B. Thurston. Viscoelasticity of human blood. *Journal of Biophysics*, 12:1205–1212, 1972.

[108] G. B. Thurston. Frequency and shear rate dependence of viscoelasticity of human blood. *Biorheology*, (10):375–381, 1973.

[109] D. E. Mann and J. M. Tarbell. Flow of non-newtonian blood analog fluids in rigid curved and straight artery models. *Biorheology*, 27:711–733, 1990.

[110] W. L. Lim, Y. T. Chew, T. C. Chew, and H. T. Low. Particle image velocimetry in the investigation of flow past articial heart valves. *Annals of Biomedical Engineering*, 22:307–318, 1994.

[111] R. Budwig. Refractive index matching methods for liquid flow investigations. *Experiment in Fluids*, 17:350–355, 1994.

[112] S. Hendrik and A. Aviram. Use of zinc iodide solutions in flow research. *Review of Scientific Instrumentation*, 53(1):75–78, 1982.

[113] F. J. H. Gijsen, F. N. van de Vosse, and J. D. Janssen. The influence of the non-newtonian properties of blood on the flow in large arteries: steady flow in a carotic bifurcation model. *Journal of Biomechanics*, 32:601–608, 1998.

[114] F. J. H. Gijsen, F. N. van de Vosse, and J. D. Janssen. The influence of the non-newtonian properties of blood on the flow in large arteries: unsteady flow in a 90 curved tube. *Journal of Biomechanics*, 32:705–713, 1999.

[115] J. T. Wernicke, D. Meier, K. Mizuguchi, G. Damm, G. Aber, R. Benkowski, Y. Nose, G. P. Noon, and M. E. DeBakey. A fluid dynamic analysis using flow visualization of the baylor/nasa implantable axial flow blood pump for design improvement. *Artificial Organs*, 19(2):161–177, 1995.

[116] W. W. Nichols and M. F. O'Rourke. *McDonald's Blood Flow in Arteries*. SAGE Publication, London, 5th edition, 1998.

[117] Z. Mátrai, R. Bordás, G. Janiga, and D. Thévenin. Laser Doppler Velocimetry measurements in artificial medical models. In P. Bikfalvi, editor, *XXIV. microCAD International Scientific Conference*, pages 45–50, Miskolc, Hungary, 2010.

[118] S. Seshadhri, G. Janiga, R. Bordás, M. Skalej, and D. Thévenin. Experimental validation of numerical simulations on a cerebral aneurysm phantom model. *Medical Engineering and Physics*, Submitted, 2011.

[119] www.dantecdynamics.com.

[120] R. Bade, C. Schumann, S. Seshadhri, G. Janiga, T. Bölke, O. Gürvit, M. Skalej, G. Rose, D. Thévenin, and B. Preim. Effiziente Generierung von Oberflächenmodellen für die Simulation des zerebralen Blutflusses. In *6. Jahrestagung der Deutschen Gesellschaft für Computergestützte Chirurgie (CURAC)*, pages 125 –128, Karlsruhe, Germany, 2007.

[121] G. Janiga, S. Seshadhri, O. Beuing, M. Neugebauer, R. Gasteiger, B. Preim, G. Rose, M. Skalej, and D. Thévenin. Guidelines for accurate numerical flow simulations of stented cerebral aneurysms : A VISC09 case. *Journal of Biomechanics*, Submitted, 2011.

[122] G. Janiga, O. Beuing, S. Seshadhri, M. Neugebauer, R. Gasteiger, B. Preim, G. Rose, M. Skalej, and D. Thévenin. Virtual stenting using real patient data. In *Conference on Modelling Fluid Flow (the 14th*

International Conference on Fluid Flow Technologies), pages 111–117. (Vad, J., Ed.), Budapest, Hungary, ISBN 978-963-420-987-4, 2009.

[123] M. Casey and T. Wintergerste. *Quality and Trust in Industrial CFD: Best Practice Guidelines*. ERCOFTAC, 2000.

[124] C. Sadasivan, B. B. Lieber, M. Gounis, D. Lopes, and N. Hopkins, L. Angiographic quantification of contrast medium washout from cerebral aneurysms after stent placement. *American Journal of Neuroradiology*, 23:1214 – 1221, 2002.

[125] J. R. Cebral, M. A. Castro, J. E. Burgess, R. S. Pergolizzia, M. J. Sheridan, and C. M. Putman. Characterization of cerebral aneurysms for assessing risk of rupture by using patient-specific computational hemodynamics models. *American Journal of Neuroradiology*, 26:2550–59, 2005.

[126] S. Tateshima, A. Chien, J. Sayre, J. Cebral, and F. Viñuela. The effect of aneurysm geometry on the intra-aneurysmal flow condition. *Neuroradiology*, pages 1–7, 2010.

[127] H. J. Steiger, R. Aaslid, S. Keller, and H. Reulen. Strength, elasticity and viscoelastic properties of cerebral aneurysms. *Heart Vessels*, 5:41–46, 1989.

[128] A. Barakat and E. Cheng. Numerical simulation of fluid mechanical disturbance induced by intravascular stents. In *International Conference on Mechanics in Medicine and Biology ICMMB-11*, Hawaï, 2000.

[129] J. L. Ottesen, M. S. Olufsen, and J. K. Larsen. *Applied Mathematical models in Human Physiology, SIAM Monograph on mathematical modeling and computation*. SIAM: Society for Industrial and Applied Mathematics; 1st edition, 2004.

[130] H. J. Steiger, K. Perktold, and V. T. Turitto. Computer modeling of intracranial saccular and lateral aneurysms for the study of their hemodynamics. *Neurosurgery*, 41(1):326–327, 1997.

[131] S. Scott, G. Ferguson, and M. Roach. Comparison of the elastic properties of human intracranial arteries and aneurysms. *Canadian Journal of Physiology and Pharmacology*, 50:328–332, 1972.

[132] M. Kim, E. I. Levy, H. Meng, and L. N. Hopkins. Quantification of hemodynamic changes induced by virtual placement of multiple

stents across a wide-necked basilar trunk aneurysm. *Neurosurgery*, 61(6):1305–1312, 2007.

[133] S. Seshadhri, G. Janiga, B. Preim, G. Rose, M. Skalej, and D. Thévenin. Numerical simulation and experimental validation in an exact aortic arch aneurysm model. In *4th European Conference of the International Federation for Medical and Biological Engineering*, volume 22, pages 1975–1979. Antwerp, Springer, 2008.

[134] M. Kim, D. B Taulbee, M. Tremmel, and H. Meng. Comparison of two stents in modifying cerebral aneurysm hemodynamics. *Annals of Biomedical Engineering*, 36(5):726–741, 2008.

[135] H. Meng, Z. Wang, M. Kim, R. D. Ecker, and L. N. Hopkins. Saccular aneurysms on straight and curved vessels are subject to different hemodynamics: implications of intravascular stenting. *American Journal of Neuroradiology*, 27(9):1861–5, 2006.

[136] S. C. M. Yu and J. B. Zhao. A steady flow analysis on the stented and non-stented sidewall aneurysm models. *Medical Engineering and Physics*, 21:133–141, 1999.

[137] M. Aenis, A. Stancampiano, A. J. Wakhloo, and B. B. Lieber. Modeling of flow in a straight stented and nonstented side wall aneurysm model. *Journal of Biomechanical Engineering*, 119:206–212, 1997.

[138] G. Geremia, T. Brack, L. Brennecke, M. Haklin, and R. Falter. Occlusion of experimentally created fusiform aneurysms with porous metallic stents. *American Journal of Neuroradiology*, 21:739–745, 2000.

[139] G. Benndorf, U. Herban, W. Sollmann, and A. Campi. Treatment of a ruptured dissecting vertebral artery aneurysm with double stent placement: Case report. *American Journal of Neuroradiology*, 22:1844–1848, 2001.

[140] M. Ohta, M. Hirabayashi, and S. Wetzel. Impact of stent design on intra-aneurysmal flow. *Interventional Neuroradiology*, 10:85–94, 2004.

[141] J. C. Palmaz. Intravascular stent: tissue-stent interactions and design considerations. *American Journal of Roentgenology*, 160:613–618, 1993.

[142] A. K. Wakhloo, F. O. Tio, B. B. Lieber, F. Schellhammer, M. Graf, and L. N. Hopkins. Self expanding nitinol stents in canine vertebral arteries: hemodynamics and tissue response. *American Journal of Neuroradiology*, 16:1043–1051, 1995.

[143] N. F. Kassell and J. C. Torner. Size of intracranial aneurysms. *Neurosurgery*, 12(3):291–297, 1983.

[144] B. Weir. Unruptured intracranial aneurysms: A review. *Journal of Neurosurgery*, 96(1):3–42, 2002.

[145] D. M. Sforza, C. M. Putman, and J. R. Cebral. Hemodynamics of cerebral aneurysms. *Annual Review of Fluid Mechanics*, 41:91–107, 2009.

[146] G. R. Stuhne and D. A. Steinman. Finite-element modeling of the hemodynamics of stented aneurysms. *Journal of Biomechanical Engineering*, 126(3):382–387, 2004.

[147] M. Kim, C. N. Ionita, R. V. Tranquebar, K. R. Hoffmann, D. B. Taulbee, H. Meng, and S. Rudin. Evaluation of an asymmetric stent patch design for a patient specific intracranial aneurysm using computational fluid dynamic CFD calculations in the computed tomography CT derived lumen. In Armando Manduca and Amir A. Amini, editors, *Proceedings of SPIE 6143 II, Medical Imaging 2006: Physiology, Function, and Structure from Medical Images*, volume 6143, 2006.

[148] G. Tabor, D. Tame, F. Pierron, P. Young, A. Watkinson, and J. Thompson. Patient-specific arterial flow simulation with additional geometric elements. In P. Wesseling, E. Oñate, and J. Périaux, editors, *European Conference on Computational Fluid Dynamics, ECCOMAS CFD 2006*, pages 228/1–12, Egmond aan Zee (The Netherlands), 2006.

[149] G Lanzino, A. K. Wakhloo, R. D. Fessler, M. L. Hartney, L. R. Guterman, and L. N. Hopkins. Efficacy and current limitations of intravascular stents for intracranial internal carotid, vertebral, and basilar artery aneurysms. *Journal of Neurosurgery*, 91(4):538–546, 1999.

[150] A.G. Radaelli, L. Augsburger, J.R. Cebral, M. Ohta, D.A. Rüfenacht, R. Balossino, G. Benndorf, D.R. Hose, A. Marzo, R. Metcalfe, P. Mortier, F. Mut, P. Reymond, L. Socci, B. Verhegghe, and A.F. Frangi. Reproducibility of hemodynamical simulations in a subject-specific stented aneurysm model - a report on the virtual intracranial stenting challenge 2007. *Journal of Biomechanics*, 41(10):2069–2081, 2008.

[151] J. Schöberl. Netgen: An advancing front 2D/3D-mesh generator based on abstract rules. *Computing and Visualization in Science*, 1(1):41–52, 1997.

[152] S. J. Owen and D. R. White. Mesh-based geometry. *International Journal for Numerical Methods in Engineering*, 58(2):375–395, 2003.

[153] C. Schumann, M. Neugebauer, R. Bade, B. Preim, and H. O. Peitgen. Implicit vessel surface reconstruction for visualization and CFD simulation. *International Journal of Computer Assisted Radiology and Surgery*, 2(5):275–286, 2007.

[154] L. Antiga and D. A. Steinman. Robust and objective decomposition and mapping of bifurcating vessels. *IEEE Transactions on Medical Imaging*, 23(6):704–713, 2004.

[155] M. Neugebauer, G. Janiga, S. Zachow, M. Skalej, and B. Preim. Generierung qualitativ hochwertiger Modelle für die Simulation von Blutuss in zerebralen Aneurysmen. In *Simulation and Visualization 2008*, pages 221–236, Magdeburg, Germany, 2008.

[156] Y. Hoi, S.H. Woodward, M. Kim, D.B. Taulbee, and H. Meng. Validation of CFD simulations of cerebral aneurysms with implication of geometric variations. *Journal of Biomechanical Engineering*, 128(6):844–851, 2006.

[157] D. M. Sforza, C. M. Putman, E. Scrivano, P. Lylyk, and J. R. Cebral. Blood-flow characteristics in a terminal basilar tip aneurysm prior to its fatal rupture. *American Journal of Neuroradiology*, 31(6):1127–1131, 2010.

[158] R. Löhner, J. Cebral, O. Soto, P. Yim, and J. E. Burgess. Applications of patient-specific CFD in medicine and life sciences. *International Journal for Numerical Methods in Fluids*, 43(6-7):637–650, 2003.

[159] C. W. Ryu, O. K. Kwon, J. S. Koh, and E. J. Kim. Analysis of aneurysm rupture in relation to the geometric indices: aspect ratio, volume, and volume-to-neck ratio. *Neuroradiology*, in press:1–7, 2010.

[160] S. Dhar, M. Tremmel, J. Mocco, M. Kim, J. Yamamoto, A. H. Siddiqui, L. N. Hopkins, and H. Meng. Morphology parameters for intracranial aneurysm rupture risk assessment. *Neurosurgery*, 63(2):185–196, 2008.

[161] A. C. Burleson and V. T. Turitto. Identification of quantifiable hemodynamic factors in the assessment of cerebral aneurysm behavior. *Thrombosis and Haemostasis*, 76(1):118–124, 1996.

[162] J. Xiang, S.K. Natarajan, M. Tremmel, D. Ma, J. Mocco, L.N. Hopkins, A.H. Siddiqui, E.I. Levy, and H. Meng. Hemodynamic-morphologic discriminants for intracranial aneurysm rupture. *Stroke*, in press, 2010.

[163] S. Seshadhri, G. Janiga, M. Skalej, and D. Thévenin. Impact of different flow diverters on hemodynamics in an idealized aneurysm model. *Journal of Biomechanical Engineering*, Accepted for publication, 2011.

[164] J. H. Ferziger and M. Perić. *Computational Methods for Fluid Dynamics*. Springer, Berlin, third edition, 2002.

[165] A. Leuprecht and K. Perktold. Computer simulation of non-newtonian effects on blood flow in large arteries. *Computer Methods in Biomechanical and Biomedical Engineering*, 4:149–163, 2001.

[166] A. Quarteroni, M. Tuveri, and A. Veneziani. Computational vascular fluid dynamics: Problems, models and methods. *Computing and Visualization in Science*, 2(4):163–197, 2000.

[167] G. Pontrelli. Pulsatile blood flow in a pipe. *Computer and Fluids*, 27(3):367–380, 1998.

[168] Y. Bazilevs, M. Hsu, Y. Zhang, W. Wang, X. Liang, T. Kvamsdal, R. Brekken, and J. G. Isaksen. A fully-coupled fluid-structure interaction simulation of cerebral aneurysms. *Computational mechanics*, 46(1):3–16, 2010.

[169] K. Takizawa, J. Christopher, T. E. Tezduyar, and S. Sathe. Space-time finite element computation of arterial fluid-structure interactions with patient-specific data. *International Journal for Numerical Methods in Biomedical Engineering*, 26(1):101–116, 2010.

[170] R. Torii, M. Oshima, T. Kobayashi, K. Takagi, and T. E. Tezduyar. Influence of wall thickness on fluid-structure interaction computations of cerebral aneurysms. *International Journal for Numerical Methods in Biomedical Engineering*, 26(3-4):336–347, 2010.

[171] M. Quast. Numerical modeling of cerebral blood flows using fluid-structure coupling, Diploma Thesis, 2011.

[172] C. Sadasivan, L. Cesar, J. Seong, A. K. Wakhloo, and B. B. Lieber. Treatment of rabbit elastase-induced aneurysm models by flow diverters: Development of quantifiable indexes of device performance using digital subtraction angiography. *IEEE Transaction of Medical Imaging*, 28(7):1117–1125, 2009.

[173] D. F. Kallmes, Y. H. Ding, D. Dai, R. Kadirvel, D. A. Lewis, and H. J. Cloft. A new endoluminal, flow-disrupting device for treatment of saccular aneurysms. *Stroke*, 38(8):2346–2352, 2007.

[174] D. F. Kallmes, Y. H. Ding, D. Dai, R. Kadirvel, D. A. Lewis, and H. J. Cloft. A second-generation, endoluminal, flow-disrupting device for treatment of saccular aneurysms. *American Journal of Neuroradiology*, 30(6):1153–1158, 2009.

[175] Z. Kulcsár, U. Ernemann, S. G. Wetzel, A. Bock, S. Goericke, V. Panagiotopoulos, M. Forsting, D. A. Rüfenacht, and I. Wanke. High-profile flow diverter (SILK) implantation in the basilar artery: Efficacy in the treatment of aneurysms and the role of the perforators. *Stroke*, 41(8):1690–1696, 2010.

[176] D. Fiorella, H. H. Woo, F. C. Albuquerque, and P. K. Nelson. Definitive reconstruction of circumferential, fusiform intracranial aneurysms with the pipeline embolization device. *Neurosurgery*, 62(5):1115–21, 2008.

[177] D. Fiorella, D. Hsu, H. H. Woo, R. W. Tarr, and P. K. Nelson. Very late thrombosis of a pipeline embolization device construct: Case report. *Neurosurgery*, 67 (3):E313–314, 2010.

[178] P. Lylyk, C. Miranda, R. Ceratto, A. Ferrario, E. Scrivano, H. R. Luna, A. L. Berez, Q. Tran, P. K. Nelson, and D. Fiorella. Curative endovascular reconstruction of cerebral aneurysms with the pipeline embolization device: the Buenos Aires experience. *Neurosurgery*, 64(4):632–642, 2009.